Title
Investigating Properties of Active Galactic Nuclei Through Reverberation Mapping

Author
Pei, Liuyi

Publication Date
2016

Peer reviewed|Thesis/dissertation

UNIVERSITY OF CALIFORNIA,
IRVINE

Investigating Properties of Active Galactic Nuclei Through Reverberation Mapping

DISSERTATION

submitted in partial satisfaction of the requirements
for the degree of

DOCTOR OF PHILOSOPHY

in Physics

by

Liuyi Pei

Dissertation Committee:
Professor Aaron J. Barth, Chair
Professor David P. Kirkby
Associate Professor Michael C. Cooper

2016

DEDICATION

To my wonderful husband, who always sees the strength in me.
To my loving grandparents, who always have faith in me.

TABLE OF CONTENTS

Page

LIST OF FIGURES **v**

LIST OF TABLES **vi**

ACKNOWLEDGMENTS **vii**

CURRICULUM VITAE **viii**

ABSTRACT OF THE DISSERTATION **xi**

1 Introduction **1**

2 Reverberation Mapping of the *Kepler*-Field AGN KA1858+4850 **8**
- 2.1 Background . . . 8
- 2.2 Imaging Observations . . . 10
  - 2.2.1 West Mountain Observatory . . . 11
  - 2.2.2 KAIT . . . 11
  - 2.2.3 Faulkes Telescope North . . . 12
  - 2.2.4 The Nickel Telescope . . . 12
  - 2.2.5 Mount Laguna Observatory . . . 12
- 2.3 Photometric Reductions and Measurements . . . 13
  - 2.3.1 V-Band Data . . . 13
  - 2.3.2 *Kepler* Data . . . 17
  - 2.3.3 Continuum Light Curve Characteristics . . . 19
- 2.4 Spectroscopic Observations . . . 21
- 2.5 Spectroscopic Reductions and Measurements . . . 23
- 2.6 Lag Measurements . . . 30
  - 2.6.1 Cross-Correlation Measurements . . . 30
  - 2.6.2 `JAVELIN` . . . 35
  - 2.6.3 Hβ Contamination in the V band . . . 38
  - 2.6.4 Lags with Respect to the *Kepler* Light Curve . . . 39
- 2.7 Line Widths and Black Hole Mass Estimate . . . 40
- 2.8 Eddington Ratio . . . 44

3 Optical Spectroscopic Analysis of the Broad Line Region in NGC 5548 46
3.1 Background . . . 46
3.2 Observations and Data Reduction . . . 49
3.2.1 Spectral Flux Calibrations . . . 52
3.3 Spectroscopic Flux Measurements . . . 56
3.3.1 Spectral Decomposition . . . 60
3.3.2 Host-Galaxy Flux Removal . . . 64
3.3.3 Anomalous Emission-Line Light Curve Behavior . . . 68
3.4 Data Analysis . . . 70
3.4.1 Emission-Line Lag Analysis . . . 70
3.4.2 Anomalous Emission-Line Response to Continuum . . . 82
3.4.3 Line Width and $M_{\rm BH}$ Estimate . . . 91
3.5 Discussion . . . 95
3.5.1 Implications of UV and Optical Hβ Lags . . . 95
3.5.2 Anomalous Emission-Line Light Curve Behavior . . . 98
3.5.3 Comparison to Previous Campaigns: The $R_{\rm BLR} - L_{\rm AGN}$ Relation . . . 99

4 Conclusions 102
4.1 Reverberation Mapping of KA1858+4850 . . . 102
4.2 The Broad Line Region in NGC 5548 . . . 104

Bibliography 106

A Aperture Photometry Pipeline 113
A.1 Background . . . 113
A.2 `Autophot` . . . 115
A.3 Applications and Sample Light Curves . . . 117

B Light Curve Tables from Reverberation Mapping Data 121

LIST OF FIGURES

Page

2.1 KA1858 Field 14
2.2 V-band light curve 16
2.3 *Kepler* light curves 20
2.4 Mean Kast spectrum 23
2.5 Spectral decomposition 24
2.6 Continuum and emission-line light curves 29
2.7 Mean and rms spectra 31
2.8 Emission-line lag analysis 33
2.9 `JAVELIN` light curves 37

3.1 NGC 5548 optical spectrum 49
3.2 Mean and rms spectra 55
3.3 Optical continuum and Hβ light curves 58
3.4 Spectral decomposition 61
3.5 Mean and rms spectra for T1 and T2 65
3.6 Multi-wavelength light curves 66
3.7 UV continuum and Hβ light curves—T1 and T2 69
3.8 Lag distributions from using UV continuum 73
3.9 Lag distributions from using optical continuum 73
3.10 Lag distributions from using V-band continuum 74
3.11 `JAVELIN` light curves 75
3.12 `JAVELIN` lag distributions 76
3.13 Velocity-resolved lags 78
3.14 Hβ velocity-resolved light curves 83
3.15 Hβ light-curve anomaly analysis 86
3.16 Anomalous behaviors for Hβ and He II light curves 90
3.17 Hβ line profile 92
3.18 NGC 5548 $R_{\mathrm{BLR}} - L_{\mathrm{AGN}}$ relation 101

LIST OF TABLES

Page

2.1 Photometric Comparison Stars for KA1858+4850 16
2.2 Photometry measurements for KA1858+4850 17
2.3 Wavelength Windows for Flux Measurements 26
2.4 Spectroscopic Measurements for KA1858+4850 27
2.5 Light-Curve Statistics 30
2.6 Observed-Frame Lag Measurements 34
2.7 Line Widths, Lags, and Derived Black Hole Masses 43

3.1 Instrument characteristics and data reduction parameters for all telescopes . 50
3.2 Flux measurements for continuum and emission lines. 59
3.3 Light Curve Statistics 67
3.4 Observed-Frame Emission-Line Lags 71
3.5 Hβ Velocity-resolved lags 80
3.6 Broad-Line Responsivity 87
3.7 NGC 5548 Hβ Responsivity and AGN Continuum Flux 89
3.8 Hβ Line Widths 94
3.9 Hβ Line Measurements, $M_{\rm BH}$ Estimates, and Continuum Fluxes 95

B.1 Photometry measurements for KA1858+4850 121
B.2 Spectroscopic Measurements for KA1858+4850 138
B.3 NGC 5548 continuum and emission-line flux measurements 144

ACKNOWLEDGMENTS

My thesis work was supported by NSF grants AST-1108835 and AST-1412693. I want to thank the UCI Graduate Division for supporting my final year through the President's Dissertation Year Fellowship, as well as the Associated Graduate Students (AGS) at UCI for funding several of my research trips through AGS Travel Grants.

Support for HST program number GO-13330 was provided by NASA through a grant from the Space Telescope Science Institute, which is operated by the Association of Universities for Research in Astronomy, Inc., under NASA contract NAS5-26555. This thesis makes use of observations from the LCOGT network. Some of the data presented in this thesis were obtained from the Mikulski Archive for Space Telescopes (MAST). STScI is operated by the Association of Universities for Research in Astronomy, Inc., under NASA contract NAS5-26555. Support for MAST for non-*HST* data is provided by the NASA Office of Space Science via grant NNX13AC07G and by other grants and contracts. This thesis includes data collected by the *Kepler* mission, the funding for which is provided by the NASA Science Mission directorate. This research has made use of the NASA/IPAC Extragalactic Database (NED), which is operated by the Jet Propulsion Laboratory, California Institute of Technology, under contract with the National Aeronautics and Space Administration.

Some of the text of this dissertation is a reprint of the material as it appears in the Astrophysical Journal. Permission to use copyrighted material has been granted by the Astrophysical Journal.

I would like to express my sincerest gratitude to my thesis advisor Aaron J. Barth, for his guidance and support in both my scientific and professional development, and for being patient with me all these years. I am also grateful to the past and present members of my research group for their helpful discussions, especially Dan Carson, Ben Boizelle, Carol Hood, and Vivian U, and also Shea Garrison-Kimmel for all his technical help during my first few years of research.

I am grateful to my wonderful husband Jaeyoon Chung for believing in me, to my parents Bin Pei and Susan Liu for their continuous support, and to my dear friends Tiffany Kwong, Andrew Pace, Alan Deng, Andrew Yeager, Noah Tanabe and Peiharn Chen for helping to keep me sane throughout grad school.

My involvement with AGS has helped me tremendously in developing confidence and leadership skills, so I'd like to thank all those I've had the privilege of working with through AGS, especially my fellow members of the AGS executive committees (2014 − 2016), and Timothy Ma for encouraging me to join in the first place.

CURRICULUM VITAE

Liuyi Pei

EDUCATION

Doctor of Philosophy in Physics & Astronomy **2016**
University of California, Irvine *Irvine, CA*

Master of Science in Physics & Astronomy **2012**
University of California, Irvine *Irvine, CA*

Bachelor of Science in Astrophysics **2010**
California Institute of Technology *Pasadena, CA*

RESEARCH EXPERIENCE

Graduate Research Assistant **2011–2016**
University of California, Irvine *Irvine, CA*

Undergraduate Research Assistant **2007–2010**
California Institute of Technology *Pasadena, CA*

LEADERSHIP & OUTREACH

Associated Graduate Student **2014–2016**
University of California, Irvine *Irvine, CA*

Astronomy Ambassador **2014–2016**
American Astronomical Society

Physics Graduate Caucus **2013–2016**
University of California, Irvine *Irvine, CA*

Women in Physics & Astronomy **2013–2016**
University of California, Irvine *Irvine, CA*

Outreach Volunteer **2011–2016**
UCI Observatory *Irvine, CA*

TEACHING & MENTORING

Mentor (UCI Women in Physics & Astronomy) **2015–2016**
University of California, Irvine *Irvine, CA*

Graduate Mentor to Cal-Bridge Scholar **2015**
University of California, Irvine *Irvine, CA*

Teaching Assistant **2012–2014**
California State Summer School for Math and Science *Irvine, CA*

Teaching Assistant for UCI Undergraduate Courses **2011–2012**
University of California, Irvine *Irvine, CA*

FIRST-AUTHOR REFEREED JOURNAL PUBLICATIONS

Space Telescope and Optical Reverberation Mapping Project. V. Optical Emission Line Analysis of NGC 5548 **in prep**
to be submited to The Astrophysical Journal

Reverberation Mapping of the KeplerField AGN KA1858+48 **2014**
The Astrophysical Journal

OTHER REFEREED JOURNAL PUBLICATIONS

Space Telescope and Optical Reverberation Mapping Project. IV. Anomalous Behavior of the Broad Ultraviolet Emission Lines in NGC 5548 **2016**
The Astrophysical Journal

Space Telescope and Optical Reverberation Mapping Project. III. Optical Continuum Emission and Broad-Band Time Delays **2016**
The Astrophysical Journal

Robotic Reverberation Mapping of Arp 151 **2015**
The Astrophysical Journal Letters

Space Telescope and Optical Reverberation Mapping Project. II. Swift and HST Reverberation Mapping of the Accretion Disk of NGC 5548 **2015**
The Astrophysical Journal

Space Telescope and Optical Reverberation Mapping Project. I. Ultraviolet Observations of the Seyfert 1 Galaxy NGC 5548 with the Cosmic Origins Spectrograph on Hubble Space Telescope **2015**
The Astrophysical Journal

Spectroscopic Observations of SN 2012fr: A Luminous, Normal Type Ia Supernova with Early High-velocity Features and a Late Velocity Plateau **2013**
The Astrophysical Journal

The Very Young Type Ia Supernova 2012cg: Discovery and EarlyTime FollowUp Observations **2013**
The Astrophysical Journal Letters

LoCuSS: First Results from Stronglensing Analysis of Massive Clusters **2010**
Monthly Notices of the Royal Astronomical Society

Keck spectroscopic survey of strongly lensed galaxies in Abell 1703: further evidence of a relaxed, unimodal cluster **2009**
Astronomy and Astrophysics

ABSTRACT OF THE DISSERTATION

Investigating Properties of Active Galactic Nuclei Through Reverberation Mapping

By

Liuyi Pei

Doctor of Philosophy in Physics

University of California, Irvine, 2016

Professor Aaron J. Barth, Chair

Reverberation mapping is a time-domain technique used to resolve the supermassive black hole's sphere of influence in active galactic nuclei. We carried out a nine-month reverberation mapping campaign to measure the broad-line region size and estimate the mass of the black hole in KA1858+4850, a narrow-line Seyfert 1 galaxy at redshift 0.078 and among the brightest active galaxies monitored by the *Kepler* mission. We obtained spectroscopic data using the Kast Spectrograph at the Lick 3-m telescope and complementary V-band images from five other ground-based telescopes. We measured the Hβ light curve lag with respect to the V-band continuum light curve, and combined this lag with the Hβ root-mean-square line profile width to obtain a virial estimate of $M_{\rm BH} = 8.06^{+1.59}_{-1.72} \times 10^6\ M_\odot$ for the mass of the central black hole and an Eddington ratio of $L/L_{\rm Edd} \approx 0.2$.

I also used reverberation mapping to study in detail the broad line region in NGC 5548, a Seyfert 1 galaxy at redshift 0.017. Optical spectroscopic data targeting NGC 5548 were taken in 2014 as part of a larger multi-wavelength reverberation mapping campaign. The ground-based spectra spanned six months and achieved almost daily cadence with observations from five telescopes. We computed the Hβ and He II λ4686 lags relative to both the optical continuum and the UV continuum measured by the *Hubble Space Telescope*, and found the Hβ–UV lag to be $\sim$50% longer than the Hβ–optical lag. This suggests that the true

broad-line region size is 50% larger than the size that would be inferred from optical data alone. We also measured velocity-resolved lags for Hβ and found a complex velocity-lag structure with shorter lags in the line wings. The responsivity of both the Hβ and He II lines decreased halfway through the campaign, an anomalous phenomenon also observed for the UV emission lines during the same monitoring period. Finally, we showed that, given the optical luminosity of NGC 5548 during our campaign, the measured Hβ lag is a factor of five shorter than the expected value based on the past behavior of NGC 5548.

To efficiently process large amounts of reverberation mapping photometry data, I developed an IDL pipeline that is able to automatically extract the aperture photometry magnitude of the AGN, calibrate the individual exposures for nightly variations using reference stars, and construct the relative optical continuum light curve combining data from multiple telescopes. This pipeline has been used in several collaborations, both to monitor AGN variability in real time and to construct photometry light curves from archival data, and its applications can be extended to time-domain studies of any variable object.

Chapter 1

Introduction

The launch of the *Hubble Space Telescope* (*HST*) 26 years ago has brought about tremendous advances in many fields of astrophysics, one of which is our understanding of supermassive black holes (SMBHs). Thanks to the high angular resolution of *HST*, it is now commonly understood that a SMBH exists at the center of every massive galaxy. The masses of these black holes (BHs) are on the order of $10^6 - 10^{10}$ $M_\odot$, and have been found to correlate with properties of their host galaxies such as bulge luminosity and bulge stellar velocity dispersion (e.g. Ferrarese & Merritt, 2000; Gebhardt et al., 2000; Gültekin et al., 2009). This correlation is surprising given the significant differences in mass and size between typical SMBHs and their host galaxies—the ratio of BH mass to host galaxy mass is on the order of $\sim 0.2\%$, and the BH's gravitational sphere of influence is on parsec scales while the galaxy bulge size is on kiloparsec scales. These correlations thus suggest that SMBHs and their host galaxies must have co-evolved through cosmic time (see Kormendy & Ho 2013 for a review).

To understand the details of this co-evolutionary process, we must

1) build a large inventory of BH mass ($M_{\rm BH}$) measurements for galaxies across all redshifts in order to study these objects as a population, and

2) examine the local environments of SMBHs in order to understand the mechanisms by which they grow and interact with their host galaxies.

In galaxies whose inner-parsec region can be spatially resolved, the BH mass can be resolved by dynamically modeling the motions of stars and gas orbiting within the BH's sphere of influence. However, because this technique requires high spatial resolution, it is limited in application to objects within ~ 100 Mpc of our galaxy. To probe SMBH properties at larger distances, we must turn to active galaxies, which offer the only insight into the inner few parsecs of galaxies at high redshifts.

The distinction between active and quiescent galaxies is that active galaxies host SMBHs that are accreting at a relatively high rate—typically more than 0.1% of the Eddington rate—and emitting strongly across the electromagnetic spectrum. Studies in the past several decades (Netzer, 2015, and references therein) have led to the "unified" model of the internal structure of an active galactic nucleus (AGN). In this model (see Urry & Padovani, 1995, Figure 8), the BH and accretion disk at the center make up the central engine. Outside of that, on the scale of light-days to light-months, is photoionized gas orbiting deep within the BH's potential well. This gas produces Doppler-broadened emission lines with widths of several thousand km s^{-1}, thus this region is called the broad-line region (BLR). The outer edge of the BLR is thought to be set by the dust sublimation radius (e.g. Netzer & Laor, 1993; Nenkova et al., 2008; Goad et al., 2012), outside of which is dust in a torus-like structure that may obscure the line of sight to the central engine and the BLR depending on the AGN's orientation. There is also photoionized gas far outside the BH's sphere of influence that produce narrow emission lines with widths of around 100 km s^{-1}. The region occupied by this gas is called the narrow-line region (NLR). Finally, some AGNs have also been observed to have relativistic jets that typically flow out of the plane of the accretion disk. This model is "unifying" because it can explain the variety of spectral features seen in different AGNs using only changes in viewing angle. If an AGN is viewed close to edge-on, the dusty torus will obscure the view of the BLR and only narrow emission lines will be observed in the spectrum. If an AGN is viewed more face-on, then both the BLR and the central engine are visible and broad emission lines will be observed.

Reverberation mapping (RM) is a technique used to study the SMBH and its immediate environment in broad-lined AGNs by resolving the BH's sphere of influence in the time domain rather than the spatial domain (Blandford & McKee, 1982; Peterson, 1993). The AGN central engine produces continuum emission that exhibits stochastic flux variations, possibly due to inhomogeneous accretion and thermal fluctuations in the disk (Czerny et al., 1999; Collier & Peterson, 2001; Czerny et al., 2003; Kelly et al., 2009; Kozłowski et al., 2010; MacLeod et al., 2010). The continuum emission photoionizes the BLR gas, and the fluxes in the resulting broad emission lines will echo the variations seen in the continuum light curve with a lag, τ, that corresponds to the response-weighted mean light-travel time from the ionizing continuum to the BLR. The line flux, $L(v_r, t)$, at time t and line-of-sight velocity v_r is related to the continuum by

$$L(v_r, t) = \int_0^\infty \Psi(v_r, \tau) C(t - \tau) d\tau, \tag{1.1}$$

where $C(t - \tau)$ is the continuum emission at an earlier time $t - \tau$, and $\Psi(v, \tau)$ is the transfer function that maps the continuum light curve to the time-variable line profile (Blandford & McKee, 1982).

The transfer function—also known as the velocity-delay map—encodes important information about the BLR's geometry and kinematics that can be used to infer the mass of the central black hole (e.g. Gaskell & Sparke, 1986; Clavel et al., 1991; Kaspi et al., 2000; Denney et al., 2006, 2010; Pancoast et al., 2013). Additionally, since the gas in this region is only several light-days to light-months from the SMBH (e.g. Antonucci & Cohen, 1983; Clavel et al., 1991; Peterson et al., 1998, 2004; Bentz et al., 2009b; Grier et al., 2013), it is possible that infalling BLR gas may fuel AGN accretion (e.g. Gaskell, 1988; Peterson, 2006; Gaskell & Goosmann, 2016) and outflowing gas may contribute to AGN disk winds, which could interact with the host galaxy in the form of AGN feedback (e.g. Murray & Chiang, 1997; Kollatschny, 2003; Leighly & Moore, 2004). The geometry and kinematics of the BLR are therefore key components in completing our understanding of the AGN central engine and its relation to the host galaxy.

There has been tremendous effort in the past three decades by many groups to recover velocity-delay maps (e.g. Rosenblatt & Malkan, 1990; Horne et al., 1991; Krolik et al., 1991; Ulrich & Horne, 1996; Bentz et al., 2010a; Pancoast et al., 2011; Li et al., 2013; Grier et al., 2013; Pancoast et al., 2014) and velocity-resolved line lags, which are lags for individual velocity bins across a broad emission-line profile (e.g. Kollatschny, 2003; Bentz et al., 2009b; Denney et al., 2010; Barth et al., 2011a; Du et al., 2016a). In order to obtain $\Psi(v, \tau)$ for an AGN, RM campaigns must have a combination of high cadence, long duration, high photometric precision, and high signal-to-noise ratio (SNR), which is often not achievable by ground-based programs. More typically, RM campaigns only measure the mean emission-line lag τ, which represents the response-weighted mean light-travel time from the ionizing continuum to the BLR. Under the assumption that the broad-line width is the result of virialized motion around the BH, the emission-line lag and gas velocity dispersion inferred from the line width (ΔV) can be used to infer the mass of the BH using

$$M_{\rm BH} = f \frac{c\tau \Delta V^2}{G}. \tag{1.2}$$

Here, $c\tau$ is the BLR radius ($R_{\rm BLR}$), the fraction quantity is called the virial product, and f is a dimensionless normalization factor of order unity that accounts for the unknown physical properties of the BLR incorporated by the transfer function. The value of f is generally unknown for any individual AGN, so it is customary to use a single value $\langle f \rangle$ that represents the average normalization for all AGNs. This value is typically taken to be the scale factor that puts the sample of RM virial products onto the same $M_{\rm BH} - \sigma_\star$ relation as nearby inactive galaxies (e.g. Onken et al., 2004; Woo et al., 2010; Graham et al., 2011; Park et al., 2012a; Grier et al., 2013; Ho & Kim, 2015).

The basic observational components of an RM campaign designed to measure the BH mass in an AGN are 1) a light curve for at least one broad emission line, typically obtained through spectroscopic monitoring of the object, and 2) a light curve for the AGN continuum, which can be obtained from either the same set of spectra producing the emission-line light curve or from V-band photometric monitoring. The time lag is obtained by cross-correlating the continuum and emission-line light curves, and the BLR velocity dispersion is the width of the broad emission line in the spectrum. Equation 1.2 is then used to compute the BH mass.

While conceptually straightforward, RM is practically very challenging due to the high data quality required to produce robust $M_{\rm BH}$ measurements. For one, the campaign length needs to be at least three times as long as the longest lag being probed in the system (Horne et al., 2004) and the sampling cadence must be dense enough to resolve the expected time lag. The spectral resolution of the data must also be high enough to separate the broad emission lines from other spectral components, and the SNR must be high enough to detect flux variation of only a few percent. Finally, the AGN must be highly variable—which is difficult to predict due to the stochastic nature of the variability—and the weather must be good enough during the course of the campaign so as to not introduce large gaps in the time series. Discontinuity and lack of distinct variability features in the light curves can both lead to large lag uncertainties from cross-correlation.

Combinations of the above factors have resulted in the currently modest sample of ∼60

AGNs with reverberation mapped BH masses. Some of the major campaigns that contributed several or more $M_{\rm BH}$ measurements include those presented by Peterson et al. (1998), Kaspi et al. (2000), Bentz et al. (2009b), Denney et al. (2010), Grier et al. (2013), and Pancoast et al. (2014). Bentz & Katz (2015) compiled a comprehensive database for all AGNs with reverberation mapped BH masses. Most of the objects in this sample are in the nearby universe with redshifts of $z < 0.1$. This is primarily due to the high spectral SNR required to measure AGN variability and the fact that brighter AGNs have longer time delays, which require longer monitoring campaigns to detect.

RM can probe the inner-most parsecs of galactic nuclei in galaxies much further away than those that can be studied using dynamically modeling. However, at even higher redshifts, RM also becomes more difficult due to a combination of several factors. Objects are fainter at greater distances, making it difficult to obtain data with high SNR. AGNs that are visible to us at these distances are intrinsically more luminous, and based on trends observed for local AGNs, the variability timescales are longer and variability amplitudes are lower for more luminous AGNs. The continuum signal will also suffer from geometric dilution due to the larger BLR sizes, and the BLR lags are lengthened by cosmic time dilation. Direct RM is often not feasible for these AGNs, however we can use the observed relation between the size of the Hβ broad-line region and the AGN optical luminosity—or the $R_{\rm BLR} - L_{\rm AGN}$ relation—derived from local reverberation mapped targets to indirectly estimate $M_{\rm BH}$ for higher redshift objects (e.g. Laor, 1998; Wandel et al., 1999; Kaspi et al., 2000, 2005; Bentz et al., 2006, 2009a). From a single spectrum containing a broad emission line (typically Hβ), one can measure both the BLR velocity dispersion and the AGN optical luminosity, the latter can then be used to infer the BLR radius, thereby providing all the required quantities to computed the black hole mass via Equation 1.2. This "single-epoch" method using the $R_{\rm BLR} - L_{\rm AGN}$ relation has been used to estimate BH masses for quasars with $z > 6.5$ (De Rosa et al., 2014), and is to date the only means by which SMBHs in distant quasars can be studied.

Despite significant progress in the field of RM over the last several decades, there is still much to be learned about the immediate environments of SMBHs in AGNs and BH mass scaling relations. For example, the sample of $\sim$ 60 AGNs with BH masses is still not large enough to definitively determine the scale factor $\langle f \rangle$, which can have different values depending on which objects are included in fitting the virial products to the inactive galaxies $M_{\rm BH} - \sigma_\star$ relation, and could also depend on the morphology of the AGN host galaxy (e.g. Onken et al., 2004; Graham et al., 2011; Park et al., 2012a; Grier et al., 2013; Woo et al., 2015). These discrepancies may be reconciled with a much larger sample of AGNs with RM masses. Furthermore, the $R_{\rm BLR} - L_{\rm AGN}$ relation is not well undestood outside of the limited luminosity and redshift ranges covered by the current RM sample. In the era of large-scale spectroscopic surveys, the single-epoch method of estimating BH masses is becoming increasingly important in efficiently probing larger populations of AGNs at higher redshifts. It is thus crucial that we understand the behavior of the $R_{\rm BLR} - L_{\rm AGN}$ relation as it extends to higher luminosities and redshifts.

In my thesis work, I 1) expanded the number of AGNs with reverberation mapped masses by carrying out an RM campaign of a *Kepler*-field AGN, 2) improved our understanding of the BLR-continuum relationship and explored potential sources of systematic effects in the $R_{\rm BLR} - L_{\rm AGN}$ relation through a detailed study of the BLR in the galaxy NGC 5548, and 3) developed an IDL pipeline that quickly and automatically produces AGN photometric light curves, thereby increasing the efficiency of future RM campaigns.

This rest of this document is organized as follows. Chapter 2 describes the RM campaign targeting the *Kepler*-field AGN KA1858+4850, Chapter 3 describes my work in studying the the BLR in NGC 5548, and a summary of the main results of my thesis work is presented in Chapter 4. Appendix A describes my IDL photometry pipeline and its applications, and Appendix B contains light curve tables from both the KA1858+4850 and NGC 5548 RM campaigns.

Chapter 2

Reverberation Mapping of the *Kepler*-Field AGN KA1858+4850

2.1 Background

The NASA *Kepler* Mission, designed to search for exo-planets, continuously monitored the brightness of more than $100,000$ stars in a 115 square-degree field for about four years (Borucki et al., 2010). Situated within the *Kepler* field are several active galactic nuclei (AGNs) that also exhibit optical flux variations. *Kepler*'s monitoring capabilities enable measurements of AGN optical light curves over long temporal baselines with unprecedented cadence and precision, providing the basis for extremely detailed AGN variability studies.

Observations have revealed correlations between AGN variability amplitude and redshift (Cristiani et al., 1990; Giallongo et al., 1991; Hook et al., 1994; Cid Fernandes et al., 1996; Vanden Berk et al., 2004), variability amplitude and black hole mass (Wold et al., 2007; Wilhite et al., 2008; Bauer et al., 2009), and anticorrelations between variability amplitude and luminosity (Cristiani et al., 1990; Hook et al., 1994; Cid Fernandes et al., 1996; Giveon et al., 1999; Vanden Berk et al., 2004; Webb & Malkan, 2000). Furthermore, analyses of continuum light curves have revealed the presence of characteristic variability timescales which have been found to vary with black hole mass (Collier & Peterson, 2001; MacLeod et al., 2010). The *Kepler* high-resolution light curves have a cadence of 30 minutes, and are the only datasets to date that have been able to probe optical AGN variability down to such short timescales. Optical fluctuation power spectral density functions for several *Kepler* AGNs have already been published (Mushotzky et al., 2011), and they have shown much steeper slopes than those seen in the X-rays. *Kepler*'s light curves provide new high signal-to-noise ratio (SNR) data which will test and better constrain these previously established correlations and further shed light on AGN variability characteristics.

Independent measurements of black hole mass are required to search for connections between AGN variability characteristics and black hole mass. To this end, we present the results of a nine-month monitoring campaign for the narrow-line Seyfert 1 (NLS1) galaxy 1RXSJ185800.9+485020, also known as KA1858+4850, which has redshift $z = 0.078$ and a Galactic extinction of $A_V = 0.15$ mag (Schlafly & Finkbeiner, 2011). This object was identified as an X-ray source in the *ROSAT* All-Sky Bright Source Catalogue (Voges et al., 1999). Prior to 2012, there was no published spectrum of KA1858+4850 in the literature, and an observation from Lick Observatory identified it as a Seyfert 1 galaxy (Edelson & Malkan, 2012). The initial portion of KA1858+4850's *Kepler* light curve from quarters Q6 and Q7 was published by Mushotzky et al. (2011) and showed strong optical variability, qualifying it as a prime candidate for reverberation mapping.

The technique of reverberation mapping relies on the assumption that variability in the AGN continuum is echoed by emission lines originating from the surrounding broad-line region (BLR; **?**). Ionizing photons from the AGN central engine travel to the BLR gas in a time τ that is a function of the BLR radius. Changes in the ionizing photon flux incident on BLR clouds cause fluctuations in the emission-line flux. This means that the emission-line light curve will appear as a lagged version of the continuum light curve, and the lag time, combined with the speed of light, can give an estimate of the BLR radius. Additionally, the line-emitting gas orbits the central black hole at very high velocities, which causes Doppler broadening of the emitted spectral lines. The width of the broad emission line gives the velocity dispersion of the BLR gas, which, combined with the BLR radius, can yield a virial estimate of the central black hole mass.

Kepler light curves covering over two years of monitoring are now publicly available for KA1858+4850, of which three consecutive quarters (Q13, Q14, and Q15) directly coincide with the time of our ground-based monitoring campaign. We therefore performed our analysis using both V-band and *Kepler* observations.

We employed the Lick Observatory 3-m Shane telescope with the Kast Spectrograph and five other ground-based telescopes to spectroscopically and photometrically monitor KA1858+4850 from February to November of 2012. We describe our imaging observations and data reductions in Sections 2.2 and 2.3; spectroscopic observations, reductions, and measurements are described in Sections 2.4 and 2.5; Section 2.6 outlines the steps in measuring emission-line light curve lags; our estimates of the black hole mass ($M_{\rm BH}$) and Eddington ratio are discussed in Sections 2.7 and 2.8; and Section 2.9 summarizes our results for this project.

2.2 Imaging Observations

Reverberation mapping requires a continuum light curve with high sampling cadence and SNR. To achieve this, we obtained V-band images from ground-based telescopes and used aperture photometry to construct a light curve for KA1858+4850 that has nearly nightly sampling for a span of 290 days. For several reasons, we chose to use the V-band light curve rather than the *Kepler* light curve for reverberation measurements. First, we wanted to monitor the AGN's variability in real time, and since *Kepler* data are uploaded only periodically, this was possible only with ground-based monitoring. Additionally, the *Kepler* passband, at 4000−8650 Å, includes the strong Hα emission line, which can contribute significantly to the photometric fluxes and introduce a strong lag signal to what should ideally be a pure continuum light curve. Furthermore, *Kepler* light curves exhibit severe mismatches between the flux scales for different quarterly observation sets, as can be seen in light curves shown by Revalski et al. (2014). We avoided these issues by constructing the continuum light curve with photometric data from five ground-based telescopes, whose properties are described in the following sections.

2.2.1 West Mountain Observatory

The Brigham Young University West Mountain Observatory (WMO) uses a 0.9-m telescope that employs a FLI PL3041UV detector with a $20'.8 \times 20'.8$ field of view. The CCD has 15 μm pixels and a scale of $0''.61$ pixel^{-1}. KA1858+4850 was observed at WMO with exposure times of 200 s, 240 s, 250 s, or 300 s. WMO data covered the period from March to November of 2012 with images from 124 nights, and had a median seeing of $3''.2$. Figure 2.1 shows a portion of the WMO field of view centered on KA1858+4850.

2.2.2 KAIT

The Katzman Automatic Imaging Telescope (KAIT) at Lick Observatory is a 0.76-m robotic telescope with an Apogee AP7 CCD, which has 24 μm pixels in a 500×500 array and a scale of $0''.8$ pixel^{-1} (Filippenko et al., 2001). KA1858+4850 was observed with KAIT using 300 s exposures with the exception of six nights, for which exposure times of 60 s, 180 s, or 240 s were used. The median seeing for the KAIT exposures was $3''.2$, and the observing period at KAIT spanned February to September of 2012 with data from 109 nights.

2.2.3 Faulkes Telescope North

The Faulkes Telescope North (FTN), operated by the Las Cumbres Observatory Global Telescope Network, is a 2-m telescope located at the Haleakala Observatory in Hawaii. We used the Spectral camera with a Fairchild Imaging CCD486 detector, which has a $10'.5 \times 10'.5$ field of view (Brown et al., 2013). The CCD has 15 μm pixels in a 4000×4000 array and has a scale of $0''.152$ pixel^{-1}. The images were obtained using 2×2 binning for the readout. KA1858+4850 was observed at FTN with 120 s exposures from February to March 2012. The exposure time was increased to 180 s in April 2012, then to 240 s in May for the remainder of the program ending in November. We obtained 65 epochs of data from FTN, with median seeing of $1''.6$.

2.2.4 The Nickel Telescope

The 1-m Nickel telescope at Lick Observatory employs a Loral 2048×2048 CCD with a $6'.3 \times 6'.3$ field of view and a scale of $0''.184$ pixel^{-1}. The images were obtained using 2×2 binning for the readout. KA1858+4850 was observed on the Nickel adopting 300 s exposures with the exception of three nights, for which 150 s, 250 s, and 600 s exposures were used. We obtained 47 epochs of data from the Nickel between February and November of 2012, and the median seeing was $2''.4$.

2.2.5 Mount Laguna Observatory

The Mount Laguna Observatory (MLO) 1-m telescope uses a Fairchild CCD that has 15 μm pixels in a 2048×2048 array, and has a scale of $0''.41$ pixel^{-1}. KA1858+4850 was observed at MLO with 300 s exposures. The median seeing for the MLO exposures was $3''.0$. Between February and November of 2012, we obtained 27 epochs of data from MLO.

2.3 Photometric Reductions and Measurements

2.3.1 *V*-Band Data

Photometric data reduction included overscan correction, trimming, bias subtraction, and flat fielding for all images. We used the *Astrometry.net* software (Lang et al., 2010) to register celestial coordinates onto images from WMO, KAIT, Nickel, and MLO. This step was omitted for FTN data, which already contained celestial coordinates in the image headers. After cleaning all images of cosmic rays using the L.A.Cosmic algorithm (van Dokkum, 2001a), we performed aperture photometry in IDL using an aperture radius of $3''$ and sky annulus radii of $10''-20''$, and obtained instrumental magnitudes for KA1858+4850 and seven comparison stars (marked in Figure 2.1) for each image. The comparison stars were chosen to have similar or slightly brighter V-band magnitudes compared to KA1858+4850. For nights where multiple exposures were taken at the same telescope, the magnitude measurements for each object were averaged into a single value. Since KA1858+4850 is almost indistinguishable from a point source at ground-based resolution, we did not attempt to remove host-galaxy light from the AGN photometry.

We used the comparison stars as constant-flux references and obtained a separate AGN light curve for each telescope. However, the uncertainties from aperture photometry photon counting errors underestimate the true photometric error budget. Additional sources of error include inconsistencies in flat-field corrections and poor comparison-star magnitude measurements owing to blemishes on the detector. We measured the magnitude of these additional errors by calculating the excess variance, defined as

$$\sigma_{\mathrm{x}}^2 = \frac{1}{N}\sum_{i=1}^{N}[(X_i-\mu)^2-\sigma_i^2], \tag{2.1}$$

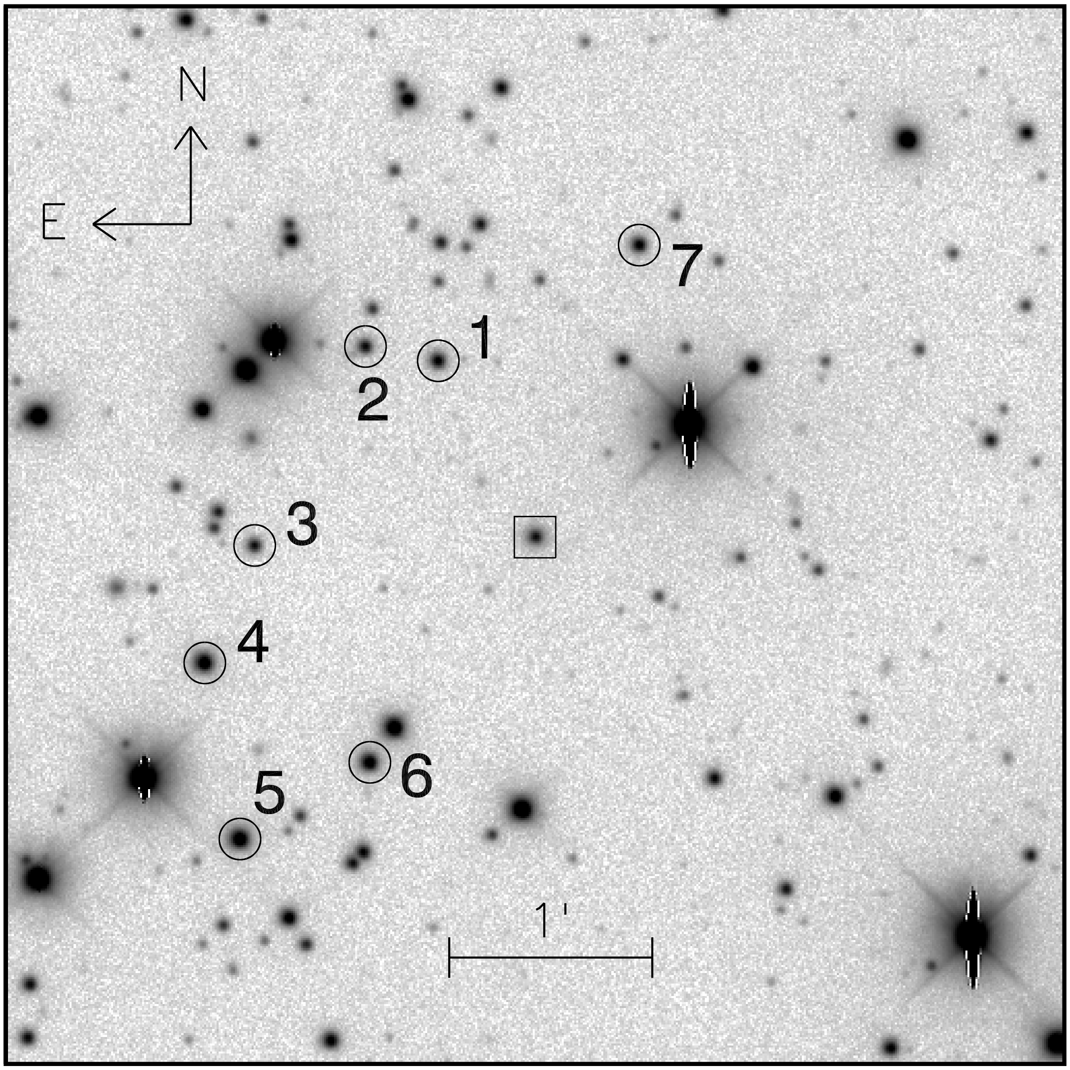

Figure 2.1: A subset of a coadded frame created from WMO images showing KA1858+4850 (boxed) and its seven comparison stars (circled).

in the scaled comparison-star light curves. Here, N is the number of measurements in the sample, μ is the mean magnitude, and X_i and σ_i are the individual measurements and their associated uncertainties, respectively. The σ_i values range from 0.004 mag to 0.048 mag, and the median and standard deviation of the uncertainties are 0.009 mag and 0.007 mag, respectively. We found the mean scatter of all seven comparison stars to be $\sigma_{\mathrm{x}} \approx 0.001$ mag, and added this in quadrature to the uncertainties from aperture photometry to produce the final AGN light curve for each telescope.

To combine the light curves from different telescopes, we scaled each light curve so that the mean comparison-star magnitudes for each telescope matched those from WMO, the telescope with the highest SNR and cadence and longest temporal coverage. However, each telescope has a different wavelength-dependent throughput, which can cause systematic offsets between light curves from different telescopes since the AGN is likely bluer than the average comparison-star color. We tested for these offsets by calculating the differences between AGN magnitude measurements taken on the same night but at different sites, and found the offsets to be on the order of 0.01 mag. We applied these calculated shifts to the FTN, KAIT, MLO, and Nickel light curves and brought them into agreement with WMO to produce the combined light curve.

Finally, we used Landolt (1992) standard stars observed at WMO to calibrate the zero point of the magnitude scale and produce the final light curve. We used WMO images from 18 nights, on which the observers deemed conditions photometric, to calibrate the comparison-star magnitudes. We did not attempt to compute color dependence in the Landolt calibrations.

Because truly photometric conditions are rare and difficult to confirm, each night gave slightly different comparison-star magnitudes. We took the weighted mean magnitude and standard deviation over 18 nights to be the magnitude and uncertainty for each star. The V magnitudes of the comparison stars are listed in Table 2.1.

Table 2.1. Photometric Comparison Stars for KA1858+4850

Star	α (h:m:s)	δ ($\circ$:$\prime$:$\prime\prime$)	V (mag)
1	18:58:04.03	48:51:15.53	16.612 ± 0.026
2	18:58:06.24	48:51:19.82	17.121 ± 0.037
3	18:58:09.54	48:50:20.69	17.256 ± 0.031
4	18:58:11.03	48:49:46.16	15.449 ± 0.028
5	18:58:09.97	48:48:54.06	15.195 ± 0.029
6	18:58:06.09	48:49:16.65	15.843 ± 0.029
7	18:57:58.01	48:51:49.72	16.724 ± 0.027

Note. — Coordinates are J2000 and are based on an astrometric solution obtained by the *astrometry.net* software (Lang et al., 2010). The quoted uncertainties are calculated as the standard deviation of 18 measurements from photometric nights at WMO.

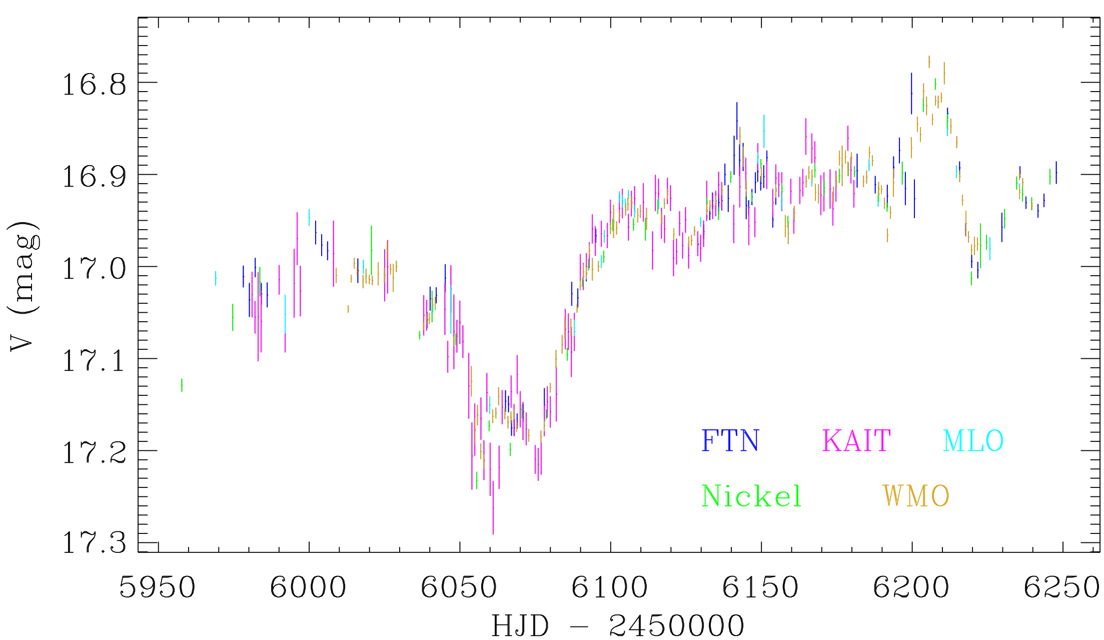

Figure 2.2: KA1858+4850 V-band light curve.

Table 2.2. Photometry measurements for KA1858+4850

UT Date	Telescope	HJD − 2450000	V (mag)
2012-01-31	N	5957.754	17.129 ± 0.008
2012-02-11	M	5969.014	17.012 ± 0.015
2012-02-17	N	5974.663	17.055 ± 0.015
2012-02-20	F	5978.153	17.011 ± 0.014
2012-02-22	F	5980.166	17.037 ± 0.020

Note. — The telescopes are listed as follows: N = Nickel, M = MLO, F = FTN, K = KAIT, W = WMO. (See Appendix B for full table.)

Figure 2.2 plots the final V-band light curve for KA1858+4850. The vertical length at each epoch indicates the photometric uncertainties, and the data are listed in Table B.1. We averaged photometric measurements taken within 12 hours of each other to produce a condensed light curve that was used for subsequent lag analyses.

The steps from performing aperture photometry to obtaining a multiple-telescope light curve were carried out using an automated pipeline (see Appendix A). Mapping WCS coordinates onto the images allowed for automatic detection of the AGN and comparison-star locations for aperture photometry. The automated nature of this process enables the pipeline to process a large number of images at once, and to rapidly produce and update the AGN light curve as new images are acquired.

2.3.2 *Kepler* Data

We also obtained *Kepler* Simple Aperture Photometry (SAP) fluxes for KA1858+4850 from the MAST archive for Q13, Q14, and Q15, corresponding to 2012 March through November. Data from Q12 are missing from the archive because, during this time, the source fell on

Module 3 of the *Kepler* telescope, which failed early on in the mission.

The *Kepler* light curves are mismatched between individual quarters, so we used our V-band light curve as a reference to scale each quarter's light curve individually. We applied a different multiplicative scale factor and additive shift to each quarterly *Kepler* light curve to bring it into agreement with ground-based observations. The multiplicative factors account for the difference in transmission between the *Kepler* and V-band filters, and the additive constants account for the changes in AGN-to-host galaxy flux ratio between each quarter caused by using different quarterly extraction apertures to obtain SAP fluxes.

For each epoch in the condensed V-band light curve, we averaged together all *Kepler* flux measurements taken within six hours of the V-band measurement to compose condensed *Kepler* light curves. Then for each quarter, we fitted the contemporaneous *Kepler* and V-band flux measurements to the equation

$$f_V = m * f_{\mathrm{Kepler}} + b, \tag{2.2}$$

where m gives the multiplicative scale factor and b gives the additive shift. We fitted the data using MPFITEXY to account for measurement errors in both V-band and *Kepler* data. Figure 2.3 shows the results of applying a scale factor (top panel) and a scale factor plus a shift (middle panel) to the *Kepler* light curves.

Even with a multiplicative scale factor and an additive shift, however, there are still visible discrepancies between the two sets of data. Specifically, each *Kepler* quarterly light curve tilts downward with time compared to the V-band light curve. This is caused by the constant change in *Kepler* pointing with respect to the *Kepler* field as the telescope orbited the Sun, which, in turn, causes differential velocity aberration (DVA) and results in a trend that is superimposed on the light curve within the period of each quarter (Still & Barclay, 2012). To account for this effect, we applied an empirical secular linear trend to the V-band light curve by adding a time-dependent flux to the data. The *Kepler* light curves were then fitted to the adjusted V-band light curve with scale factors and shift constants. Finally, the empirical trend was removed from both V-band and *Kepler* light curves by subtracting the same time-dependent fluxes as before. The resulting scaled *Kepler* light curves are shown in the bottom panel of Figure 2.3, and were used for subsequent *Kepler*-related lag analyses.

We note that the *Kepler* passband is much better matched to the R band rather than the V band, which means there could be color-dependent variability signals contributing to discrepancies between the V and *Kepler* light curves. We also note that the SAP light curves from the *Kepler* archive are susceptible to several instrumental effects. First, the use of different sized apertures between individual quarters affects the SAP fluxes more so than the *Kepler* Pre-search Data Conditioning Simple Aperture Photometry (PDCSAP) fluxes because of the much smaller aperture sizes of SAP. Additionally, the effects of DVA are also larger in the SAP light curves compared to the PDCSAP light curves. A more robust analysis of *Kepler* AGN data would require re-extracting the SAP light curve over a larger set of pixels to remove these systematics, but that is beyond the scope of this work.

2.3.3 Continuum Light Curve Characteristics

To quantify the observed KA1858+4850 continuum variability during our monitoring period, we computed the statistics $R_{\rm max}$ and $F_{\rm var}$ for consistency with previous reverberation mapping studies (Rodriguez-Pascual et al., 1997; Peterson et al., 2004). $R_{\rm max}$ is defined as

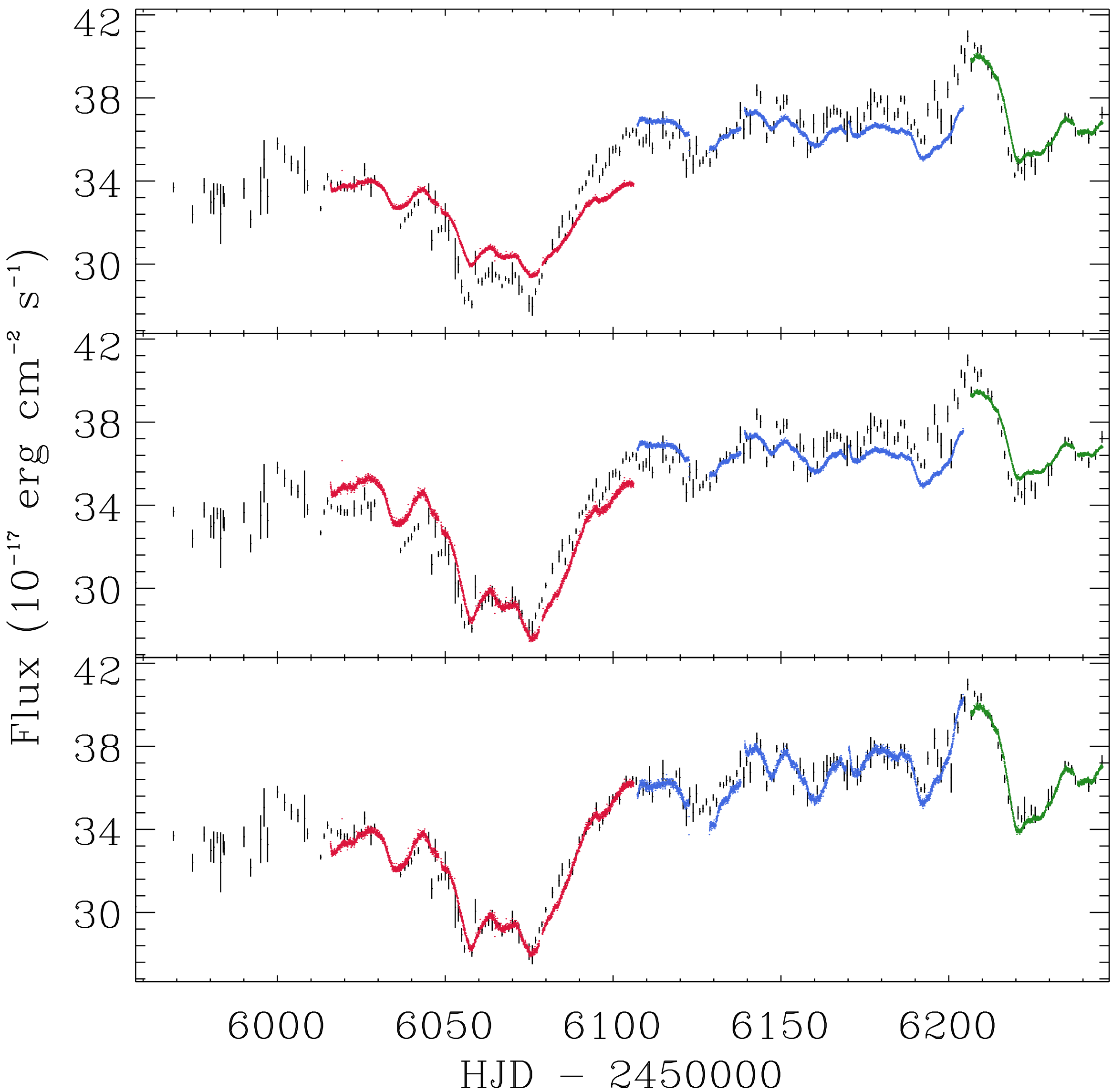

Figure 2.3: V-band light curve (black) overplotted with *Kepler* Q13, Q14, and Q15 light curves in red, blue, and green (respectively), scaled by three different methods. *Top:* multiplicative factor only; *middle:* multiplicative factor plus additive constant; *bottom:* multiplicative factor plus additive constant fitted to a V-band light curve with an additional linear trend. Error bars are not plotted for the *Kepler* points.

the ratio between the maximum and minimum observed fluxes, and $F_{\rm var}$ is defined as

$$F_{\rm var} = \frac{\sqrt{\sigma^2 - \langle\delta^2\rangle}}{\langle f\rangle}, \tag{2.3}$$

where σ^2 is the sample variance, $\langle\delta^2\rangle$ is the mean square value of the measurement uncertainties, and $\langle f\rangle$ is the unweighted mean flux. $F_{\rm var}$ is essentially an estimate of the intrinsic root-mean-square (rms) variability relative to the mean flux corrected for random errors. We found $R_{\rm max} = 1.56$ and $F_{\rm var} = 0.086$ for the V-band light curve and $R_{\rm max} = 1.45$ and $F_{\rm var} = 0.080$ for the *Kepler* light curve.

A previous AGN monitoring campaign carried out by the LAMP 2008 collaboration observed 13 AGNs over a two-month period (Bentz et al., 2009a). Five of these AGNs (Mrk 142, Mrk 1310, Mrk 202, NGC 4253, and NGC 4748) are NLS1 galaxies with full width at half-maximum intensity FWHM(H$\beta_{\rm broad}$) < 2000 km s^{-1}. The $F_{\rm var}$ values for their V-band light curves range from 0.27 to 0.73, and the $R_{\rm max}$ values range from 1.12 to 1.39. Compared to these NLS1s, KA1858+4850 was significantly more variable during our monitoring period, with both $F_{\rm var}$ and $R_{\rm max}$ values much larger than those for the LAMP 2008 NLS1 galaxies over their two-month monitoring period.

2.4 Spectroscopic Observations

Spectroscopic observations of KA1858+4850 were carried out using the Kast Spectrograph on the Shane 3-m telescope at Lick Observatory. This spectrograph is usually mounted only during dark runs. We employed an interrupt-mode observing method, where every group of Kast observers took one exposure of KA1858+4850 on each of their regularly scheduled observing nights. This enabled us to spectroscopically monitor the AGN for a total of nine months, much longer than what is achievable by most dedicated observing campaigns at classically scheduled facilities.

The Kast spectrograph has a D55 dichroic that splits light from the slit at about 5500 Å into separate blue- and red-side cameras. Our standard setup used a 600/4310 grism on the blue side, which gives a wavelength dispersion of 1.02 Å pixel^{-1} and wavelength range of 2090 Å. However, the wavelength coverage was inconsistent because each group used a slightly different blue-side setup that shifted the wavelength coverage, and on the nights of 2012 February 16, 2012 March 4, 2012 April 19, and 2012 May 1, the observers employed a 830/3460 grism. We used the wavelength range 4000−5500 Å for our analysis as this is common to all spectra. This wavelength range includes the Hβ, Hγ, Hδ, [O III], and He II emission lines, as well as a portion of the Balmer continuum.

On the red side, because different observing teams used significantly different setups for their primary science targets, we were unable to obtain a complete set of spectra with consistent quality and wavelength coverage for analysis of the Hα line. For reference, Figure 2.4 shows the unweighted mean AGN spectrum constructed from all nights with both blue- and red-side Kast data.

From February to November of 2012, weather permitting, each regularly scheduled group of Kast observers took at least one 1200 s exposure of KA1858+4850 at the parallactic angle (Filippenko, 1982) using a 2″ slit, along with one 120 s exposure of a flux-standard star with the same slit width for calibration. Two consecutive exposures of KA1858+4850 were taken on two nights and three consecutive exposures were taken on four nights. The flux standards we used are BD+284211, Feige 34, G191B2B, and HZ 44, in decreasing order of frequency. Very few spectra were taken in February and March owing to poor weather conditions. April and May had several good nights of data, and starting from June until the end of the campaign in November, we obtained spectra during more than two-thirds of the

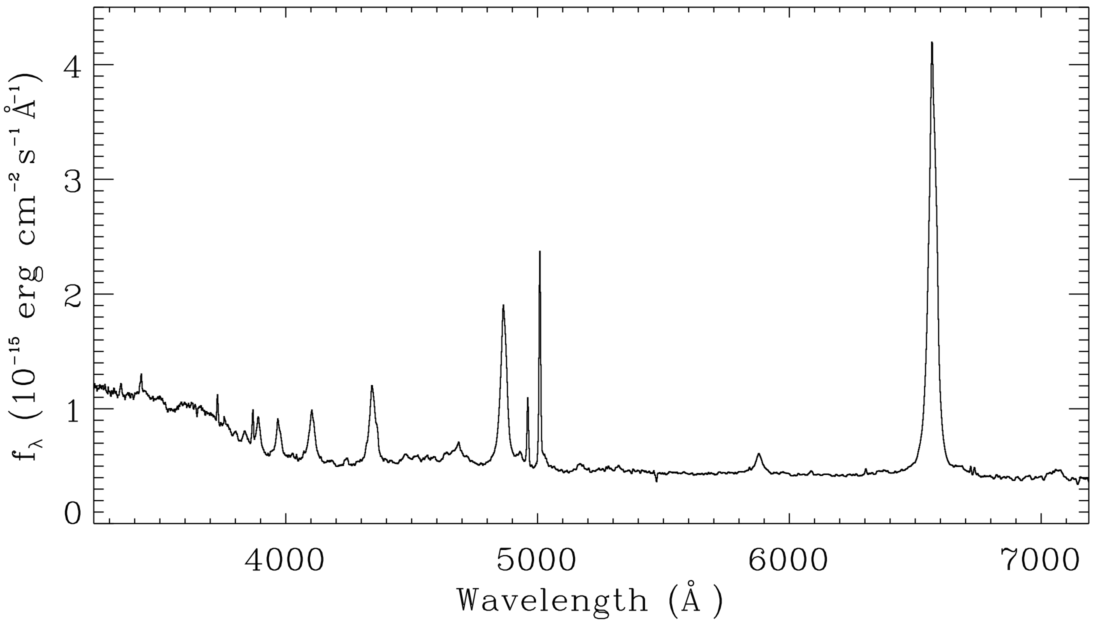

Figure 2.4: Mean rest-frame spectrum of KA1858+4850 constructed from all nights with both blue- and red-side Kast observations.

Kast nights each month. We obtained spectroscopic data from a total of 74 nights.

2.5 Spectroscopic Reductions and Measurements

Spectroscopic data reduction included overscan subtraction, flat fielding, cosmic ray cleaning using the L.A.Cosmic routine (van Dokkum, 2001a), extraction with a width of $6''.88$ (corresponding to a 16-pixel extraction window for the blue-side data), wavelength calibration employing line-lamp exposures, and flux calibration using standard stars. We took unweighted extractions for AGN spectra and optimal extractions for standard-star spectra. Spectra taken on the same night were averaged into a single spectrum. We also propagated the extracted error spectrum through subsequent calibrations and analyses.

We attempted to perform spectral decomposition using methods described by Barth et al. (2013) to isolate the broad-line components. However, owing to the presence of weak and

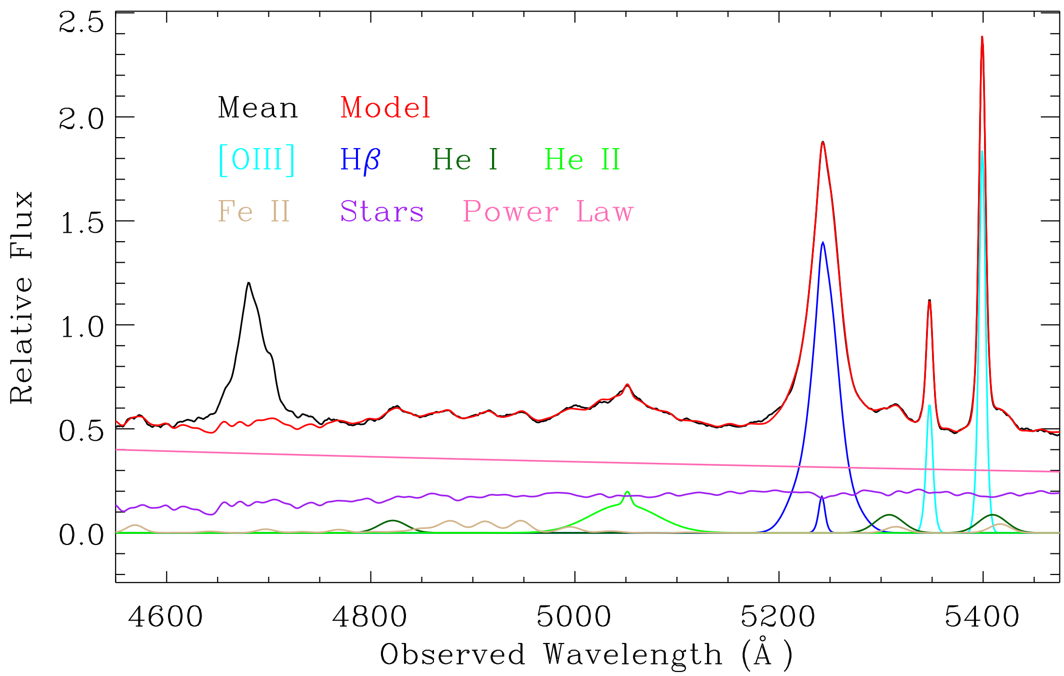

Figure 2.5: KA1858+4850 mean spectrum (black), the combined model fit of all components (red), and individual spectral fit components. The Hγ and [O III] λ4363 blend was excluded from the fits in order to limit the total number of fit parameters.

blended emission lines as well as limited spectral coverage, many single-epoch spectra produced poorly constrained fit parameters for the continuum components, He II and Fe II emission, and reddening. We therefore used the traditional approach of measuring line fluxes by employing a linear fit to approximately subtract the continuum underlying emission lines. The decomposed components of the higher-SNR mean spectrum are displayed in Figure 2.5 for reference.

To quantify the flux-measurement uncertainty introduced by using this linear interpolation approach as opposed to the spectral deomposition method, we also measured $f(\mathrm{H}\beta)$ of a series of Hβ-only spectra. Each Hβ-only spectrum was created by subtracting from the data all model fit components except the broad and narrow Hβ models. We found that $f(\mathrm{H}\beta)$ measured from the Hβ-only spectra are, on average, 1.2% higher than those measured by simply interpolating over the continuum in the data.

To calibrate the relative fluxes between individual spectra, we followed steps described by van Groningen & Wanders (1992a), where the [O III] lines are taken to be constant in flux for the duration of the campaign. As the [O III] line is emitted by gas in the narrow-line region, which is much farther out from the black hole than the BLR, the time delay in line response to continuum variations is much longer than typical reverberation mapping campaigns. The algorithm applies a multiplicative flux scaling factor, a small wavelength shift, and a convolution with a Gaussian kernel to a region in each individual spectrum that contains a narrow emission line and some surrounding continuum, and searches for a combination of these parameters that minimizes the residual between this region in the individual spectrum and the same region in a reference spectrum. We constructed the reference spectrum from the mean of all Kast blue-side spectra taken with the 600/4310 grism, and chose the observed wavelength range 5390−5410 Å, which encompasses the [O III] λ5007 emission line, to be the comparison region. Spectra taken with the 830/3460 grism were not used to make the reference spectrum, but were calibrated using the same method. The flux scale factors range from 0.27 to 4.70. The median wavelength shift is 1.2 Å, which is consistent with the amount expected from miscentering the AGN in the slit.

We followed steps described by Barth et al. (2011b) to assess the accuracy of the spectral scaling, and calculated the normalized excess variance of the [O III] emission-line light curve. The normalized excess variance, $\sigma^2_{\rm nx}$, is defined by normalizing Eq. A.2 by a factor of the mean flux squared, giving

$$\sigma^2_{\rm nx} = \frac{1}{N\mu^2}\sum_{i=1}^{N}[(X_i-\mu)^2-\sigma_i^2]. \tag{2.4}$$

We found $\sigma_{\rm nx} \approx 0.02$ for the [O III] light curve after flux scaling, indicating that, above the uncertainties from photon counting in flux measurements, there is an additional scatter on

Table 2.3. Wavelength Windows for Flux Measurements

Line (Å)	Line Window (Å)	Continuum Windows (Å)
Hβ	5200−5290	5130−5160, 5360−5390
He II	4990−5100	4960−4980, 5120−5160
Hγ	4650−4720	4600−4640, 4730−4780
Hδ	4395−4455	4360−4380, 4470−4500
Hβ-blue	5200−5238	5130−5160, 5360−5390
Hβ-core	5239−5249	5130−5160, 5360−5390
Hβ-red	5250−5290	5130−5160, 5360−5390

Note. — Wavelengths are in the observed frame.

the order of 2% of the total [O III] flux in the scaled light curve. This scatter may be caused by a combination of variations in seeing, miscentering of the AGN in the slit, and nightly variations in the instrument focus. Overall, this is a relatively small effect on the flux scaling of the Hβ light curve. We added this 2% flux scatter in quadrature to all spectroscopic flux uncertainties before performing further analysis.

The spectroscopic data were photometrically calibrated by carrying out synthetic V-band photometry on the spectrum from 2012 September 9, which was taken under nearly photometric conditions. We compared this magnitude to the aperture photometry magnitude from the same night and calculated a scale factor of 1.15 that needed to be applied to the spectrum to bring the synthetic photometry measurement into agreement with the aperture photometry measurement. We then applied this scale factor to the entire set of Kast spectra.

Table 2.4. Spectroscopic Measurements for KA1858+4850

UT Date	HJD−2450000	SNR	$f(\mathrm{H}\beta)$	$f(\mathrm{H}\gamma)$	$f(\mathrm{H}\delta)$	$f(\mathrm{He\ II})$
				(10^{-15} erg s^{-1} cm^{-2})		
2012-02-16	5974.087	11	42.87 ± 0.38	19.12 ± 0.51	8.27 ± 0.54	11.60 ± 0.47
2012-03-04	5991.073	35	40.90 ± 0.14	18.37 ± 0.14	9.84 ± 0.14	7.30 ± 0.14
2012-04-02	6020.024	19	42.42 ± 0.30	19.30 ± 0.27	12.24 ± 0.27	9.68 ± 0.28
2012-04-16	6033.929	21	45.20 ± 0.28	22.75 ± 0.26	13.73 ± 0.26	10.20 ± 0.27
2012-04-16	6034.975	34	46.41 ± 0.19	22.53 ± 0.16	13.15 ± 0.16	8.04 ± 0.16
2012-04-20	6036.930	24	42.77 ± 0.22	21.05 ± 0.23	11.19 ± 0.25	7.72 ± 0.22
2012-04-24	6041.013	22	44.66 ± 0.29	20.27 ± 0.24	10.99 ± 0.24	9.29 ± 0.25
2012-04-28	6046.026	11	45.42 ± 0.36	20.86 ± 0.43	11.14 ± 0.45	10.26 ± 0.39
2012-05-00	6048.942	21	44.91 ± 0.24	22.80 ± 0.27	12.31 ± 0.29	9.62 ± 0.25
2012-05-18	6065.967	30	41.41 ± 0.17	18.68 ± 0.15	10.41 ± 0.15	5.35 ± 0.16
2012-05-20	6066.952	29	41.92 ± 0.20	18.94 ± 0.16	10.63 ± 0.16	5.80 ± 0.16

Note. — Listed SNR is the signal-to-noise ratio per pixel for the observed wavelength range 4500–4600 Å in the AGN spectra. Measured fluxes include the blended broad and narrow emission lines. (See Appendix B for full table.)

To obtain emission-line fluxes, we first subtracted a local linear continuum surrounding the line, then integrated over the emission-line profile. Table 2.3 shows the wavelength ranges used for each line and their local continuum windows. Table B.2 gives the spectroscopic measurements of the Hβ, Hγ, Hδ, and He II emission lines for the entire dataset, as well as the SNR for each epoch measured using the observed wavelength range 4500$-$4600 Å. The median SNR per pixel is 28.

Figure 2.6 displays the V-band photometric and spectroscopic light curves for the Hβ, Hγ, Hδ, and heii emission lines. The scaling routine works best for wavelength ranges closest to the [O III] emission lines, so at wavelengths farther away from [O III], the higher-order Balmer-line light curves become progressively noisier. Noise in the He II light curve is primarily caused by weak line strength as well as a lack of true continuum surrounding the line. The presence of Fe II lines blended into the blue side of He II, and the fact that the He II line is intrinsically very weak and broad, make fitting the true continuum with a linear model very difficult. The spectral decomposition components of He II are also poorly constrained owing to the line's low amplitude.

Figure 2.6 also illustrates the spectroscopic light curve for the observed wavelength range 4500$-$4600 Å. This region is dominated by continuum emission, so its light curve can be compared with the V-band light curve. This spectroscopic B-band continuum light curve, denoted by $B_{\rm s}$, is noisier than that of the V band owing to higher susceptibility to seeing variations and slit losses, but the two light curves show consistent variability trends during the monitoring period.

The $F_{\rm var}$ and $R_{\rm max}$ values for each of the light curves are listed in Table 2.5. The higher-order Balmer lines exhibit distinctly larger relative variability amplitude, and the He II line is proportionally more variable than all the Balmer lines. Both results are in agreement with findings of previous reverberation mapping programs (Peterson & Ferland, 1986; Dietrich et al., 1993; Kollatschny, 2003; Bentz et al., 2010b).

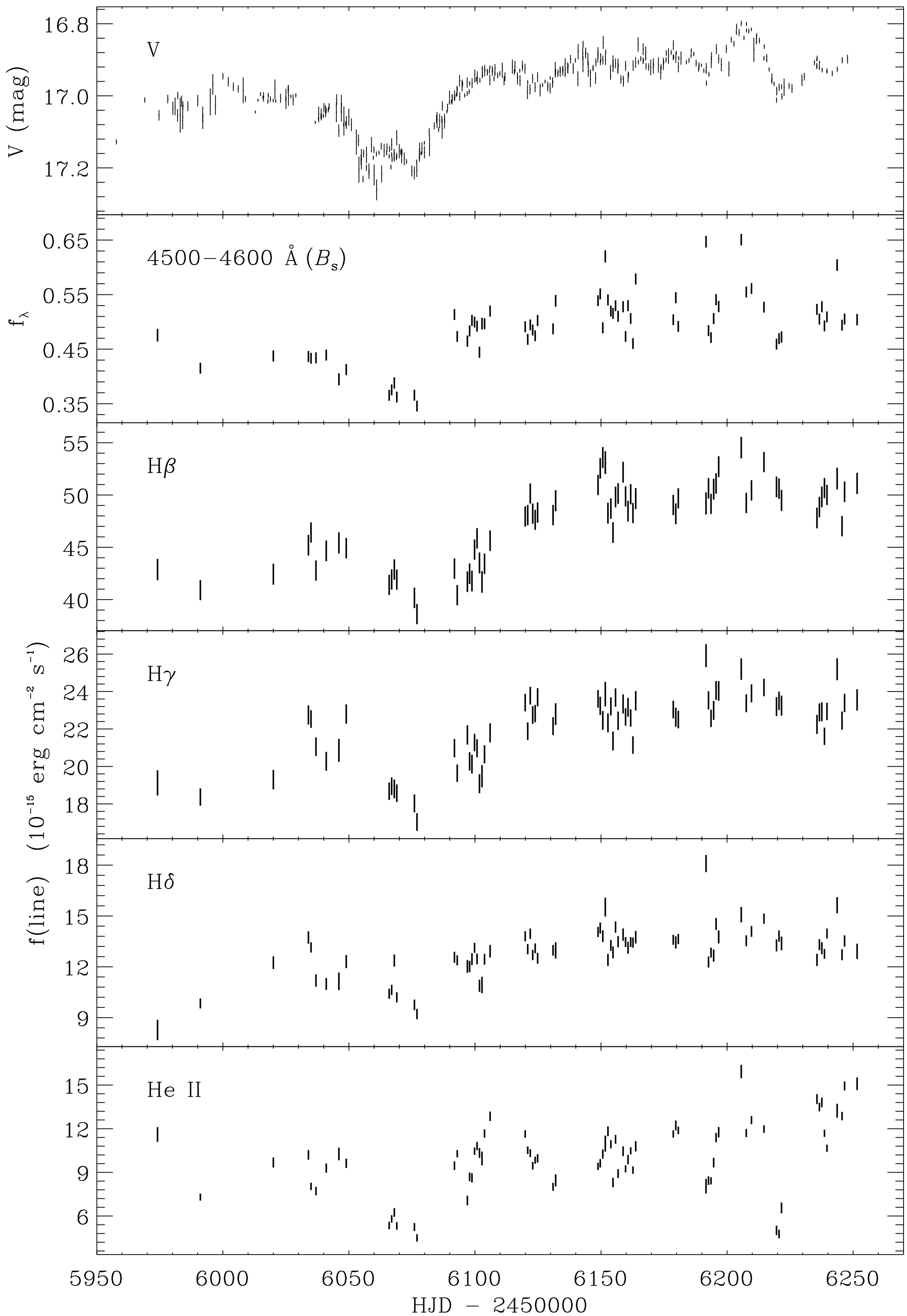

Figure 2.6: KA1858+4850 V-band magnitude, continuum flux measured from the spectroscopic data, and emission-line light curves. Plotted errors include the 2% flux scatter found by computing the normalized excess variance of the [O III] light curve.

Table 2.5. Light-Curve Statistics

Light Curve	$F_{\rm var}$	$R_{\rm max}$
V	0.084	1.50 ± 0.05
$B_{\rm s}$	0.119	1.88 ± 0.07
Hβ	0.076	1.41 ± 0.05
Hγ	0.078	1.52 ± 0.07
Hδ	0.111	2.19 ± 0.13
He II	0.245	3.54 ± 0.26

Note. — $R_{\rm max}$ and $F_{\rm var}$ values for V, $B_{\rm s}$, and the four emission lines. Higher-ionization lines show larger variations.

Figure 2.7 shows the mean and rms spectra of KA1858+4850 constructed from all blue-side spectra taken with the 600/4310 grism after applying [O III] spectral scaling. The rms spectrum indicates the amount of relative variability at each wavelength. The [O III] narrow lines have low residuals in the rms spectrum, indicating good spectral flux calibration results using the [O III] lines. The broad Balmer lines clearly stand out with very high variability. He II appears to be highly variable in the rms spectrum, even though the line is weak in the mean spectrum owing to blending with Fe II lines.

2.6 Lag Measurements

2.6.1 Cross-Correlation Measurements

We calculated the lag between the continuum and each emission-line light curve illustrated in Figure 2.6, as well as between the photometric and spectroscopic light curves, by employing the interpolation cross-correlation technique developed by Gaskell & Peterson (1987) and

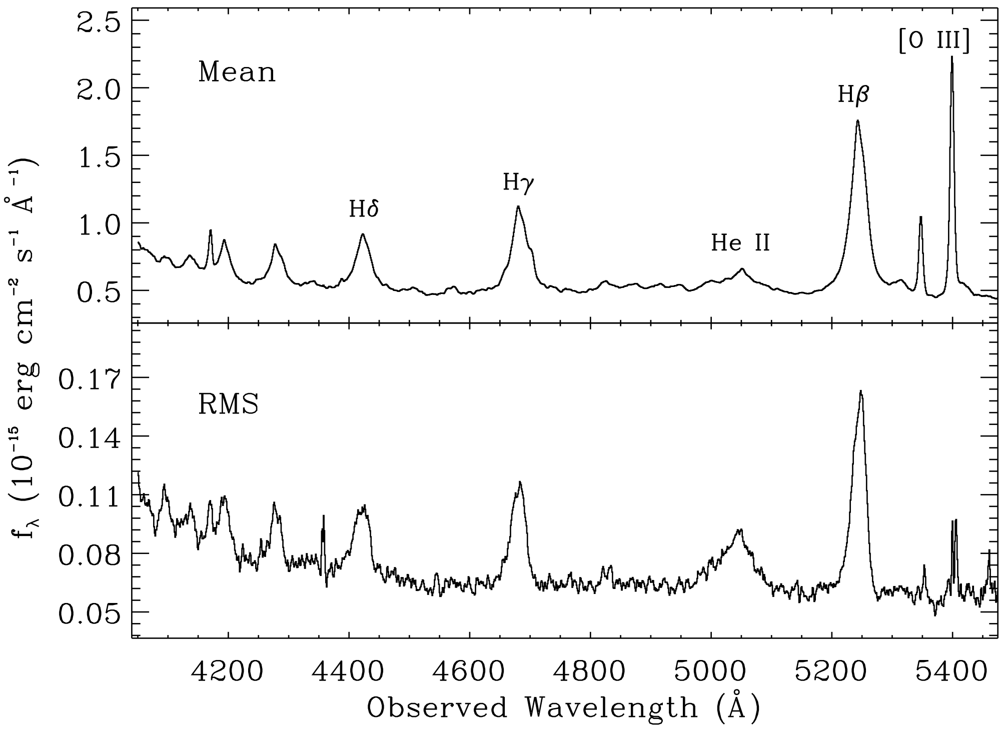

Figure 2.7: Mean and rms spectra of KA1858+4850.

described by White & Peterson (1994), Peterson et al. (2004), and Bentz et al. (2009a). We computed the cross-correlation function (CCF) for τ values from -20 to 40 days in increments of 0.25 days. The lag for each emission line is then calculated in two ways: by using the peak of the CCF, defined as $\tau_{\rm peak}$, and by using the centroid of CCF values above 80% of the peak value, defined as $\tau_{\rm cen}$. We opted to use $\tau_{\rm cen}$ for $M_{\rm BH}$ estimates as Peterson et al. (2004) showed that this yields more consistent black hole mass estimates between different emission lines.

In cases where the continuum light curve exhibits distinct global trends, a detrending procedure is sometimes applied prior to cross-correlation analysis, where a linear function is fitted to and subtracted from the light curve so that only local variations are taken into account in the cross-correlation. We computed the Hβ lag both with and without detrending using a linear fit. In the case without detrending, the lag uncertainties are smaller and the CCF peak is higher, indicating a more robust CCF. Therefore, we chose to omit the detrending procedure f6r our final cross-correlation analysis. The top panel in Figure 2.8 shows the CCF for the four emission-line light curves with the photometric light curve. We also computed the auto-correlation function (ACF) for the photometric light curve, which peaks at zero lag as expected.

To determine the final lags and their uncertainties, we employed the same Monte Carlo bootstrapping method used by Barth et al. (2011b) and described by White & Peterson (1994) and Peterson et al. (2004). We constructed 10^4 modified realizations of the continuum and emission-line light curves. Each realization is made by randomly choosing n data points from the actual light curve allowing resampling, where n is the total number of points in the dataset. If a point is picked m times, then its uncertainty is reduced by a factor of $m^{1/2}$. The simulated light curves are then varied by adding random Gaussian noise based on the measured uncertainties at each data point. We then computed the CCF for each pair of simulated continuum and line light curves to construct distributions of $\tau_{\rm cen}$ values. The median values are chosen as the final lag results, and the uncertainties on $\tau_{\rm cen}$ are the 1σ thresholds in the distribution centered around the median.

Table 3.4 gives the measured $\tau_{\rm peak}$ and $\tau_{\rm cen}$ values for the four emission-line light curves with respect to the V-band light curve. The He II lag is consistent with zero within 1σ uncertainties. The larger fractional uncertainties on the higher-order Balmer line lags, as well as on the He II lag, can be attributed to their noisier light curves due to less precise spectral scaling at wavelengths farther from [O III].

The lag times are progressively shorter for higher-order Balmer lines. Specifically, we find lag ratios of $\tau(\mathrm{H}\beta)$:$\tau(\mathrm{H}\gamma)$:$\tau(\mathrm{H}\delta)$=1.00:0.75:0.44. This is consistent with the picture of a BLR stratified in optical depth (Rees et al., 1989; Korista & Goad, 2004), as well as with findings from previous reverberation mapping campaigns (e.g. Bentz et al., 2010b).

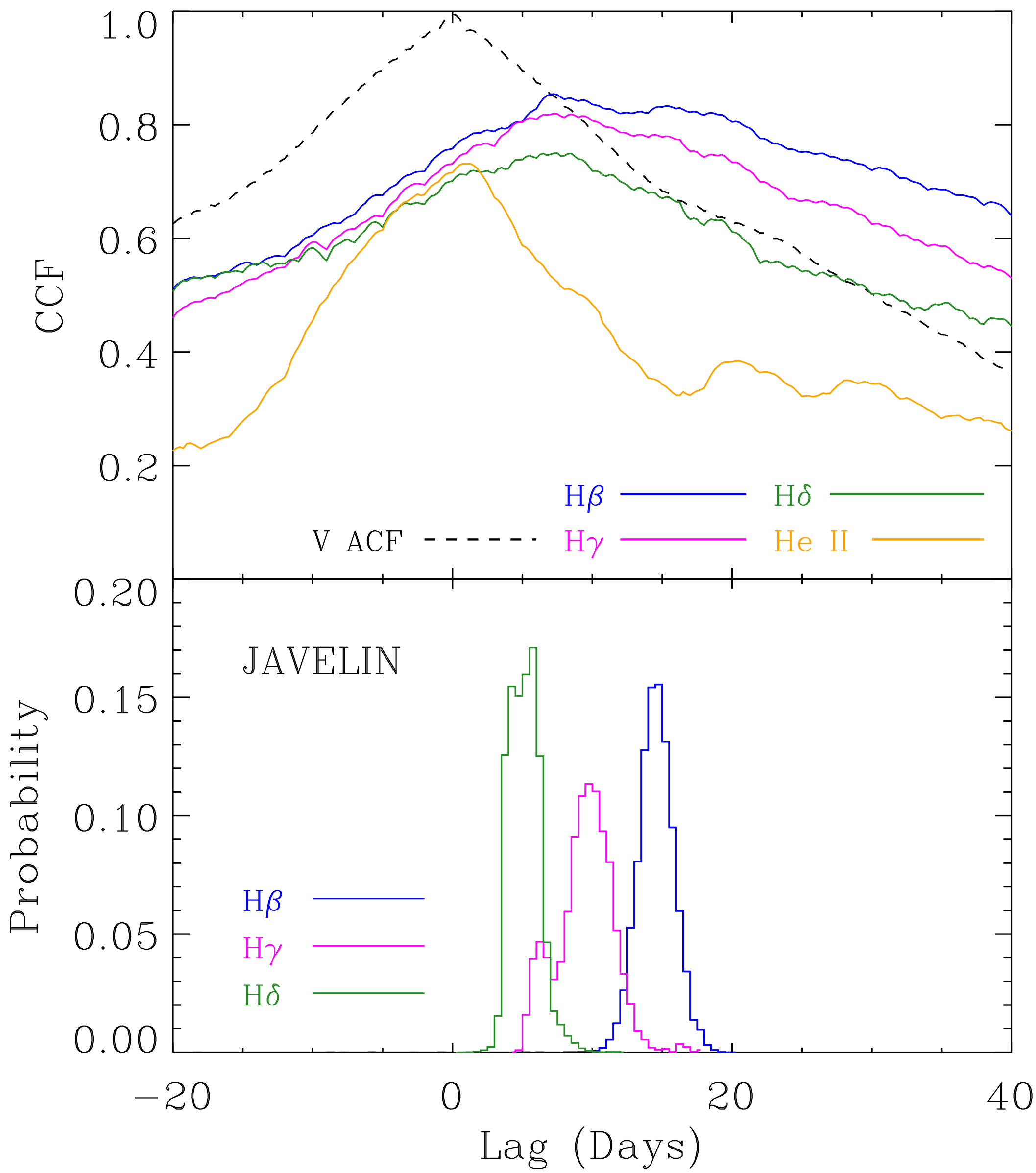

Figure 2.8: *Top*: Cross-correlation functions between the four emission lines and the V-band continuum, and the auto-correlation function of the V-band continuum. *Bottom*: Probability distributions of `JAVELIN` lags for Hβ, Hγ, and Hδ. These distributions were obtained with 6.25×10^4 iterations, while the He II distribution was obtained with 2.5×10^5 iterations. However, the He II distribution is poorly constrained owing to the line's noisy light curve, and is therefore omitted in this plot.

Table 2.6. Observed-Frame Lag Measurements

Emission Line	$\tau_{\rm peak}$ (days)	$\tau_{\rm cen}$ (days)	$\tau_{\tt JAVELIN}$ (days)
Hβ vs. V	$8.25^{+7.25}_{-1.00}$	$14.58^{+2.19}_{-2.50}$	$14.18^{+1.16}_{-1.08}$
Hγ vs. V	$7.50^{+2.00}_{-1.25}$	$10.96^{+3.08}_{-2.76}$	$10.04^{+1.42}_{-1.48}$
Hδ vs. V	$6.50^{+1.75}_{-2.00}$	$6.42^{+2.53}_{-2.60}$	$5.81^{+1.06}_{-2.03}$
He II vs. V	$0.75^{+0.50}_{-0.50}$	$-0.58^{+1.20}_{-0.85}$	$-2.86^{+2.01}_{-0.08}$
Hβ blue vs. V	$7.25^{+1.00}_{-0.75}$	$13.43^{+2.17}_{-2.62}$	$13.85^{+1.22}_{-1.23}$
Hβ core vs. V	$15.00^{+3.75}_{-6.50}$	$15.50^{+1.92}_{-2.01}$	$14.73^{+0.90}_{-0.89}$
Hβ red vs. V	$8.50^{+5.75}_{-1.25}$	$12.89^{+3.64}_{-3.20}$	$14.25^{+1.28}_{-1.26}$
Hβ vs. $B_{\rm s}$	$11.50^{+5.50}_{-4.00}$	$14.89^{+4.19}_{-5.10}$	$15.67^{+1.20}_{-1.62}$
V vs. $B_{\rm s}$	$2.25^{+1.25}_{-2.75}$	$1.68^{+2.21}_{-1.39}$	$1.64^{+0.30}_{-0.73}$
Hβ vs. *Kepler*	$8.25^{+6.50}_{-1.00}$	$14.17^{+2.26}_{-2.66}$	$13.42^{+1.10}_{-1.10}$
Hγ vs. *Kepler*	$6.75^{+1.50}_{-1.25}$	$9.49^{+3.02}_{-2.24}$	$9.10^{+0.93}_{-0.89}$
Hδ vs. *Kepler*	$4.50^{+1.75}_{-1.75}$	$4.86^{+2.78}_{-2.27}$	$4.86^{+0.86}_{-0.73}$
He II vs. *Kepler*	$0.00^{+0.50}_{-0.75}$	$-0.72^{+0.72}_{-0.72}$	$0.88^{+0.03}_{-0.03}$
Kepler vs. V	$0.50^{+0.25}_{-0.00}$	$1.00^{+0.47}_{-0.47}$	$0.76^{+0.31}_{-0.30}$
Kepler vs. $B_{\rm s}$	$1.75^{+1.50}_{-1.25}$	$1.95^{+1.28}_{-1.16}$	$2.06^{+0.15}_{-2.15}$

Note. — Cross-correlation $\tau_{\rm peak}$, cross-correlation $\tau_{\rm cen}$, and `JAVELIN` lags. Observed-frame lags can be converted to rest-frame lags by dividing by $1+z$.

Additionally, we attempted to obtain velocity-resolved lag measurements for KA1858+4850, since the lag behavior as a function of velocity across broad emission lines can contain information about BLR kinematics. We divided the Hβ line profile into three wavelength segments: 5200−5238 Å for the blue wing, 5239−5249 Å for the core, and 5250−5290 Å for the red wing. The Hβ lag for each segment is listed in Table 3.4. We found marginal evidence for longer lag in the emission-line core and shorter lags in the wings. We were unable to obtain useful lag measurements for smaller velocity bins, and therefore refrain from drawing any definitive conclusions regarding the kinematics of the BLR.

2.6.2 `JAVELIN`

We used an alternative method of estimating emission-line lags, which employs a statistical model for quasar variability. This method uses the *Python* code `JAVELIN` v.0.3α (Zu et al., 2011) to model the optical AGN continuum variability as a damped random walk process with covariance function

$$S_{\mathrm{DRW}}(\Delta t) = \sigma^2 \exp\left(-\left|\frac{\Delta t}{\tau_{\mathrm{r}}}\right|\right), \tag{2.5}$$

where τ_{r} is the "relaxation time" required for the variability to become roughly uncorrelated, and σ is the variability amplitude on timescales much shorter than τ_{r} (Kelly et al., 2009). `JAVELIN` fits τ_{r} and σ for the AGN continuum light curve, then models the emission-line light curves as lagged, smoothed, and scaled versions of the continuum light curve. An important caveat of using `JAVELIN` for the KA1858+4850 lag analysis is that the Kelly et al. (2009) damped random walk model produces variability power spectra with a slope of −2, while Mushotzky et al. (2011) showed that KA1858+4850 has a power-spectrum slope of ~ -3.

The V-band light curve was rebinned into one-day intervals for analysis with `JAVELIN` in order to cut down on computation time. While `JAVELIN` is, in principle, able to fit a large number of emission-line light curves simultaneously, the lags were poorly constrained in this case for fitting three emission-line light curves simultaneously, most likely because of the monthly gaps in the data when the Moon was bright. Therefore, we chose the two-line analysis method, where we fit each of Hγ, Hδ, and He II emission-line light curves simultaneously with that of Hβ. The Hβ lags computed from pairing with Hγ and Hδ are consistent with each other, while the Hβ lag computed from pairing with He II yielded a slightly shorter lag. This is likely due to the noisy He II light curve as well as the fact that He II intrinsically has a lag that is very short compared to the monthly gaps in the light curves, which makes the lag difficult to measure. We use the Hβ lag value obtained from pairing with Hγ as $\tau_{\texttt{JAVELIN}}$ for Hβ.

Table 3.4 lists the `JAVELIN` lags, which are consistent with those obtained using cross-correlation techniques within 1σ uncertainties. Lags for the Hβ blue wing, core, and red wing were computed simultaneously in a three-line `JAVELIN` run, and the V-band and Hβ lags with respect to the $B_{\rm s}$ band were obtained from a two-line run. The bottom panel of Figure 2.8 shows the `JAVELIN` distributions for Hβ, Hγ, and Hδ lags, and Figure 2.9 shows the `JAVELIN` model results for the continuum, Hβ, and Hγ light curves.

We note that both the CCF and `JAVELIN` He II lags are slightly negative, which is likely caused by the combined effects of the higher ionization (and therefore shorter lag) of He II, and a slight contaminating lag signal in the V-band light curve, described in the next section.

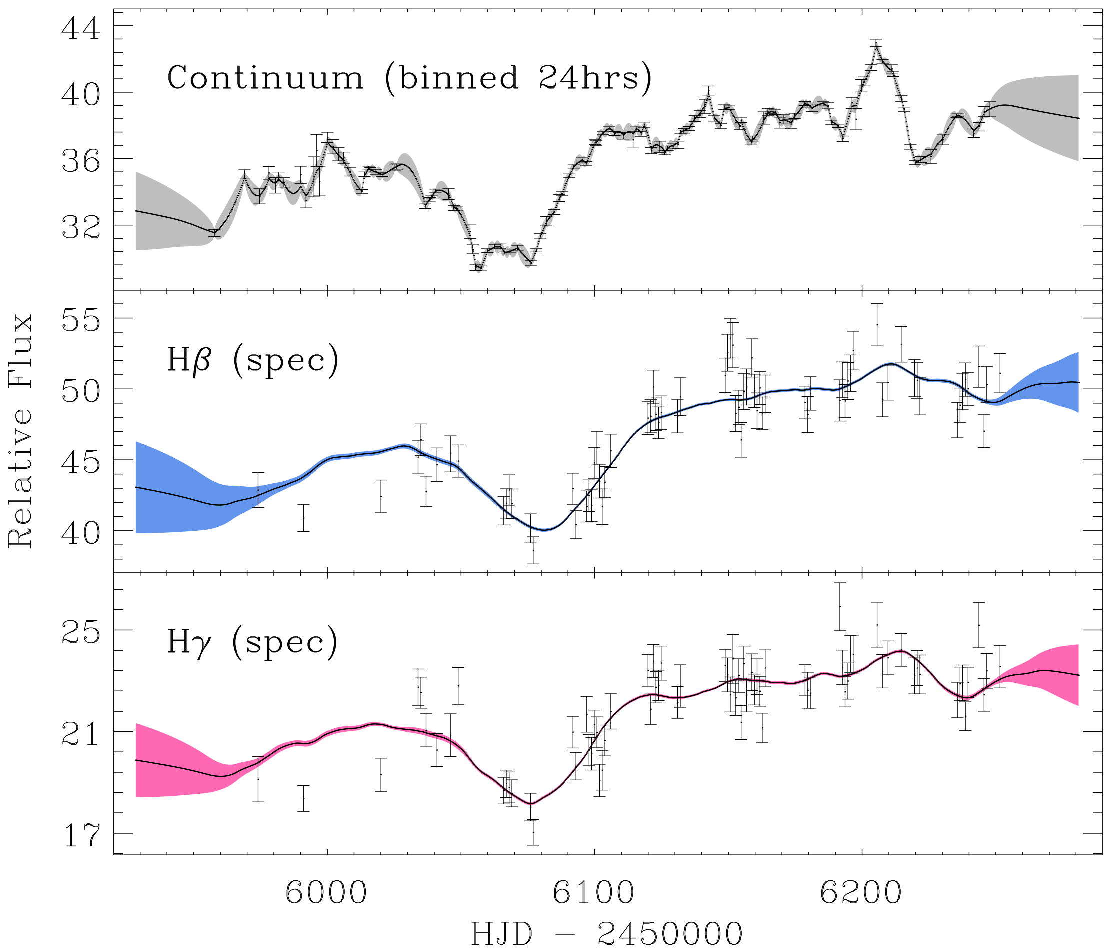

Figure 2.9: **JAVELIN** model results for the continuum (V band), Hβ (spectroscopic), and Hγ (spectroscopic) light curves (black solid lines), the model 1σ uncertainties at each time (shaded regions), and observational data and uncertainties.

2.6.3 Hβ Contamination in the V band

There is a small biasing factor in the Hβ lag calculations from the emission-line contribution to the V-band flux. While the V-band light curve would ideally represent pure continuum, the presence of the Hβ line in the V filter adds a flux component that contains a lag signal. Consequently, the calculated lags from the biased continuum would be shorter than those obtained with a pure continuum.

To determine the magnitude of this contribution, we first combined the blue- and red-side spectra from a single night, and next performed synthetic photometry on the spectrum using a Johnson V filter. We then removed the Hβ line from the spectrum by directly interpolating over it, performed synthetic photometry on the modified spectrum, and compared the two magnitude results. We found that Hβ contributes approximately 9.6% of the V-band flux, and assume that Hβ dominates the variable emission-line contribution in the V band and is therefore the main source of the lag bias.

To quantify the effect of this bias on the calculated lag, we simulated 10^4 pure AGN continuum light curves using methods described by Timmer & Koenig (1995), and simulated corresponding emission-line light curves by convolving the continuum light curves with a δ function at a lag of 14 days. We then simulated 10^4 contaminated V-band light curves by adding a lagged emission-line contribution to the continuum at the 9.6% level. The pure and contaminated continuum light curves in each pair are both then cross-correlated with the corresponding emission-line light curve to create two distributions of lag times. We found a median lag of 14.0 ± 2.1 days for the pure continuum case and a median lag of 13.2 ± 2.1 days for the contaminated continuum case, indicating an expected bias of 0.8 days. This prediction is similar to the bias we find from observations.

We found an Hβ lag of $14.89^{+4.19}_{-5.10}$ days with respect to B_{s}, which contains no Hβ flux contamination, indicating an observed bias of $\sim$0.3 days compared to the lag-contaminated case. We also found a small positive lag of $1.68^{+2.21}_{-1.39}$ days for the V light curve with respect to $B_{\rm s}$. However, in both simulations and observations, the biases are smaller than the lag uncertainties for Hβ with respect to the V-band light curve. We therefore conclude that the lag bias due to Hβ flux contribution in the V band is present, but is small compared to the 1σ uncertainties on the $\tau_{\rm cen}$ measurements.

2.6.4 Lags with Respect to the *Kepler* Light Curve

We computed the lag of each emission line with respect to the scaled *Kepler* fluxes using both cross-correlation analysis and `JAVELIN`. The *Kepler* light curve has a cadence of 30 minutes, giving a total of $\sim 1.3 \times 10^4$ data points over three quarters. We binned the light curve into bins of 12 and 24 hours to use in the cross-correlation and `JAVELIN` analyses, respectively. For both CCF and `JAVELIN`, we found the emission-line lags with respect to the *Kepler* light curve, listed in Table 3.4, to be consistent with but slightly shorter than those with respect to the V-band continuum. This is consistent with expectations, since the *Kepler* passband includes Hα, which introduces an additional lag signal to the *Kepler* light curve compared to the V-band data. The redder portion of the continuum could also have a small lag with respect to the bluer continuum (Sergeev et al., 2005), since the redder continuum emission comes from larger radii in the accretion disk than where the V-band continuum is emitted. The combined effects of broad emission lines and red continuum in the *Kepler* band should account for the shorter emission-line lags measured against the *Kepler* light curve as compared to those measured against the V-band light curve.

We also measured the lag of the *Kepler* light curve with respect to both the V-band and $B_{\rm s}$-band light curves, and found small positive lags for both cases. This also supports the idea of broad emission lines and the red continuum introducing a lag signal to the *Kepler* light curve.

2.7 Line Widths and Black Hole Mass Estimate

There are two conventional methods of measuring the broad-line width: using the FWHM and the line dispersion (σ_{line}) of the emission-line profile. The line profile is typically taken to be the rms profile, since using the variable portion of the spectrum instead of the mean spectrum implies a black hole mass estimate based only on components of the emission line that echo the continuum signal (Peterson et al., 2004). The line dispersion is defined as

$$\sigma_{\text{line}}^2 = \left(\frac{c}{\lambda_0}\right)^2 \left(\frac{\sum \lambda_i^2 S_i}{\sum S_i} - \lambda_0^2\right), \tag{2.6}$$

where S_i is the flux density at wavelength bin λ_i and λ_0 is the flux-weighted centroid wavelength of the line profile. In this empirical method of measuring the line width, the line profile is not fitted to any functional model. We used the same line and continuum windows to measure the line width as those used in measuring line fluxes.

To determine the final FWHM and σ_{line} values and uncertainties, we employed the bootstrap method described by Peterson et al. (2004). The entire dataset contains N spectra. For each bootstrap realization, we randomly selected N spectra from the dataset allowing reselection, constructed the mean and rms line profiles from this randomly sampled set, and measured the line dispersion of the rms profile. From multiple realizations, we built up a distribution of FWHM and line-dispersion values, and took the median and standard deviation of the distributions to be the final FWHM and σ_{line} and their uncertainties, respectively. We removed the instrumental line width by taking the width of the λ5086 Cd I calibration line in a $2''$-slit width exposure and subtracting it from the measured FWHM or σ_{line} in quadrature. We found FWHM = 324 km s^{-1} for the Cd I calibration line for a Gaussian fit to the line profile. After correcting for the instrumental line width, we found FWHM = 1511 ± 68 km s^{-1} and $\sigma_{\rm line} = 770 \pm 49$ km s^{-1} for the Hβ line in the rms spectrum.

We also measured the Hβ FWHM and $\sigma_{\rm line}$ for the mean profile. To ensure exclusion of the narrow-line component in the width measurements, we measured the FWHM and $\sigma_{\rm line}$ of the broad Hβ model based on the spectral decomposition of the mean spectrum, as shown in Figure 2.5. The [O III] narrow-line profile was used to model the narrow Hβ line in the spectral fitting routines, and $f(\mathrm{H}\beta_{\rm narrow})/f([\mathrm{O~III}]_{\lambda5007}) \approx 0.09$. We also measured the FWHM and $\sigma_{\rm line}$ of the broad Hβ model for each epoch in our dataset, and took the standard deviations about the means to be the FWHM and $\sigma_{\rm line}$ uncertainties. We found FWHM $= 1820 \pm 79$ km s^{-1} and $\sigma_{\rm line} = 853 \pm 34$ km s^{-1} for Hβ in the mean spectrum after subtracting the instrumental line width. This is consistent with previous findings that line widths measured from mean spectra tend to be larger than those measured from rms spectra (e.g. Bentz et al., 2009a).

The reverberation lag and line width of Hβ combined can give a virial estimate of the central black hole mass, given by

$$M_{\rm BH} = f\frac{(c\tau)(\Delta V)^2}{G}, \tag{2.7}$$

where τ is the Hβ lag time with respect to the continuum and $c\tau$ gives the mean radius of the BLR, ΔV is the Hβ line width, G is the gravitational constant, and f is a scaling factor of order unity that depends on the inclination and kinematics of the BLR. Traditionally, since these properties of the BLR are usually unknown, the scale factor f is chosen to be a value that brings the set of reverberation mapped AGNs into agreement with local quiescent galaxies in the $M_{\rm BH} - \sigma_\star$ relation, which relates black hole mass to host-galaxy bulge stellar velocity dispersion (Onken et al., 2004; Woo et al., 2010; Park et al., 2012a;

Grier et al., 2013).

We use $c\tau_{\rm cen}$ for the BLR radius and Hβ line dispersion $\sigma_{\rm line}$ of the rms line profile for ΔV, for consistency with Peterson et al. (2004), and a scale factor of $f = 5.13$, calculated by Park et al. (2012a) based on the updated local AGN $M_{\rm BH} - \sigma_\star$ relation obtained with the forward regression method. Combining the Hβ vs. V lag of $14.58^{+2.19}_{-2.50}$ days, corresponding to a rest-frame lag of $\tau_{\rm cen} = 13.53^{+2.03}_{-2.32}$ days, and $\sigma_{\rm line} = 770 \pm 49$ km s^{-1}, we obtain a virial black hole mass estimate of $M_{\rm BH} = 8.06^{+1.59}_{-1.72} \times 10^6\ M_\odot$. If we follow the prescription of Grier et al. (2013) by using the Hβ $\tau_{\texttt{JAVELIN}}$ and a scale factor $f = 4.31$, we find $M_{\rm BH,\texttt{JAVELIN}} = 6.58^{+1.00}_{-0.98} \times 10^6\ M_\odot$.

The above uncertainties on $M_{\rm BH}$ include only errors propagated from the lag and emission-line-width measurements. If we incorporate the uncertainties on the mean scale factor from the linear fits by Park et al. (2012a), $f = 5.13 \pm 1.30$, then our black hole mass estimate becomes $M_{\rm BH} = 8.06^{+2.58}_{-2.67} \times 10^6\ M_\odot$. It is evident that true uncertainties on the virial estimate of $M_{\rm BH}$ are dominated by the systematic uncertainties in the scale factor, which are significantly larger than those derived from the lag and line-width measurements alone.

We note that there are other estimates of the scale factor, such as those obtained by separating galaxies into different populations based on mass (Greene et al., 2010) and morphology (Graham et al., 2011), which yield estimates of f different from that of Park et al. (2012a) by up to a factor of $\sim$2. For example, Woo et al. (2013) investigated the scale factor for both quiescent and active galaxies as a combined sample and found $f = 5.9^{+2.1}_{-1.5}$. Furthermore, recent work by Ho & Kim (2014) showed that the scale factor can be different for galaxies with pseudobulges and classical buldges, with $f = 3.2 \pm 0.7$ for pseudobulges and $f = 6.3 \pm 1.5$ for classical bulges. Various ongoing efforts that further examine the $M_{\rm BH} - \sigma_\star$ relation for local galaxies will improve the precision of the scale factor in the near future as the number of reverberation mapped AGNs increases. Moreover, there has been progress in constraining f for individual galaxies by dynamically modeling the BLR (Pancoast et al., 2013).

Table 2.7. Line Widths, Lags, and Derived Black Hole Masses

Emission Line	$\sigma_{\rm line}$ (km s^{-1})	Computation Method	$\tau_{\rm cen,rest}$ (days)	$M_{\rm BH}$ (10^6 $M_\odot$)
Hβ	770 ± 49	CCF	$13.53^{+2.03}_{-2.32}$	$8.06^{+1.59}_{-1.72}$
		`JAVELIN`	$13.15^{+1.08}_{-1.00}$	$6.85^{+1.00}_{-0.98}$
Hγ	741 ± 73	CCF	$10.17^{+2.86}_{-2.56}$	$5.59^{+1.92}_{-1.79}$
		`JAVELIN`	$9.31^{+1.32}_{-1.37}$	$3.99^{+0.97}_{-0.98}$
Hδ	827 ± 83	CCF	$5.96^{+2.35}_{-2.41}$	$4.20^{+1.85}_{-1.89}$
		`JAVELIN`	$5.39^{+0.98}_{-1.88}$	$3.19^{+0.86}_{-1.28}$

Note. — Line lags are measured against the V-band continuum. $M_{\rm BH}$ from CCF lags were calculated using $f = 5.13$ (Park et al., 2012a), and $M_{\rm BH}$ from `JAVELIN` lags were calculated using $f = 4.31$ (Grier et al., 2013).

In addition, we obtained $M_{\rm BH}$ estimates using the broad Hγ and Hδ lines. No lag estimate was attempted using He II since the line has a negative lag. The line widths, rest-frame lags, and derived $M_{\rm BH}$ values are listed in Table 2.7. The Hγ and Hδ light curves are significantly noisier than that of Hβ; thus, it is not surprising that, for both CCF and `JAVELIN` cases, the derived $M_{\rm BH}$ values have much higher fractional uncertainties compared to the Hβ $M_{\rm BH}$. For both CCF and `JAVELIN` lags, the Hγ $M_{\rm BH}$ estimates, though consistent with the Hβ $M_{\rm BH}$ values within 1σ uncertainties, are slightly smaller than those of Hβ, and $M_{\rm BH}$ estimates for Hδ are smaller still. This may be due to the fact that we are using the same f factor for all the emission lines, while the stratified nature of the BLR may imply different scale factors for each line that depend on the geometry and kinematics of the line-emitting gas.

We would like to compare KA1858+4850 to other AGNs having similar black hole masses by studying its location on the $M_{\rm BH} - \sigma_\star$ relation as well as the $M_{\rm BH} - L_{\rm bulge}$ relation (black hole mass vs. host-galaxy bulge luminosity). However, because KA1858+4850 appears point-like at ground-based resolution, it is impossible to observe structural properties of the host galaxy without high-resolution images from the *Hubble Space Telescope (HST)* or ground-based observations using adaptive optics. Additionally, our Lick spectra cannot be used to measure stellar velocity dispersion in KA1858+4850 owing to the galaxy's weak starlight component compared to its AGN luminosity.

2.8 Eddington Ratio

AGNs have been observed to follow a tight correlation between the size of the BLR ($R_{\rm BLR}$) and continuum luminosity (L_λ). The $R_{\rm BLR} - L_\lambda$ relation can be written in the form

$$\log\left(\frac{R_{\rm BLR}}{1\ \text{lt-day}}\right) = K + \alpha\log\left(\frac{\lambda L_\lambda}{10^{44}\ \text{erg s}^{-1}}\right), \tag{2.8}$$

where L_λ is measured at $\lambda_{\rm rest} = 5100$ Å. Bentz et al. (2013) found the values of K and α to be $1.560^{+0.024}_{-0.024}$ and $0.546^{+0.027}_{-0.027}$ respectively, with a scatter of around 0.13 dex for their best fit. From these parameters and the lag for KA1858+4850, we expect to find $\lambda L_\lambda(5100\ \text{Å}) = 1.64^{+0.59}_{-0.65} \times 10^{43}$ erg s^{-1}. We used combined Kast blue- and red-side spectra to measure L_λ and adopted the spectral fitting components for the mean spectrum (shown in Figure 2.5) to estimate the starlight contribution in this region, which we found to be approximately 40% of the total flux. Correcting for Galactic extinction, we roughly estimate $\lambda f_\lambda(5100\ \text{Å}) \approx 1.6 \times 10^{-12}$ erg cm^{-2} s^{-1} for the AGN, corresponding to $\lambda L_\lambda(5100\ \text{Å}) \approx 2.4 \times 10^{43}$ erg s^{-1} for a luminosity distance of 354 Mpc. (We assume the same standard ΛCDM cosmology as Bentz et al. 2013, where $H_0 = 72$ km s^{-1} Mpc^{-1}, $\Omega_{\rm M} = 0.3$, and $\Omega_\Lambda = 0.7$.) This is consistent with expectations given the scatter in the fit values from Bentz et al. (2013).

KA1858+4850 is a NLS1, a class of objects thought to have high $L/L_{\rm Edd}$ (Pogge 2011, and references therein). We apply the bolometric correction used by Kaspi et al. (2000), where

$L_{\rm bol} \approx 9\,\lambda L_\lambda(5100$ Å), and obtain an estimate of $L_{\rm bol} = 2.2 \times 10^{44}$ erg s^{-1} and $L/L_{\rm Edd} \approx 0.2$ using $M_{\rm BH} = 8.06^{+1.59}_{-1.72} \times 10^6\ M_\odot$. We compared this Eddington ratio to those of the four LAMP 2008 NLS1 galaxies, which were calculated using black hole masses published by Bentz et al. (2009a) and $\lambda L_\lambda(5100$ Å) values given in Bentz et al. (2013). After applying the same bolometric correction as for KA1858+4850, we found $L/L_{\rm Edd} = [0.5, 0.7, 1.2, 0.9]$ for Mrk 1310, Mrk 202, NGC 4253, and NGC 4748, respectively. Compared to these NLS1s, KA1858+4850 has a significantly lower Eddington ratio.

A recent study by Du et al. (2014) measured the Hβ lag and $M_{\rm BH}$ of three NLS1 galaxies (Mrk 335, Mrk 142, and IRAS F12397), all of which appear spectroscopically similar to KA1858+4850. The authors compute the Eddington rate based on a thin accretion disk model (Shakura & Sunyaev, 1973). This rate, denoted by $\dot{m}_{\rm ss}$, is written as

$$\dot{m}_{\rm ss} \approx 20.1 \left(\frac{L_{44}}{\cos\, i}\right)^{3/2} M_7^{-2} \eta_{\rm ss}, \tag{2.9}$$

where they define $L_{44} = \lambda L_\lambda / 10^{44}$ erg s^{-1} at $\lambda = 5100$ Å, $M_7 = M_{\rm BH}/10^7 M_\odot$, and $\cos\, i = 0.75$ as the inclination typical of Type 1 AGNs. For a minimal radiative efficiency of $\eta_{ss} = 0.038$, they find Eddington ratios of 0.6, 2.3, and 4.6 for Mrk 335, Mrk 142, and IRAS F12397, respectively. Applying this same prescription to KA1858+4850, with $M_7 = 0.81$ and $L_{44} = 0.24$, we find $\dot{m}_{\rm ss} = 0.2$, in agreement with our $L/L_{\rm Edd}$ value obtained using the Kaspi et al. (2000) bolometric correction.

Chapter 3

Optical Spectroscopic Analysis of the Broad Line Region in NGC 5548

3.1 Background

In RM, the far-UV continuum ideally should be used to derive emission-line lags and BLR sizes because this continuum, at $\lambda \cong 1100 - 1500$ Å, is closer in wavelength to the source of the ionizing continuum at < 912 Å, and therefore should be a more accurate proxy for the ionizing continuum. However, wavelengths shorter than 3200 Å are inaccessible from the ground, so the rest-frame optical continuum is often used instead as a proxy for the ionizing source in low-redshift AGN. Although the far-UV and optical continua have been shown to vary almost simultaneously in some cases (e.g. Clavel et al., 1991; Reichert et al., 1994; Korista et al., 1995; Wanders et al., 1997), more recent studies have found that the optical continuum lags the UV by up to a few days in other AGN (Collier et al., 1998; Sergeev et al., 2005; McHardy et al., 2014; Shappee et al., 2014; Edelson et al., 2015; Fausnaugh et al., 2016). The optical continuum has also been shown to have smoother variation features and smaller variation amplitude compared to its UV counterpart (e.g. Peterson et al., 1991; Dietrich et al., 1993; Stirpe et al., 1994; Santos-Lleó et al., 1997; Dietrich et al., 1998; Shappee et al., 2014; Fausnaugh et al., 2016). These differences between the UV and optical continua suggest that the optical continuum is not necessarily interchangeable with the ionizing source.

Furthermore, a long-standing assumption in RM is that the size of the source of the incident ionizing photons in a typical Seyfert galaxy is much smaller than the BLR (about a factor of 100, e.g. Peterson, 1993; Peterson & Horne, 2004). This assumption implies that the disk size can be neglected when determining the BLR radius from RM data. However, Fausnaugh et al. (2016) have shown that the optically emitting portion of the accretion disk has a lag similar to that of the inner portion of the BLR. If we assume a model in which the measured lags are purely dependent on radial distance from the ionizing source, then this means that emission-line lags measured using the optical continuum may significantly underestimate the true BLR size. Since most RM campaigns use only optical data, it is imperative that we understand the systematic effects of using the optical rather than the UV continuum in RM studies and the relevant implications for BH mass estimates.

To this end, we present the results of a six-month ground-based RM program monitoring the galaxy NGC 5548 ($z = 0.0172$). This work is the fifth in a series describing results from the AGN Space Telescope and Optical Reverberation Mapping (STORM) campaign, the most intensive multi-wavelength AGN monitoring program to date. The campaign is centered around six months of daily observations using the Cosmic Origins Spectrograph on the *Hubble Space Telescope* (*HST*). Concurrent with the *HST* program were four months of *Swift* observations and six months of ground-based photometric and spectroscopic observations. First results of the *HST*, *Swift*, and ground-based photometry programs were presented by De Rosa et al. (2015, DR15), Edelson et al. (2015), and Fausnaugh et al. (2016, F16). Goad et al. (2016, G16) described the anomalous decorrelation of the UV continuum and emission-line light curves during a portion of this campaign. This work will focus on the ground-based spectroscopic monitoring campaign.

NGC 5548 is one of the most well-studied Seyfert galaxies in the literature and has been the subject of many RM programs in the past. Most notably, it was the target of a 13-year campaign carried out by the AGN Watch consortium (Peterson et al., 2002, and references therein), which was initially designed to support UV monitoring of NGC 5548 carried out by the *International Ultraviolet Explorer* (*IUE;* Clavel et al., 1991). Subsequently, NGC 5548 was monitored in programs described by Bentz et al. (2007), Denney et al. (2009), and Bentz et al. (2009b), with campaign durations of 40 days, 135 days, and 64 days respectively. The 2014 AGN STORM campaign lasted six months and obtained nearly daily observations over a wide wavelength range. This combination of high cadence, long duration and multi-wavelength coverage makes this the most intensive RM campaign ever conducted.

There are two primary goals of the present work. The first is to compare the Hβ emission-line lag measured against simultaneously observed far-UV and optical continua in order to understand the effects of using the rest-frame optical continuum instead of the UV continuum when calculating Hβ lags. The second goal is to compare the responses of the optical and UV emission lines to continuum variations. This will provide a more complete picture of the structure and kinematics of the BLR than previous studies that used only optical data.

We describe the spectroscopic observations and reductions in Section 2. Section 3 details our procedures for flux and light curve measurements. In Section 4, we present our analysis of light curve lags, line responses, line profiles, and BH mass measurements. We discuss the implications of our results and compare our measurements to those from previous campaigns in Section 5. Section 6 summarizes our findings.

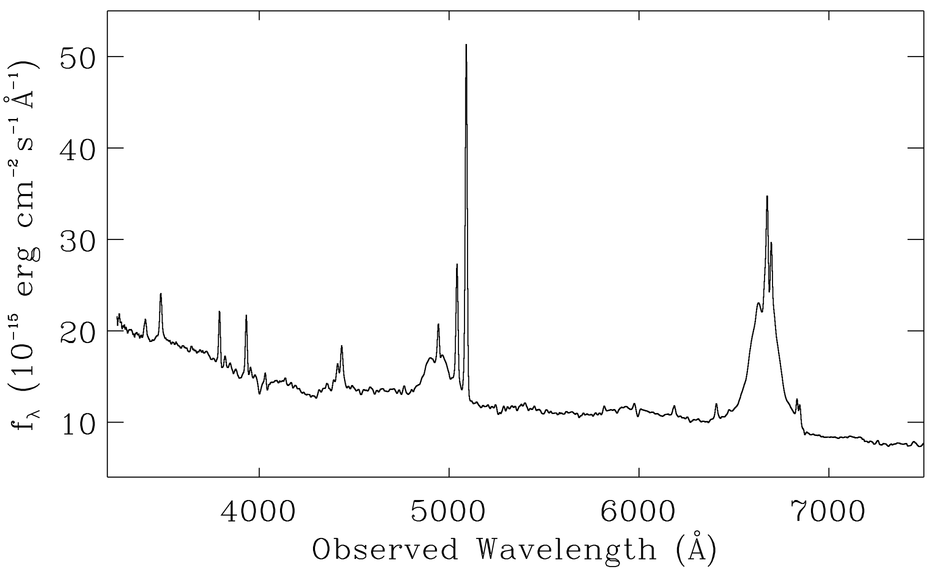

Figure 3.1: Mean spectrum of NGC 5548 from the Asiago dataset.

3.2 Observations and Data Reduction

Spectroscopic data were obtained from five telescopes: the McGraw-Hill 1.3-m telescope at the MDM Observatory, the Shane 3-m telescope at the Lick Observatory, the 1.22-m Galileo telescope at the Asiago Astrophysical Observatory, the 3.5-m telescope at Apache Point Observatory (APO), and the 2.3-m telescope at the Wyoming Infrared Observatory (WIRO). Observations at MDM were carried out with a slit width of 5″ oriented in the north-south direction, and spectra at the other telescopes were taken with a 5″-wide slit oriented at the parallactic angle. The optical spectroscopic monitoring began on 2014 January 4 and continued through 2014 July 6 with approximately daily cadence.

Table 3.1. Instrument characteristics and data reduction parameters for all telescopes

Telescope	Instrument	Number of Epochs	Median Seeing ($''$)	Wavelength Dispersion (Å pixel^{-1})	Wavelength Coverage (Å)	Pixel Scale ($''$ pixel^{-1})	Median SNR	[O III] $F_{\rm var}$ (%)
MDM	Boller & Chivens CCD Spectrograph	147	1.7	1.25	4225−5775	0.75	118	0.44
Lick	Kast Double Spectrograph	37	1.5	1.02	3460−5500	0.43	194	0.63
Asiago	Boller & Chivens CCD Spectrograph	22	4.0	1.00	3250−7920	1.00	160	0.46
APO	Dual Imaging Spectrograph	13	1.4	1.00	4180−5400	0.41	160	0.29
WIRO	WIRO Long Slit Spectrograph	6	2.1	0.74	5599−4399	0.52	217	0.23

Note. — The SNR value refers to the median SNR per pixel over the observed wavelength range 5157.6−5217.6 Å. The wavelength coverage for Lick refers to only the Kast blue-side camera.

Table 3.1 lists the properties of the telescopes and instruments used to obtain spectroscopic data, and Figure 3.1 shows the mean spectrum constructed from the Asiago dataset, which was the only dataset that covered the full optical wavelength range. MDM contributed the largest number of spectra with 147 epochs. The 37 epochs of Lick spectra were obtained by several groups of observers who used slightly different setups and calibrations. The Kast spectrograph at Lick Observatory has red-side and blue-side cameras, but since the red-side setup was very different for each group, we present only the blue-side data here. Asiago, APO, and WIRO contributed 22, 13, and 6 epochs of spectra respectively. Our analysis focuses primarily on the MDM dataset in order to maximize consistency.

Data reduction procedures included overscan subtraction, flat fielding, and cosmic ray removal using the L.A. Cosmic routine (van Dokkum, 2001b). The 1-D spectra were extracted using a width of $15''$ and consistent background sky apertures for all data, wavelength calibrated using line-lamp exposures, and flux calibrated using standard stars. Our most frequently used flux standard stars were Feige 34, BD 332642 and HZ 44. We used unweighted extractions for the AGN spectra and optimal extractions for the stellar spectra (Horne, 1986). For nights when multiple exposures were taken, the flux-calibrated 1-D spectra were combined after aligning all the spectra by applying a small wavelength shift to all but the first spectrum.

We note that the response sensitivity curve applied to each epoch of MDM data during the spectral reduction process is actually the mean of all response functions within a 10-day window centered on the date in question. Additioinally, the first 134 epochs of MDM data were flux calibrated using Feige 34, while the last 13 epochs, taken from 2014 June 20 to 2014 July 6, were flux calibrated with HZ 44. This caused spurious changes in the shape of some emission-line features, so we used only the first 134 MDM epochs for our present analysis.

3.2.1 Spectral Flux Calibrations

To place the instrumental flux values on an absolute flux scale, we measured the narrow [O III] $\lambda 5007$ line flux from spectra taken under photometric conditions and scaled each spectrum to have the same [O III] flux. There were 21 epochs identified as photometric by MDM observers. We determined the [O III] line flux for each spectrum by first subtracting a linear fit to continuum windows on either side of the line, then integrating the flux within a fixed wavelength range. We used the observed wavelength ranges 5062−5066 Å and 5114−5118 Å to fit the continuum and integrated over the range 5066.25−5113.00 Å for the line flux. We discarded the 2σ outliers from this set of [O III] flux measurements and re-computed the mean, then repeated this process, resulting in a total of 16 final photometric spectra. We used these spectra to construct a weighted mean spectrum and found its [O III] $\lambda 5007$ line flux to be $(5.01 \pm 0.11) \times 10^{-13}$ erg s^{-1} cm^{-2}. This represents our best estimate of the true [O III] flux for NGC 5548 during this campaign. For comparison, Peterson et al. (2013a) found the [O III] flux to be $(4.77 \pm 0.14) \times 10^{-13}$ erg s^{-1} cm^{-2} in their 2012 monitoring campaign. This difference is within the range of total narrow [O III] variability for NGC 5548 over the course of 21 years, as presented by Peterson et al. (2013a).

In addition to the AGN intrinsic variability, many other factors contribute to nightly variations in the spectra. These include changes in transparency due to clouds, changes in seeing conditions, inconsistent instrument focus, and mis-centering of the AGN in the slit during observations. We used the flux scaling procedure described by van Groningen & Wanders (1992b) to align the nightly spectra and place them on a consistent wavelength scale. This scaling method assumes that the narrow-line flux is constant over the monitoring period. For each spectrum in the dataset, the algorithm looks for a combination of wavelength shift, multiplicative scale, and Gaussian kernel convolution that minimizes the residual in a region containing the narrow [O III] line between each individual spectrum and a reference spectrum.

We constructed a separate reference spectrum for each telescope by averaging the highest SNR spectra in each dataset, then scaled these spectra to have the same [O III] flux as the mean photometrically calibrated MDM spectrum. This brings all spectra to a consistent flux scale. We chose the wavelength range 5067−5150 Å, which includes the [O III] λ5007 emission line and some continuum redward of the line, to be the comparison region between individual and reference spectra.

To assess the accuracy of spectral scaling, we estimated the intrinsic fractional variability, $F_{\rm var}$ of the residual [O III] λ5007 light curve after correcting for random measurement errors, defined as

$$F_{\rm var} = \frac{\sqrt{\sigma^2 - \langle\delta^2\rangle}}{\langle f\rangle}, \tag{3.1}$$

where σ^2 is the flux variance, $\langle\delta^2\rangle$ is the mean-square value of the measurement uncertainties, and $\langle f\rangle$ is the unweighted mean flux. For the [O III] λ5007 light curve, $F_{\rm var}$ gives a good estimate of the residual flux-scaling errors (Barth & Bentz, 2016). The $F_{\rm var}$ value for each telescope is listed in the last column of Table 3.1. We found $F_{\rm var}$ to be between 0.23% and 0.63% for all telescopes, meaning that there is an additional scatter of less than 1% in the [O III] light curve above the noise due to photon counting. These $F_{\rm var}$ values are consistent with or better than the best values typically obtained in ground-based campaigns. For example, Barth et al. (2015) found $F_{\rm var}$ values ranging from 0.5% to 3.3% for individual AGN in the 2011 Lick AGN Monitoring Project.

Figure 3.2 shows (in black) the mean and root-mean-squares residual (rms) spectra for the MDM dataset. The rms spectrum indicates the degree of variability at each wavelength over the course of the campaign. Both the broad Hβ and He II λ4686 emission lines exhibit strong variations, and the Hβ rms profile appears to have multiple peaks. Traditionally, the rms spectrum is constructed such that the value at each wavelength is taken to be the standard deviation of fluxes from all epochs, but this does not take into account Poisson or detector noise, which may bias the rms profile by a small amount (Barth et al., 2015). Park et al. (2012b) suggest using the SNR for each spectrum as the weight for that spectrum in calculating the rms, or using a maximum likelihood method to obtain the rms. We adopt a simpler approach that uses the excess variance as a way to exclude variations that are not intrinsic to the AGN. This "excess rms" value at each wavelength is defined as

$$\text{e-rms}_\lambda = \sqrt{\frac{1}{N-1}\sum_{i=1}^{N}[(f_{\lambda,i} - \langle f_\lambda \rangle)^2 - \delta^2_{\lambda,i}]}, \tag{3.2}$$

where N is the total number of points in the dataset, $\langle f_\lambda \rangle$ is the mean flux at each wavelength, and $f_{\lambda,i}$ and $\delta_{\lambda,i}$ are the fluxes from individual epochs and their associated uncertainties, respectively, at wavelength λ. This method estimates the degree of variability at each wavelength above what is expected given the measurement uncertainties and removes the effect of pixel-to-pixel noise from the rms spectrum. Note that the excess rms is only applicable to the total spectral flux and not to fluxes of individual components—such as AGN or stellar continuum—after spectral decomposition has been applied (see Section 3.3.1). This is because component-subtracted fluxes could be lower than the total flux uncertainties, which would result in negative values under the radical in Equation A.2.

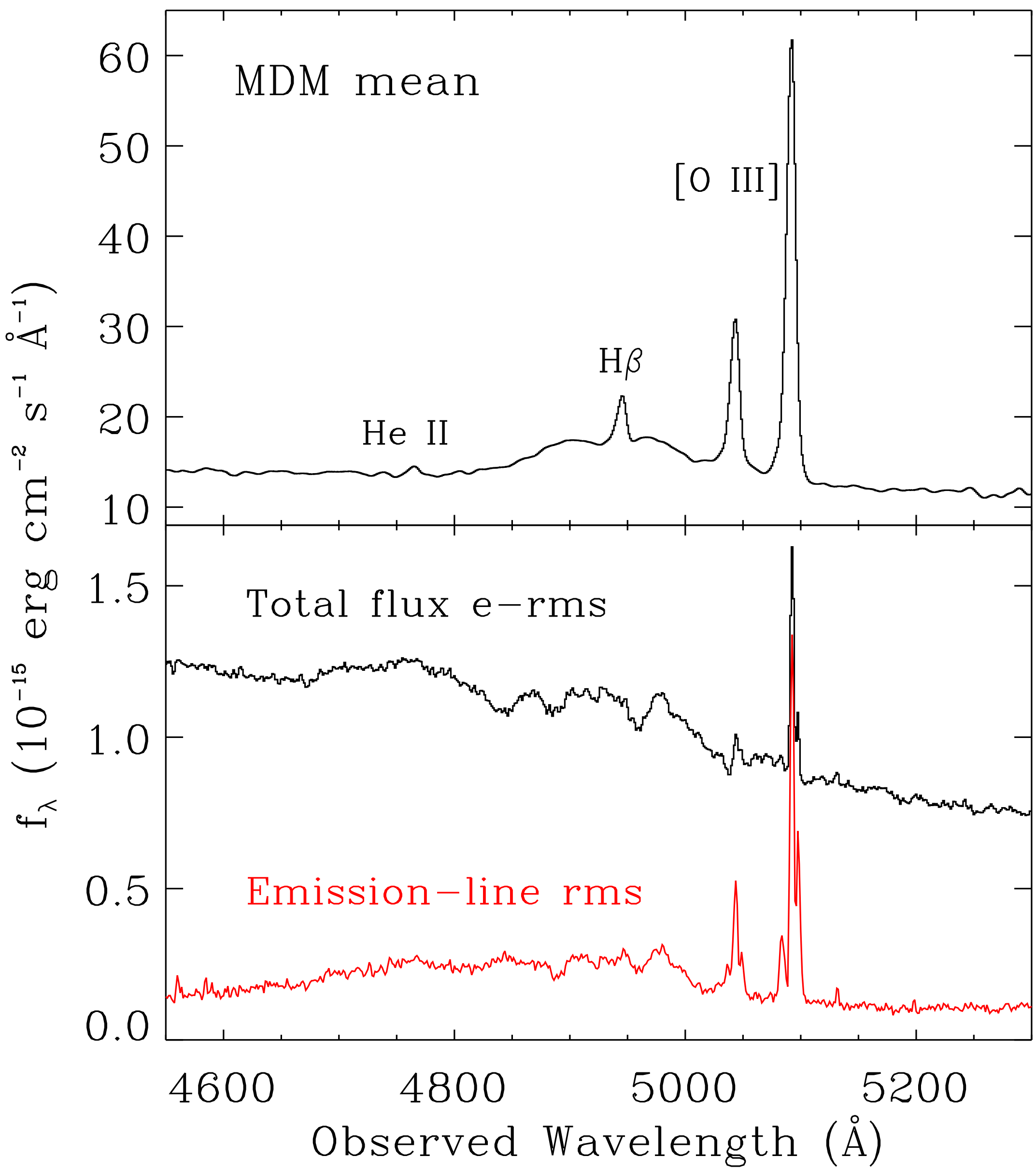

Figure 3.2: The mean and e-rms spectra from the MDM dataset are shown in black, and the rms spectrum with the AGN and stellar continuum removed is shown in red (see Section 3.3.1).

3.3 Spectroscopic Flux Measurements

The 5100 Å optical spectroscopic continuum flux was determined by averaging the flux over the observed wavelength range 5157.6−5217.6 Å, corresponding to rest-frame wavelengths of 5070−5130 Å. The Hβ line fluxes were measured from the scaled spectra using the same method as for [O III] λ5007, where we subtracted a linear fit to the surrounding continuum and integrated across the line profile. We used the wavelength ranges 4560−4620 Å and 5120−5180 Å to fit the linear continuum, and integrated over the range 4830−5030 Å for the Hβ line flux.

The flux uncertainty for each measurement is a combination of Poisson noise and residuals from spectral scaling. We computed the uncertainty due to imperfect spectral scaling by multiplying each flux measurement by the [O III] $F_{\rm var}$ value for that dataset, then adding this value in quadrature to the photon-counting error to obtain the final flux uncertainty for each measurement. There is an additional source of spectral scaling uncertainty—not represented by these quoted uncertainties—from differences in the overall spectral shape from night to night. Since the [O III] λ5007 line is used as reference in spectral scaling, parts of the spectra further from this line can have less accurate spectral calibrations if the spectral shape is significantly different from that of the reference spectrum. However, this effect is likely very small for Hβ, which is very close to [O III] λ5007.

Spectrophotometric calibrations of the reference spectra, as described in the previous section, converted all instrumental fluxes to absolute fluxes, which means that measurements from different telescopes should now be on the same flux scale. However, light curves of the same object measured over the same period but at different observing sites may be offset from each other by a flux scale factor and an additive shift due to aperture effects, where different aperture geometries result in different amounts of light loss for the point-like AGN and extended host galaxy and narrow-line region (Peterson et al., 1995, 1999). While our observations were standardized to have the same $5'' \times 15''$aperture size, significant differences in image quality between observing sites could still cause flux offsets.

We inter-calibrated the Hβ light curves from different telescopes by using data points that are nearly contemporaneous with MDM observations and performing a least-squares fit to the equation

$$F(\mathrm{H}\beta)_{\mathrm{true}} = \phi F(\mathrm{H}\beta)_{\mathrm{observed}} \tag{3.3}$$

to find the scale factor ϕ that puts each light curve on the same flux scale as the MDM data. Because the continuum flux has contributions from both the AGN point source and the extended host galaxy, we included an additive shift in the least-squares fit, i.e.

$$F(5100\ \text{Å})_{\mathrm{true}} = \phi F(5100\ \text{Å})_{\mathrm{observed}} + G. \tag{3.4}$$

The scale factors for Lick, Asiago, APO, and WIRO light curves are $\phi = [0.977,\ 0.998,\ 1.013,\ 1.084]$, and the shift constants are $G =$[0.092, -0.700, -0.050, -0.080]. The combined continuum and Hβ light curves are shown in Figure 3.3, and the 5100 $\mathring{A}$ continuum and Hβ fluxes are listed in Table 3.2.

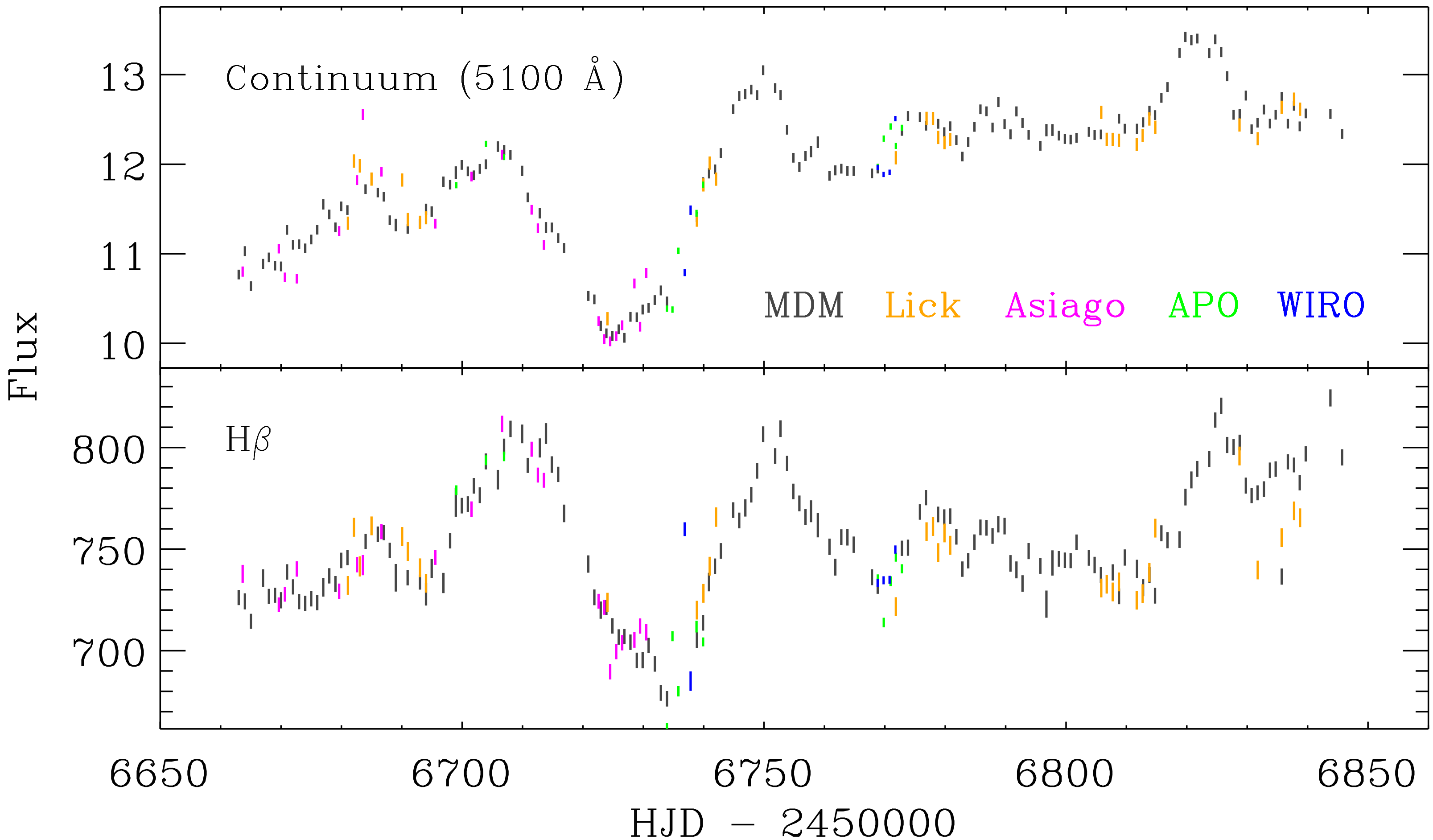

Figure 3.3: Continuum (10^{-15} erg s^{-1} cm^{-2} Å^{-1}) and Hβ (10^{-15} erg s^{-1} cm^{-2}) light curves. The Lick, APO, Asiago, and WIRO light curves were scaled and shifted to match the MDM light curve, which has the longest temporal coverage and highest sampling cadence.

Table 3.2. Flux measurements for continuum and emission lines.

HJD−2450000	Telescope	f_{5100}[a]	$f_{\mathrm{H}\beta}$[b]	$f_{\mathrm{H}\beta,\ \mathrm{SD}}$[c]	$f_{\mathrm{He\ II,\ SD}}$[d]
6663.00	MDM	10.768 ± 0.054	726.164 ± 3.759	732.158 ± 3.734	22.116 ± 2.666
6663.65	Asiago	10.800 ± 0.057	737.867 ± 4.391	—	—
6664.03	MDM	11.029 ± 0.055	724.274 ± 3.970	729.721 ± 3.946	29.052 ± 3.269
6665.02	MDM	10.639 ± 0.054	714.493 ± 3.697	721.235 ± 3.671	25.510 ± 2.469
6667.02	MDM	10.887 ± 0.056	735.759 ± 4.288	734.996 ± 4.266	37.657 ± 4.080

[a]Continuum flux (10^{-15} erg s^{-1} cm^{-2} Å^{-1}) at 5100 Å rest wavelength; includes both AGN and host galaxy contributions.

[b]Hβ flux (10^{-15} erg s^{-1} cm^{-2}) measured after subtracting a straigt-line fit to the continuum.

[c]Flux in 10^{-15} erg s^{-1} cm^{-2} measured from integrating the Hβ residual obtained after subtracting from the data all spectral decomposition (SD) model components except the Hβ components

[d]He II flux (10^{-15} erg s^{-1} cm^{-2}) measured from spectral decomposition models.

Note. — All emission-line fluxes include contribution from both broad and narrow line components. (See Appendix B for full table.)

We attempted to measure the He II λ4686 flux from the nightly spectra. However, this line is very weak and also heavily blended with broad Hβ, as shown in Figure 3.2, so we were unable to obtain a He II light curve using the linear interpolation method to remove the continuum.

3.3.1 Spectral Decomposition

To more accurately remove the continuum underlying the emission lines and to de-blend the broad emission features from each other, we employed the spectral decomposition algorithm described by Barth et al. (2015). The components fitted in this procedure include narrow [O III], broad and narrow Hβ, broad and narrow He II, Fe II emission blends, stellar continuum, and the AGN continuum. The host galaxy starlight was modeled with an 11 Gyr, solar metallicity, single-burst spectrum from Bruzual & Charlot (2003). For the Fe II component, we tested three different templates from Boroson & Green (1992), Véron-Cetty et al. (2004), and Kovačević et al. (2010). As part of the fitting procedure, the Fe II templates were broadened by convolution with a Gaussian kernel in velocity. The free fit parameters for Fe II include the velocity shift relative to broad Hβ, the broadening kernel width, and the flux normalization of the broadened template spectrum. The Boroson & Green (1992) and Véron-Cetty et al. (2004) templates are monolithic and require only one flux normalization parameter, whereas the Kovačević et al. (2010) template has five components that can vary independently in flux. We found that using the Kovačević et al. (2010) template achieves the best fit to the nightly spectra.

We made several modifications to the spectral fitting procedures used by Barth et al. (2015). First, because of the complex line profiles, we used sixth-order Gauss-Hermite functions to fit the Hβ and [O III] lines instead of fourth-order. Second, there is significant degeneracy between the weak Fe II blend and the continuum flux in the nightly fits. Since the Fe II

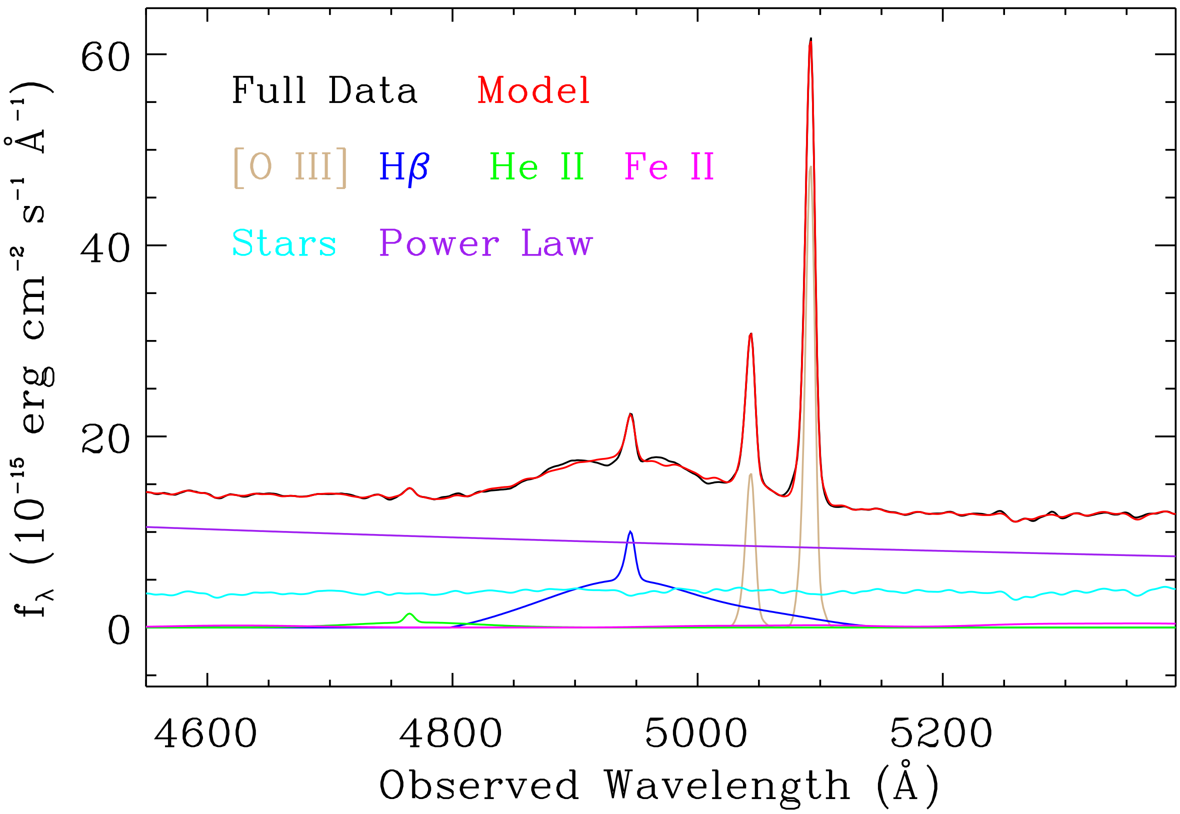

Figure 3.4: Spectral decomposition components of the mean MDM spectrum. The red spectrum is the sum of all model components.

fit is poorly constrained and sometimes varied drastically from night to night, the model continuum flux also varied significantly as a result, which in turn introduced noise to the Hβ fit component. To address this issue, we constrained the Fe II flux to lie within 10% of the value from the fit to the mean spectrum. We also fixed the Fe II redshift to that of the mean spectrum and constrained the Fe II broadening kernel to be within 5% of its value from the mean spectrum fit. The He I λ4922 and λ5016 lines are very weak and are heavily blended with broad Hβ, making it impossible to constrain their fit parameters. We therefore do not fit for these components in our model.

The broad He II λ4686 component has very low amplitude compared to other fit components and it is heavily blended with the blue wing of broad Hβ. It is also highly variable, as demonstrated by the broad bump in the rms spectrum. This made it difficult to fit the He II broad-line profile accurately, with the width varying significantly from night to night when allowed to vary freely. Since the He II λ1640 and λ4868 lines are expected to form under the same physical conditions and should thus have similar widths (), we used fits to the λ1640 line in concurrent spectra obtained with *HST* to constrain the λ4686 line width.

The He II λ1640 line was fitted with five Gaussian components (De Rosa et al., *in prep*), and we took the three broadest components to represent the broad He II λ1640 line profile. For each nightly MDM spectral fit, the He II λ4686 broad line full-width at half maximum (FWHM) was allowed to vary within 3 Å of the He II λ1640 FWHM measured from the *HST* epoch with the closest-matching time of observation. The first 23 epochs from the MDM campaign do not have corresponding *HST* spectra, so for each of these "initial epochs", we found the three epochs from later in the campaign with the closest matching 5100 Å continuum flux. We then used the weighted mean of the broad He II λ1640 widths from these three nights as the width constraint for the initial epoch, where the weights were determined by how closely the 5100 Å flux of the later epochs matched to that of the initial epoch. The width of the He II λ1640 line was highly variable during the *HST* campaign, and the set of model widths used to constrain all MDM epochs for spectral decomposition has a mean of 48 Å, with a minimum of 28 Å and maximum of 59 Å.

The final Hβ spectrum for each epoch—which we will refer to as the "Hβ-only" spectrum—was obtained by subtracting from the full spectrum all the fit components except the broad and narrow Hβ components. The Hβ line flux was then determined by integrating over the same wavelength range used previously when measuring the flux without spectral decomposition. The He II λ4686 flux for each night was taken to be the total flux in the broad and narrow He II λ4686 model fit component for that night. Both Hβ and He II flux measurements include narrow-line flux. The Hβ and He II λ4686 narrow-line fluxes from fits to the mean spectrum are 49.9×10^{-15} erg s^{-1} cm^{-2} and 8.8×10^{-15} erg s^{-1} cm^{-2} respectively, with approximately 2% uncertainty due to the overall photometric scale of the data. The ratio of the narrow Hβ flux to the [O III] λ5007 flux is $f_{\mathrm{H}\beta}/f_{[\mathrm{O\ III}]} = 0.100$, which is in good agreement with the value of $f_{\mathrm{H}\beta}/f_{[\mathrm{O\ III}]} = 0.110$ found by Peterson et al. (2004).

We applied spectral decomposition to the data from all telescopes. Figure 3.4 shows the fit components for the mean MDM spectrum. The red spectrum is the sum of all model fit components. The model does not fit the detailed structure of broad Hβ well, especially in the line core. However, this does not impact our measurements of the Hβ flux and the line profile because we do not use the broad Hβ model directly in our analysis. Instead, we use the spectrum obtained by subtracting all the other fit components from the full spectrum.

The red spectrum in Figure 3.2 shows the rms of the MDM dataset constructed after subtracting the AGN continuum and stellar continuum models from each nightly spectrum so that only emission-line components remain. The Hβ and He II λ4686 rms profiles are slightly different from those obtained without removing the continuum, plotted in black. Barth et al. (2015) discuss a potential bias that can affect line profile widths in the total flux rms spectrum and why it is advantageous to remove the continuum from nightly spectra before measuring the rms. The rms spectrum obtained after removing the AGN and stellar continua is expected to be a more accurate representation of the emission-line variability.

Figure 3.5(a) and Figure 3.5(c) show in black the mean and rms spectra for Hβ after spectral decomposition. The [O III] residuals are much lower than those found in the rms spectrum before performing spectral decomposition, but the Hβ profile still has a jagged shape in the rms spectrum after spectral decomposition.

Figure 3.6 shows the UV continuum light curve measured at 1158 Å from DR15, the MDM 5100 Å continuum light curve, the V-band photometric light curve measured by F16, and the MDM Hβ and He II λ4686 emission-line light curves. We define the truncated HJD as THJD = HJD − 2450000. Both the Hβ and He II fluxes include contributions from narrow-line components. The He II light curve reaches a flat-bottomed minimum at around THJD 6720. This is because the He II flux includes contributions from the variable broad-line component and the constant narrow-line component, so when the broad-line flux is zero, the total He II line flux stays at a constant value equal to the narrow-line flux. Light curve statistics that quantify the variability of NGC 5548 during the monitoring period are given in the top portion of Table 3.3. $F_{\rm var}$ is as defined in Equation 3.1 and $R_{\rm max}$ is the ratio between maximum and minimum observed fluxes in each light curve.

3.3.2 Host-Galaxy Flux Removal

We measured the host-galaxy contribution to the continuum flux using an "AGN-free" image of NGC 5548 generated by Bentz et al. (2013) after performing two-dimensional surface brightness decomposition on *HST* images of the galaxy. The amount of starlight that would be measured through our aperture geometry of $5'' \times 15''$ and at PA = 0 is $f_{\rm 5100,gal} = (4.52 \pm 0.45) \times 10^{-15}$ erg s^{-1} cm^{-2}. Subtracting this value from the mean continuum flux of $f_{5100} = (11.89 \pm 0.22) \times 10^{-15}$ erg s^{-1} cm^{-2}, we obtain $f_{\rm 5100,\,AGN} = (7.37 \pm 0.50) \times 10^{-15}$ erg s^{-1} cm^{-2} for the AGN optical continuum flux. Alternatively, from

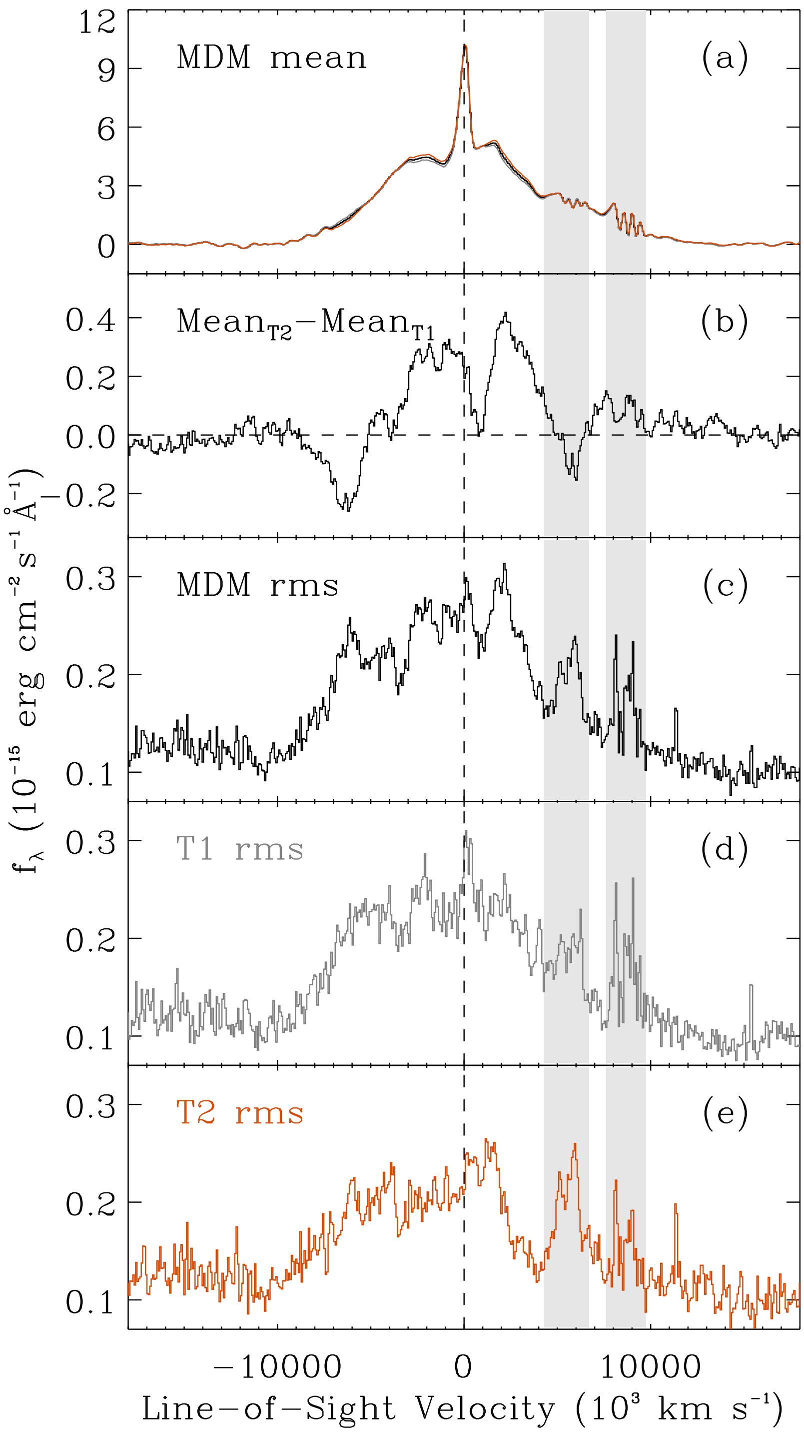

Figure 3.5: MDM mean and rms spectra for the Hβ-only component after spectral decomposition. The colors are for the full campaign (black), T1 (gray), and T2 (orange, see Section 3.3.3). Zero velocity is determined by the peak of the narrow Hβ line in the mean spectrum. The shaded regions indicate the [O III] residuals.

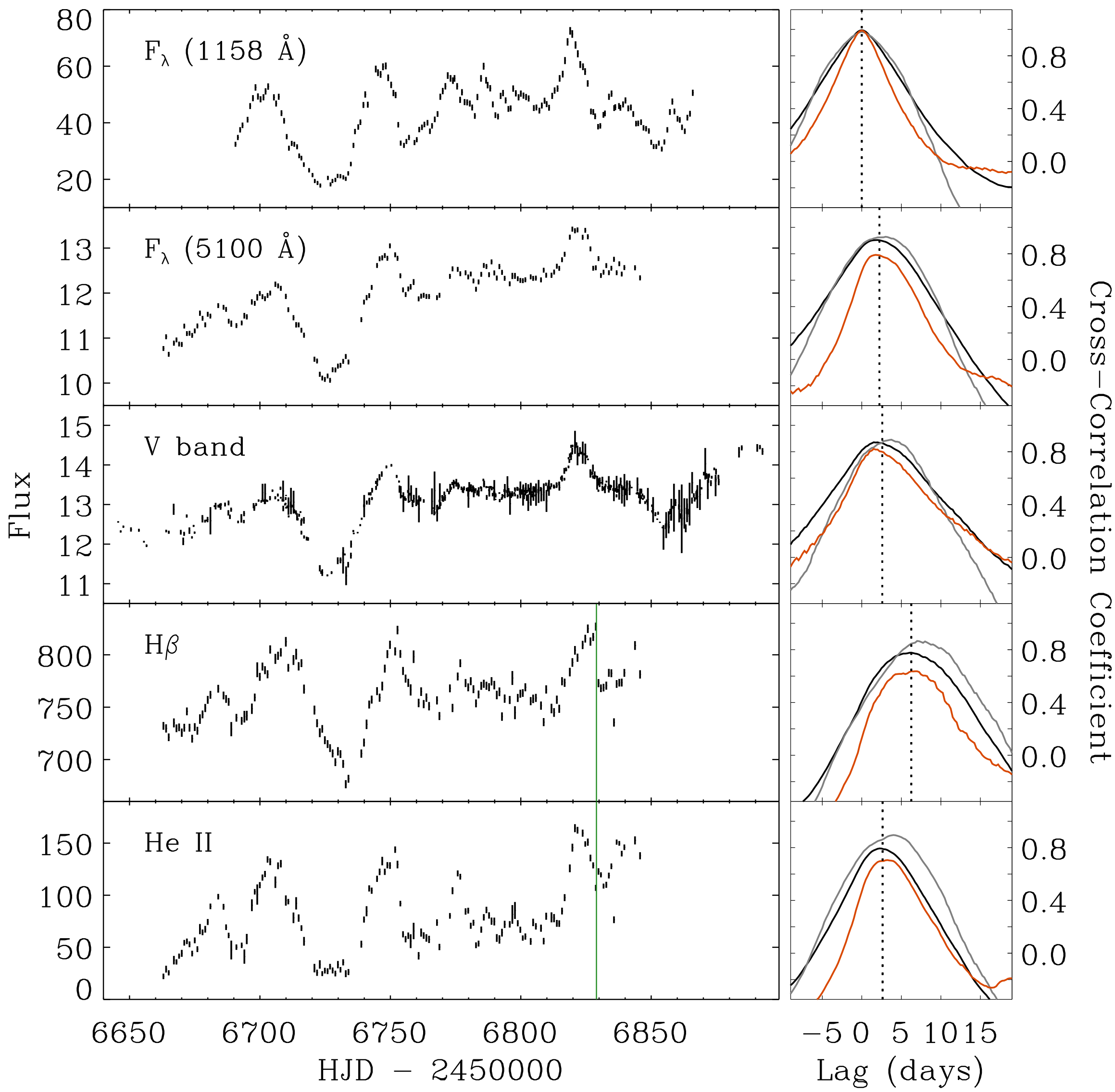

Figure 3.6: *Left:* Light curves for the UV 1158 Å continuum, optical 5100 Å continuum, V-band continuum, Hβ, and He II λ4686. Continuum light curves are in units of 10^{-15} erg s^{-1} cm^{-2} Å^{-1} and line light curves are in units of 10^{-15} erg s^{-1} cm^{-2}. The emission-line light curves are for individual spectral components after performing spectral decomposition (see text). The green vertical line indicates where the emission-line light curves were truncated in performing the lag analysis. *Right:* Cross-correlation functions for each light curve measured against the 1158 Å continuum. The black, gray, and orange solid lines represent the full campaign, T1, and T2, respectively. The dotted vertical lines denote $\tau_{\rm cen}$ for the full campaign. The top right panel shows the auto-correlation of the 1158 Å light curve.

Table 3.3. Light Curve Statistics

Emission Component	Mean Flux	$F_{\rm var}$	$R_{\rm max}$
F_λ (1158 Å)	43.48 ± 13.45	0.255	4.07 ± 0.18
F_λ (5100 Å)	11.89 ± 0.22	0.066	1.33 ± 0.01
Hβ	760.40 ± 28.38	0.040	1.22 ± 0.01
He II λ4686	77.19 ± 43.11	0.447	7.43 ± 0.90
F_λ (1158 Å, T1)	35.85 ± 6.73	0.351	3.31 ± 0.15
F_λ (1158 Å, T2)	46.72 ± 11.65	0.184	2.63 ± 0.08
F_λ (5100 Å, T1)	11.30 ± 0.45	0.059	1.27 ± 0.01
F_λ (5100 Å, T2)	12.50 ± 0.49	0.029	1.13 ± 0.01
Hβ (T1)	747.10 ± 34.01	0.042	1.20 ± 0.01
Hβ (T2)	773.70 ± 33.76	0.029	1.12 ± 0.01
He II λ4686 (T1)	67.38 ± 30.86	0.510	6.08 ± 0.75
He II λ4686 (T2)	87.00 ± 30.38	0.367	3.93 ± 0.35

Note. — Continuum fluxes are in units of 10^{-15} erg s^{-1} cm^{-2} Å^{-1} and emission-line fluxes are in units of 10^{-15} erg s^{-1} cm^{-2}. T1 and T2 denote the first and second halves of the campaign, respectively, divided at THJD = 6747.

spectral decomposition of the mean MDM spectrum, we obtain $f_{5100,\ \mathrm{AGN}} = (7.32 \pm 0.14) \times 10^{-15}$ erg s^{-1} cm^{-2}, which is entirely consistent with the result from using photometric analysis of *HST* images.

3.3.3 Anomalous Emission-Line Light Curve Behavior

RM analyses typically assume that the emission-line light curve is a lagged, scaled, and smoothed version of the continuum light curve. However, this does not appear to be the case for a portion of our campaign. DR15 and G16 described significant differences between the UV emission-line and continuum light curves starting at around THJD 6780. The continuum flux increased while the emission-line fluxes either decreased or remained roughly constant in a suppressed state for the remainder of the campaign.

We observed the optical emission lines to behave similarly to their UV counterparts. Figure 3.7 compares the 1158 Å light curve to the Hβ light curve after it has been shifted by 8 days and scaled and shifted in flux to match the main continuum variation features between THJD 6600 and THJD 6740. The two light curves have the same shape for most of the first half of the campaign, but begin to decorrelate near THJD 6740. The UV continuum flux continues to rise until about THJD 6755, while the Hβ flux begins to fall at THJD 6740. For the remainder of the campaign, the Hβ light curve does not clearly follow the variations in the continuum light curve and also has a relatively lower mean flux. The He II λ4686 light curve also deviates from the UV continuum light curve shape at around THJD 6760 and remains in a state of depressed flux until the very end of the monitoring period.

Due to this apparent change in the emission-line response, we followed the procedures presented by DR15 for determining the C IV and Lyα lags. We divided the optical continuum and emission-line light curves into two subsets to examine the lags of each subset separately. The first subset (T1) extends from THJD 6663.0 to THJD 6746.9 and includes 67 epochs.

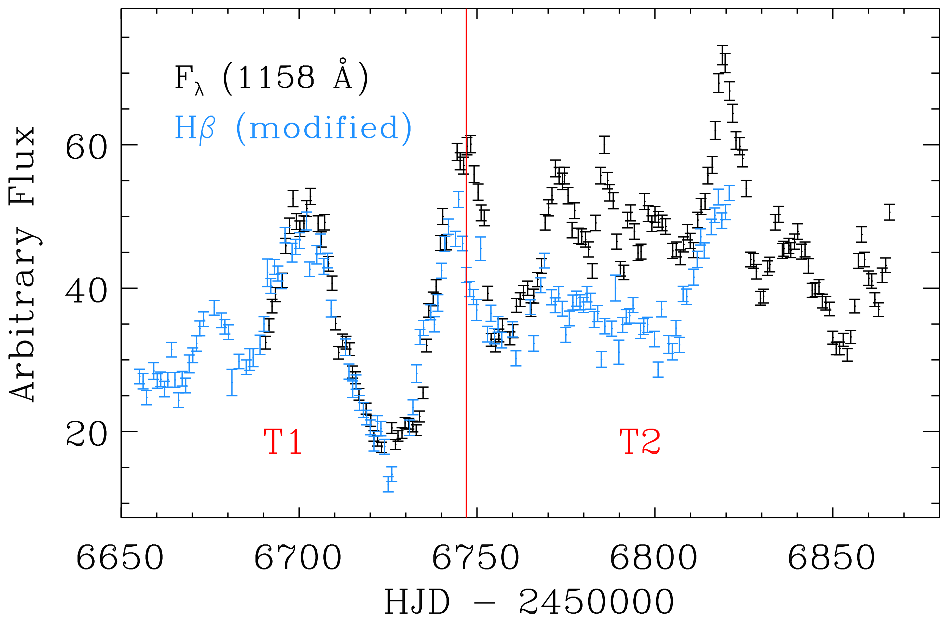

Figure 3.7: 1158 Å continuum light curve compared to an Hβ light curve that has been shifted by 8 days and scaled and shifted in flux for visual comparison. The vertical line at THJD 6747 indicates where the light curves are separated into the T1 and T2 segments.

The second subset (T2) extends from THJD 6747.9 to THJD 6828.8 and also includes 67 epochs. The 1158 Å, 5100 Å, and V-band continuum light curves were separated into two segments at THJD 6747. The mean flux, $F_{\rm var}$, and $R_{\rm max}$ values for the half light curves are given in the bottom portion of Table 3.3. Figure 3.5 shows the MDM mean and rms spectra for T1 and T2 subsets. While the three mean spectra look almost identical, the T1 and T2 rms spectra are significantly different.

3.4 Data Analysis

3.4.1 Emission-Line Lag Analysis

Cross-Correlation

We determined the emission-line responses to continuum variations by measuring the Hβ and He II λ4686 lags relative to both the 5100 Å continuum ("optical lags") and the 1158 Å continuum ("UV lags"). All light curves were detrended by subtracting a linear least-squares fit to the data to remove long-term trends that may bias lag calculations (Welsh, 1999). In this case, we found very weak trends for all light curves. We computed the cross-correlation coefficient r for lags between -20 and 30 days in increments of 0.25 days using the interpolation cross-correlation (ICCF) technique developed by White & Peterson (1994). Two lags were then determined for each light curve pair—the value corresponding to $r_{\max}$ (τ_{peak}) and the centroid of all values with $r > 0.8r_{\max}$ (τ_{cen}). Light curve detrending has a very small effect on the lags, typically on the order of 0.01 days.

Estimates for the final τ_{peak} and τ_{cen} values and their uncertainties were obtained by employing the Monte Carlo bootstrapping method described by Peterson et al. (2004), where many realizations of the continuum and emission-line light curves were created by randomly choosing with replacement n data points from the observed light curves, where n is the total number of points in the data set. If a data point is picked m times, then the uncertainty on that point is decreased by $m^{1/2}$. Each selected value is then varied by a random Gaussian deviate scaled to the flux uncertainty at that point to make the final light curves for that realization. We constructed 10^3 realizations of each light curve and computed the cross-correlation function (CCF) for each pair of line and continuum light-curve realizations to create a distribution of τ_{peak} and τ_{cen} values. The median value from each distribution and the central 64% interval are then taken to be the final lag and its uncertainty.

Table 3.4. Observed-Frame Emission-Line Lags

Light Curves	$\tau_{\rm peak}$	$\tau_{\rm cen}$	$\tau_{\rm cen,T1}$	$\tau_{\rm cen,T2}$	$\tau_{\tt JAVELIN}$	$\tau_{\tt JAVELIN,T1}$	$\tau_{\tt JAVELIN,T2}$
Hβ vs. F_λ(1158 Å)	$6.20^{+0.70}_{-1.00}$	$6.31^{+0.41}_{-0.41}$	$7.91^{+0.40}_{-0.44}$	$6.00^{+0.75}_{-0.82}$	$6.57^{+0.38}_{-0.40}$	$7.15^{+0.50}_{-0.49}$	$7.52^{+0.73}_{-0.76}$
Hβ vs. F_λ(1367 Å)	$6.00^{+0.25}_{-0.75}$	$6.00^{+0.38}_{-0.38}$	$7.49^{+0.39}_{-0.45}$	$5.94^{+0.78}_{-0.83}$	$6.24^{+0.38}_{-0.40}$	$6.72^{+0.46}_{-0.43}$	$7.27^{+0.73}_{-0.75}$
Hβ vs. F_λ(5100 Å)	$3.75^{+0.75}_{-0.25}$	$4.21^{+0.40}_{-0.35}$	$5.12^{+0.38}_{-0.46}$	$3.13^{+0.73}_{-0.64}$	$3.79^{+0.45}_{-0.45}$	$5.26^{+0.57}_{-0.56}$	$4.88^{+0.83}_{-0.90}$
Hβ vs. V band	$3.50^{+0.75}_{-0.25}$	$3.78^{+0.36}_{-0.29}$	$4.00^{+0.51}_{-0.48}$	$4.01^{+0.60}_{-0.61}$	$3.63^{+0.38}_{-0.38}$	$5.10^{+0.52}_{-0.55}$	$3.85^{+0.75}_{-0.64}$
He II vs. F_λ(1158 Å)	$2.25^{+0.50}_{-0.25}$	$2.63^{+0.33}_{-0.25}$	$3.64^{+0.38}_{-0.38}$	$3.15^{+0.35}_{-0.28}$	$2.64^{+0.27}_{-0.26}$	$3.24^{+0.34}_{-0.35}$	$2.97^{+0.24}_{-0.25}$
He II vs. F_λ(1367 Å)	$2.25^{+0.00}_{-0.25}$	$2.48^{+0.15}_{-0.25}$	$3.38^{+0.35}_{-0.37}$	$3.11^{+0.36}_{-0.26}$	$2.39^{+0.25}_{-0.25}$	$2.98^{+0.33}_{-0.34}$	$2.79^{+0.25}_{-0.25}$
He II vs. F_λ(5100 Å)	$0.50^{+0.25}_{-0.25}$	$0.49^{+0.26}_{-0.36}$	$1.11^{+0.37}_{-0.36}$	$0.85^{+0.27}_{-0.34}$	$0.34^{+0.24}_{-0.40}$	$0.99^{+0.42}_{-0.42}$	$0.86^{+0.27}_{-0.27}$
He II vs. V band	$0.50^{+0.25}_{-0.50}$	$0.49^{+0.25}_{-0.26}$	$0.28^{+0.44}_{-0.39}$	$1.47^{+0.36}_{-0.34}$	$0.64^{+0.08}_{-0.09}$	$0.51^{+0.37}_{-0.37}$	$0.86^{+0.23}_{-0.21}$
F_λ(5100 Å) vs. F_λ(1158 Å)	$2.00^{+0.25}_{-0.25}$	$2.24^{+0.24}_{-0.24}$	$2.62^{+0.28}_{-0.33}$	$2.61^{+0.36}_{-0.36}$			
H$\beta_{\rm full,\ MDM}$ vs. F_λ(1158 Å)	$5.50^{+0.25}_{-0.25}$	$5.76^{+0.46}_{-0.39}$					
H$\beta_{\rm full,\ all\ sites}$ vs. F_λ(1158 Å)	$5.75^{+0.50}_{-0.50}$	$5.56^{+0.37}_{-0.36}$					

Note. — Hβ and He II λ4686 lags (days) for the full campaign and for T1 (THJD < 6747) and T2 (THJD > 6747) subsets, measured using both ICCF and `JAVELIN`. The last two lines show Hβ lags without spectral decomposition, calculated using spectra from MDM only and all telescopes, up to THJD 6828.75. Observed-frame lags can be converted to rest-frame lags by dividing by $1 + z$.

Table 3.4 lists the ICCF lags for Hβ and He II λ4686 measured against the 1158 Å, 5100 Å, and V-band continuum light curves. The lag between the 5100 Å and 1158 Å continua is also given. For comparison with DR15, who present the UV line lags against the 1367 Å continuum, we also include Hβ and He II lags measured against this light curve. Distributions of τ_{cen} values from the Monte Carlo bootstrap analysis using the 1158 Å continuum are shown in the top panels of Figure 3.8, Figure 3.9, and Figure 3.10.

We found the Hβ lag to be longer for T1 than for T2 when measured against all three spectroscopic continua, with the full-campaign lag always between the T1 and T2 values for each case. The He II λ4686 T1 lags are also longer than the T2 lags when measured against the three spectroscopic continua and the full-campaign lags are shorter than those of both T1 and T2. In comparison, DR15 found the Lyα, Si IV, C IV, and He II λ1640 lags to be longer for T2 than for T1, which is the opposite of what we find for Hβ.

To illustrate the effects of spectral decomposition, we also include in Table 3.4 ICCF lags for the Hβ light curve where fluxes were measured after subtracting a straight-line fit to the continuum without spectral decomposition. We calculated lags for both the MDM-only Hβ light curve and the light curve that includes data from Lick, Asiago, APO and WIRO. The Hβ light curves were truncated at THJD 6828.75 to exclude the last 13 epochs of MDM data (see Section 3.2). Hβ lags obtained with and without using spectral decomposition are consistent within 1σ.

`JAVELIN`

In addition to the ICCF method, we computed emission-lags using the `JAVELIN` suite of Python codes (Zu et al., 2011). We linearly detrended the light curves, then used `JAVELIN` to model the AGN continuum variability as a damped random walk process (DRW Kelly et al., 2009). The emission-line light curves are modeled as a smoothed, scaled, and lagged version

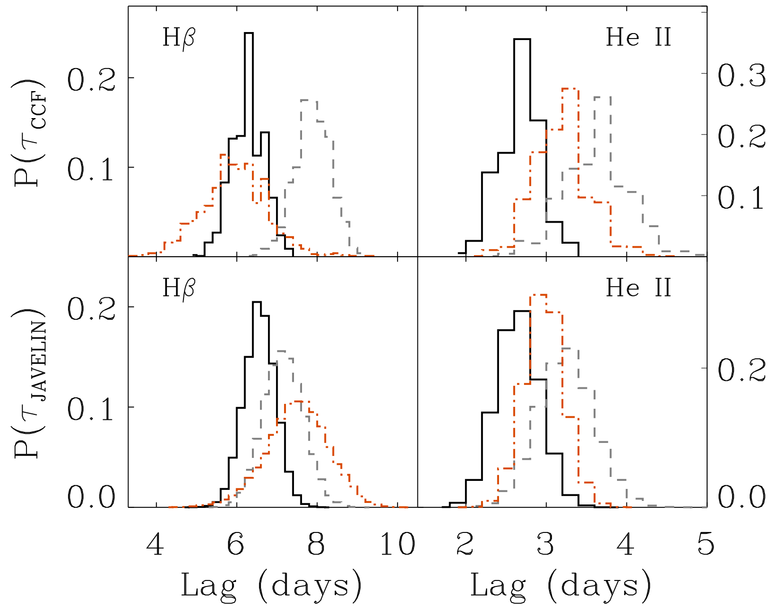

Figure 3.8: $\tau_{\rm cen}$ (*top*) and `JAVELIN` lag (*bottom*) probability distributions for Hβ (*left*) and He II (*right*) measured against the 1158 Å continuum. Black solid lines are for the full campaign, gray dashed lines are for T1, and orange dot-dash lines are for T2.

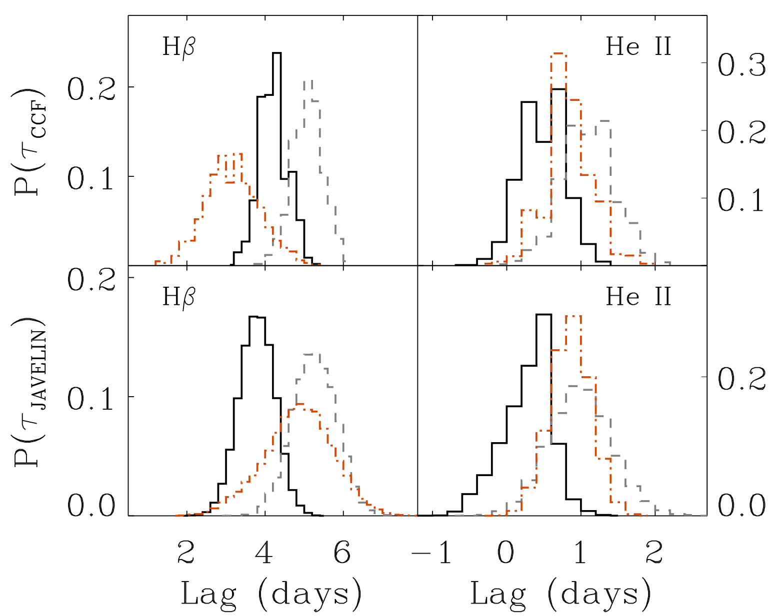

Figure 3.9: Same as Figure 3.8, but for lags measured against the rest-frame 5100 Å continuum.

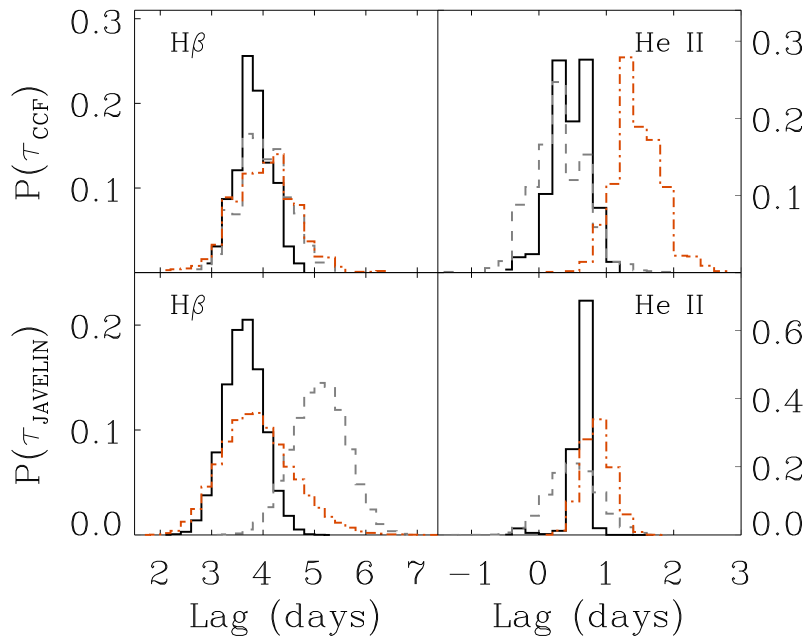

Figure 3.10: Same as Figure 3.8, but for lags measured against the photometric V-band light curve.

of the continuum light curve assuming a top-hat transfer function. We performed a two-line lag analysis using Hβ and He II λ4686, and lags were measured separately against the 1158 Å, 5100 Å, and V-band continua. Typically, the DRW parameters from fits to the continuum light curve are used to constrain the emission-line light curves from the same campaign. However, because longer light curves offer better constraints to the damping timescale, we used the Zu et al. (2011) value of $\tau_{\rm DRW} \sim 164$ days, derived from the 13-year light curve of NGC 5548 (Peterson et al., 2002), to constrain all our `JAVELIN` light curve fits.

Our initial `JAVELIN` light-curve models contained spurious high-frequency variations. This is likely because `JAVELIN` assumes that the line and continuum light curves have the same general shape, so when the line light curves deviate from that of the continuum in this campaign as previously described, `JAVELIN` creates light curve models with high-amplitude and high-frequency flux variations so that the models can match both the observed continuum light curve and the depressed line light curve (see top three panels of Figure 3.11). We mit-

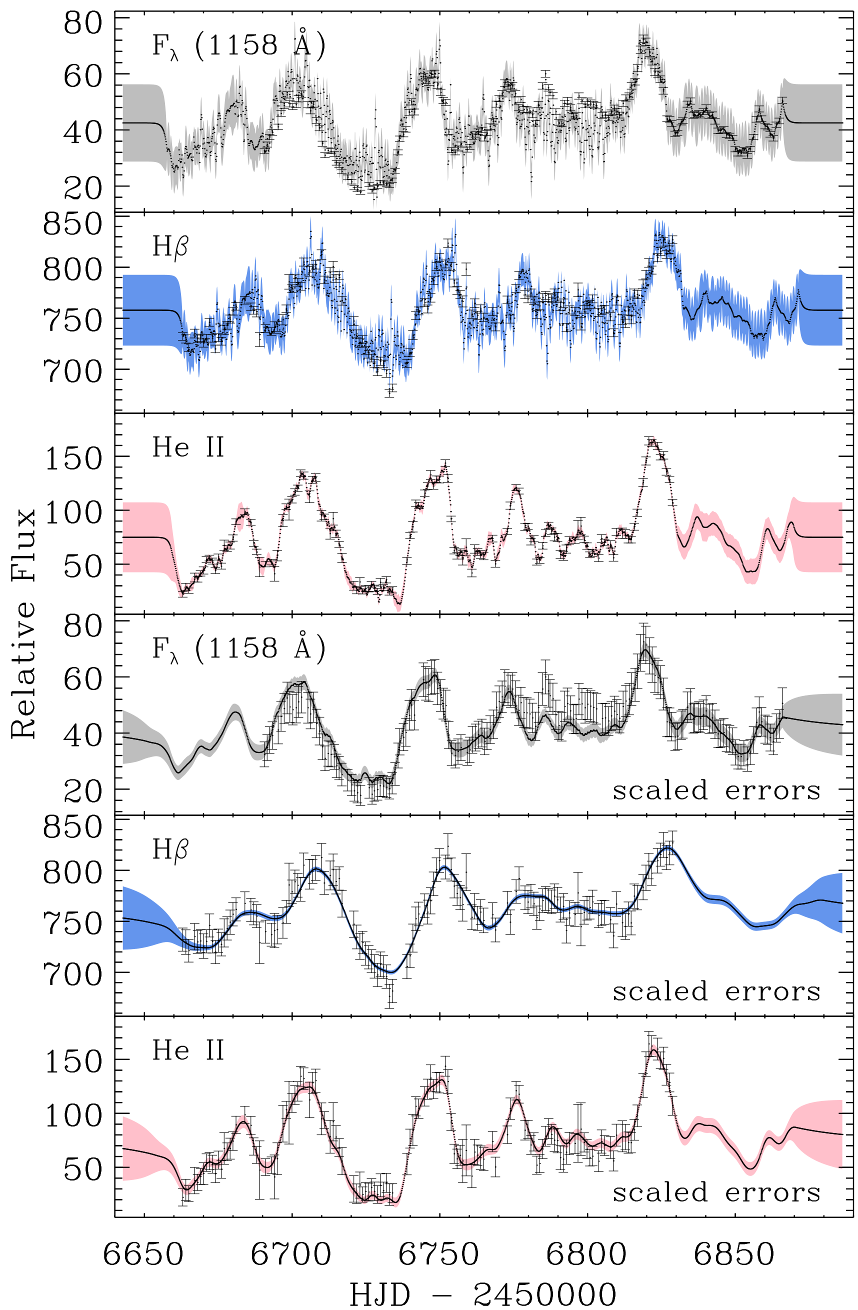

Figure 3.11: JAVELIN light curves from simultaneously modeling the Hβ and He II λ4686 emission lines with the UV 1158 Å continuum. The data points are measured from observations, the black solid lines are the weighted means of the model light curves consistent with the data, and the thickness of the shaded regions indicate the 1σ spread of those light curves. The top three panels show the observed data and JAVELIN model light curves without any error inflation, and the bottom three panels show the data and light-curve models with scaled uncertainties.

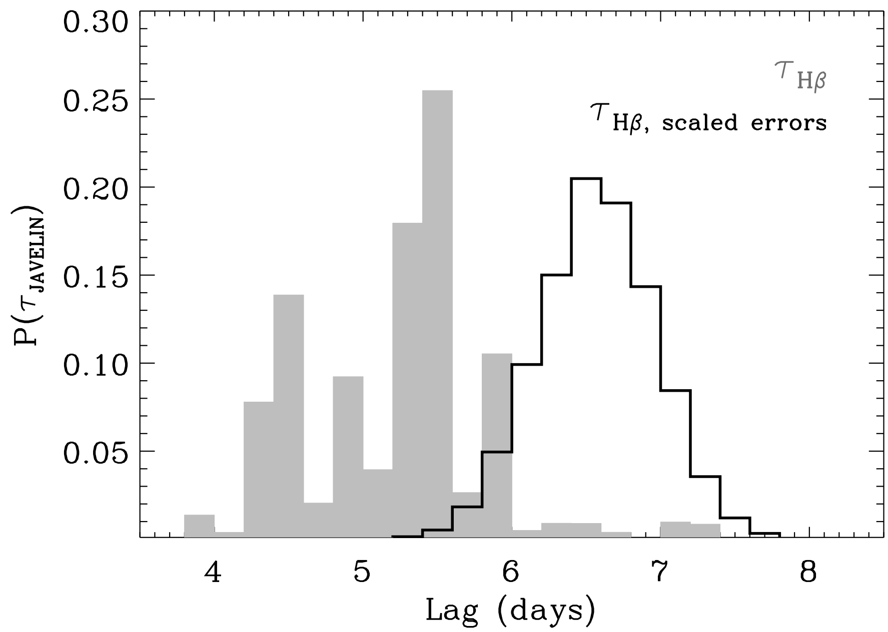

Figure 3.12: `JAVELIN` posterior lag distributions for Hβ and the 1158 Å continuum using light curves with unscaled flux uncertainties (gray filled histograms) and scaled flux uncertainties (black open histogram).

igated these problems by scaling up the flux uncertainties on all light curves until `JAVELIN` obtained converging lag solutions and produced smooth model light curves without overfitting the noise. This resulted in error inflation factors of 5.0 and 3.0 for the full-campaign continuum and line light curves, respectively, where the continuum inflation factor applies to all three continua. For the half-campaign light curves, we used an error inflation factor of 3.0 for both the continuum and emission lines. This is because the line light curves deviate from the continuum close to the epoch separating T1 and T2, so when we divided the light curves into halves, `JAVELIN` used different scale factors for T1 and T2 to scale the line light curves to the continuum light curve, and less error inflation was needed to account for the depressed emission-line fluxes.

Figures 3.12 show `JAVELIN` lag distributions for Hβ before and after scaling the light curve uncertainties, and the modeled UV continuum, Hβ, and He II light curves with scaled errors are shown in the bottom panels of Figure 3.11. Note that even though `JAVELIN` solutions do converge after expanding the light-curve errors, the code's fundamental assumption that the line light curve is always a smoothed, scaled, and lagged version of the continuum light curve is still violated for this dataset.

Velocity-Resolved Results

We examined the velocity-resolved emission-line response by dividing the Hβ line profile into 10 Å bins with each bin corresponding to a velocity width of 607 km s^{-1}, and constructing light curves for each velocity bin. Zero velocity is set by the peak of the narrow Hβ component in the mean spectrum. We then determined the lag of each of these light curves with respect to the UV and optical continua, which are shown in the top panel of Figure 3.13, where $v_r = 0$ is determined by the peak of the narrow Hβ line in the mean spectrum. The second panel shows the velocity-resolved Hβ–UV lag for the full campaign, T1, and T2. Since the line and continuum light curves do not follow each other well during T2, the cross-correlation function peaks were less well-defined and $\tau_{\rm peak}$ values had large uncertainties. Therefore, starting from the blue end of the line profile at 4830 Å, we increase the bin size in increments of 5 Å until the T2 upper and lower uncertainties on $\tau_{\rm cen}$ were less than three days. The blue horizontal error bars on each T2 point span the wavelength range over which the line flux was integrated. There were also five epochs of spectra that produced outlier Hβ fluxes and significantly higher-than-average flux uncertainties when the Hβ flux was measured from individual velocity bins, so we removed these epochs from the velocity-resolved light curves in order to improve cross-correlation results. The bottom two panels of Figure 3.13 show the MDM mean and rms spectra. The values plotted in the second panel are listed in Table 3.5.

The velocity-resolved Hβ–UV lag for the full campaign is shortest in the blue wing where the line-of-sight velocity ($v_{\rm r}$) is approximately -7000 km s^{-1} ($\tau_{\rm cen} \sim 2$ days) and also relatively low in the red wing at $v_{\rm r} \sim 5000$ km s^{-1} ($\tau_{\rm cen} \sim 6$ days). We did not calculate velocity-resolved lags for bins at higher v_r in the red wing because the Hβ flux in this region is

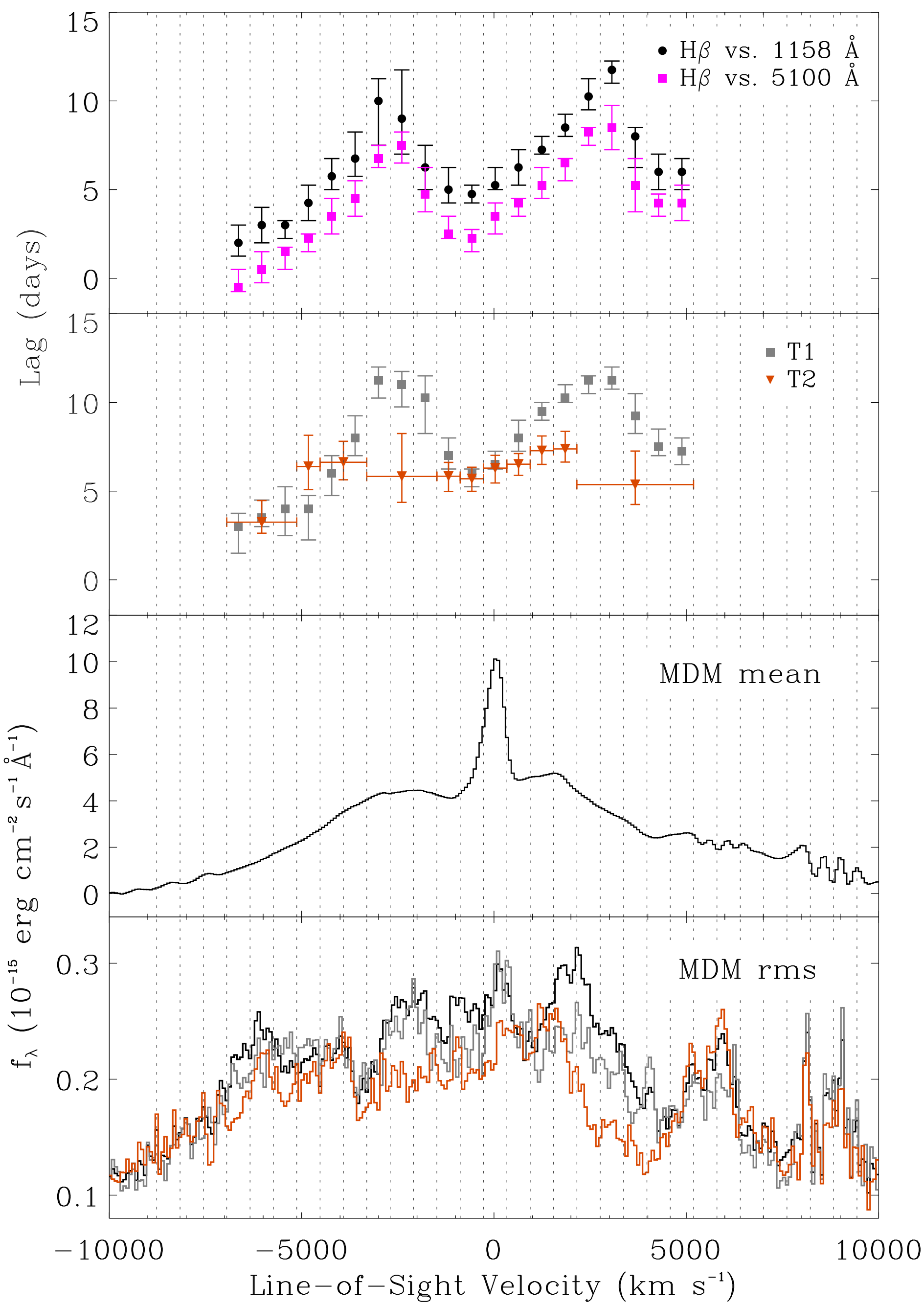

Figure 3.13: *Top:* Hβ velocity-resolved ICCF lags ($\tau_{\rm cen}$) measured against the 1158 Å and 5100 Å continua. *Top middle:* Velocity-resolved Hβ lags measured against the 1158 Å continuum for the T1 and T2 segments. *Bottom middle:* MDM mean spectrum for the full campaign. *Bottom:* MDM rms spectrum for the full, T1, and T2 segments in black, gray, and orange respectively. Zero velocity is determined by the peak of the narrow Hβ line in the mean spectrum.

contaminated by [O III] residuals. The lag increases as $v_{\rm r}$ approaches zero from both sides of the lag profile and reaches local maxima at about $v_{\rm r} \sim \pm 3000$ km s^{-1} ($\tau_{\rm cen} \sim 10$ days), then steadily decreases—more quickly on the blue side than the red side—until it reaches a local minimum at about -800 km s^{-1} ($\tau_{\rm cen} \sim 4$ days). The Hβ velocity-resolved lag profile measured against the optical continuum has a shape similar to that measured against the UV continuum, but with all lags $\sim 2 - 3$ days shorter. A double-peaked velocity-resolved lag profile is also observed for Lyα (see DR15).

The shape of the velocity-resolved lag profile can provide qualitative information about the kinematics of the line-emitting gas (e.g. Kollatschny, 2003; Bentz et al., 2009b; Denney et al., 2010; Barth et al., 2011a; Du et al., 2016a). In simple models of the BLR (Ulrich et al., 1984; Gaskell, 1988; Welsh & Horne, 1991; Horne et al., 2004; Goad et al., 2012; Gaskell & Goosmann, 2013; Grier et al., 2013), pure infall motion would lead to longer lags on the blue side of the line profile, and for outflow, the most redshifted gas would have the longest lag. For pure Keplerian motion, the shortest lags would be in the line wings, since gas with higher $v_{\rm r}$ is closer to the central black hole. Gas with very low $v_{\rm r}$ could have a wide range of lags, and a spherical or flat disk distribution of BLR clouds in Keplerian motion could lead to a double-peaked velocity-resolved lag profile if the ionizing source is emitting anisotropically (Welsh & Horne, 1991; Horne et al., 2004). Previous studies of the UV and optical lines in NGC 5548 have inferred either Keplerian orbits (Horne et al., 1991; Wanders et al., 1995; Denney et al., 2009; Bentz et al., 2010b) or infalling motion (Crenshaw & Blackwell, 1990; Done & Krolik, 1996; Welsh et al., 2007; Pancoast et al., 2014; Gaskell & Goosmann, 2016) for the BLR gas. From our data, the shape of the Hβ velocity-resolved lag profile suggests a BLR dominated by Keplerian motion. However, more detailed interpretation requires comparison with transfer functions generated for various dynamical models of the BLR, which is beyond the scope of this work.

Table 3.5: Velocity-resolved Hβ ICCF lags ($\tau_{\rm cen}$) for the full campaign and for T1 (THJD < 6747) and T2 (THJD > 6747) segments. Observed-frame lags can be converted to rest-frame lags by dividing by $1+z$.

Wavelength Range (Å)	$\tau_{\rm Full}$ (days)	$r_{\rm max,Full}$	$\tau_{\rm T1}$ (days)	$r_{\rm max,T1}$	Wavelength Range (Å)	$\tau_{\rm T2}$ (days)	$r_{\rm max,T2}$
4830−4840	$2.08^{+0.51}_{-0.48}$	0.66	$2.40^{+0.62}_{-0.66}$	0.84	4830−4860	$3.25^{+1.22}_{-0.62}$	0.54
4840−4850	$3.30^{+0.54}_{-0.57}$	0.67	$3.52^{+0.59}_{-0.63}$	0.88			
4850−4860	$3.12^{+0.40}_{-0.39}$	0.75	$3.47^{+0.53}_{-0.57}$	0.84			
4860−4870	$4.47^{+0.52}_{-0.58}$	0.70	$3.27^{+0.51}_{-0.48}$	0.85	4860−4870	$6.39^{+1.76}_{-1.30}$	0.52
4870−4880	$5.63^{+0.85}_{-0.65}$	0.64	$5.97^{+0.86}_{-0.97}$	0.81	4870−4890	$6.63^{+1.18}_{-0.99}$	0.53
4880−4890	$6.97^{+0.67}_{-0.70}$	0.65	$8.25^{+0.81}_{-0.71}$	0.80			
4890−4900	$9.21^{+0.81}_{-0.87}$	0.63	$11.01^{+0.90}_{-0.98}$	0.82	4890−4920	$5.83^{+2.42}_{-1.46}$	0.44
4900−4910	$9.35^{+1.28}_{-1.15}$	0.53	$10.92^{+1.31}_{-0.90}$	0.80			
4910−4920	$6.84^{+0.83}_{-0.87}$	0.61	$10.22^{+0.89}_{-0.94}$	0.78			
4920−4930	$5.47^{+0.47}_{-0.50}$	0.71	$7.24^{+0.64}_{-0.63}$	0.86	4920−4930	$5.84^{+0.78}_{-0.86}$	0.69
4930−4940	$4.89^{+0.49}_{-0.41}$	0.73	$5.73^{+0.55}_{-0.71}$	0.91	4930−4940	$5.70^{+0.65}_{-0.71}$	0.74
4940−4950	$5.86^{+0.51}_{-0.50}$	0.75	$7.10^{+0.51}_{-0.59}$	0.89	4940−4950	$6.30^{+0.72}_{-0.84}$	0.73
4950−4960	$6.50^{+0.48}_{-0.46}$	0.75	$8.47^{+0.54}_{-0.60}$	0.87	4950−4960	$6.52^{+0.60}_{-0.63}$	0.67
4960−4970	$7.38^{+0.46}_{-0.49}$	0.77	$9.61^{+0.47}_{-0.39}$	0.93	4960−4970	$7.28^{+0.83}_{-0.77}$	0.71
4970−4980	$8.38^{+0.39}_{-0.40}$	0.82	$10.48^{+0.48}_{-0.48}$	0.91	4970−4980	$7.38^{+0.99}_{-0.74}$	0.69

Continued on next page

Table 3.5 – continued from previous page

Wavelength Range (Å)	τ_{Full} (days)	$r_{\mathrm{max,Full}}$	τ_{T1} (days)	$r_{\mathrm{max,T1}}$	Wavelength Range (Å)	τ_{T2} (days)	$r_{\mathrm{max,T2}}$
4980−4990	$10.12^{+0.61}_{-0.51}$	0.78	$11.33^{+0.54}_{-0.60}$	0.89	4980−5030	$5.37^{+1.89}_{-1.12}$	0.45
4990−5000	$10.86^{+0.85}_{-1.05}$	0.70	$11.55^{+0.57}_{-0.64}$	0.87			
5000−5010	$7.53^{+0.99}_{-1.03}$	0.65	$9.85^{+0.73}_{-0.75}$	0.85			
5010−5020	$6.23^{+0.64}_{-0.62}$	0.65	$8.24^{+0.72}_{-0.73}$	0.88			
5020−5030	$5.76^{+0.73}_{-0.62}$	0.48	$7.28^{+0.60}_{-0.54}$	0.88			

Figure 3.14 shows light curves for 20 Å velocity bins across the broad Hβ line profile. The velocity-binned light curves all have slightly different shapes, primarily in the T2 period, indicating that gas clouds with different radial velocity ranges are responding to the continuum in different ways during the second half of the campaign.

3.4.2 Anomalous Emission-Line Response to Continuum

One basic assumption in RM is that the emission-line light curves are smoothed, scaled, and lagged versions of the continuum light curve and that these light curves have the same overall shape. However, this assumption was not valid for the entirety of the AGN STORM campaign, as we observed all the UV and optical emission-line light curves decorrelating from the UV continuum about halfway through the monitoring period.

G16 examined this effect for the UV lines by measuring changes in the line equivalent width (EW), defined as

$$\mathrm{EW} = \frac{F_{\mathrm{line}}}{F_{\mathrm{cont}}}, \tag{3.5}$$

and the responsivity (η_{eff}), which is the power-law index that relates changes in continuum flux to changes in emission-line fluxes, i.e.

$$\mathrm{d}F_{\mathrm{line}} \propto (\mathrm{d}F_{\mathrm{cont}})^{\eta_{\mathrm{eff}}}. \tag{3.6}$$

F_{cont} and F_{line} refer to the *ionizing* continuum and emission-line fluxes after removing

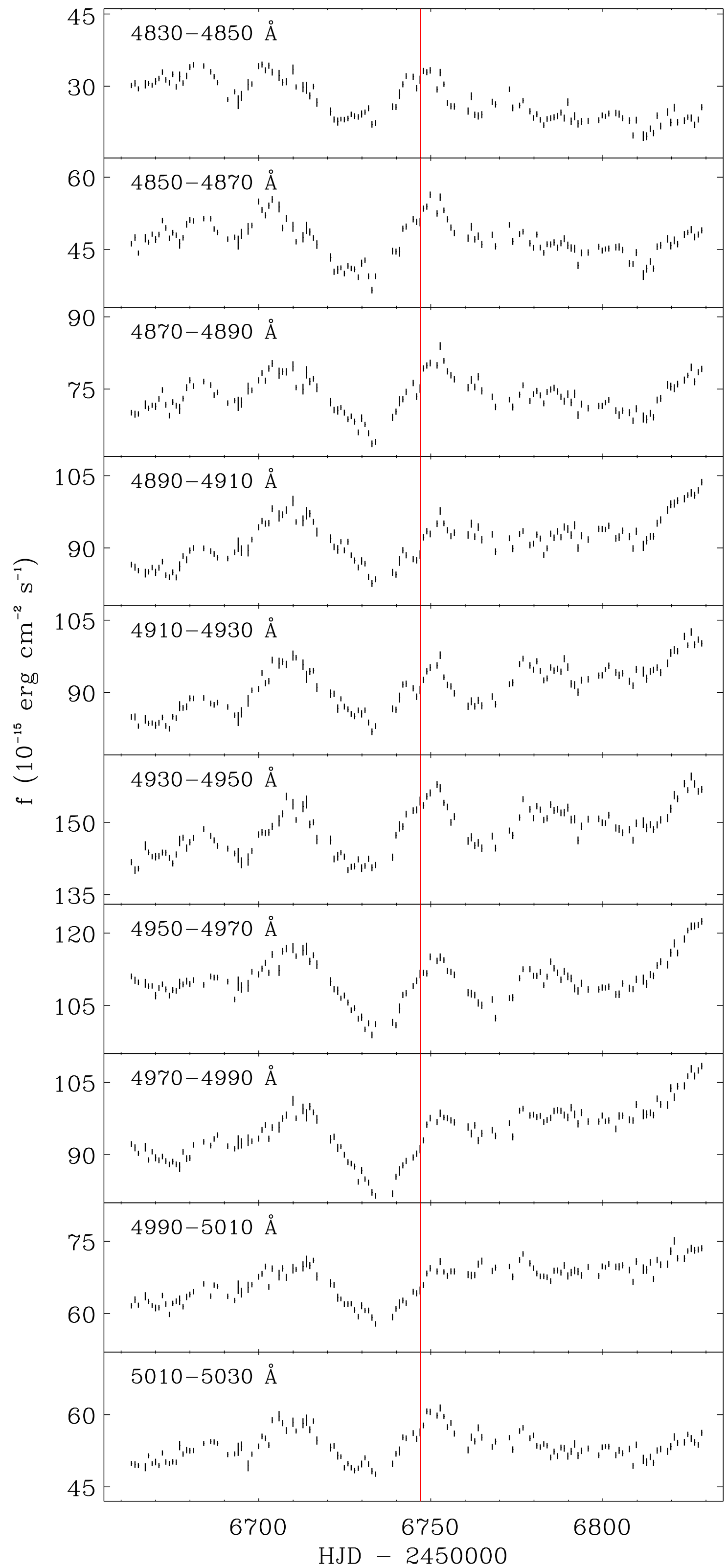

Figure 3.14: Hβ light curves for 20 Å bins over the wavelength range 4830−5030 Å. The red line indicates the epoch that separates the T1 and T2 segments.

non-variable components such as host galaxy and narrow-line flux contributions, and after correcting for the mean emission-line delay between the continuum and line light curves (Pogge & Peterson, 1992; Gilbert & Peterson, 2003; Goad et al., 2004). There is an underlying assumption here that the choice in $F_{\rm cont}$ gives a reasonably good proxy for the variability of the ionizing continuum. Both $\eta_{\rm eff}$ and EW are quantities that measure how much an emission line varies for a given continuum variation about some average value, and EW scales with the continuum flux as

$$\mathrm{dEW}_{\rm line} \propto (\mathrm{d}F_{\rm cont})^{\beta}, \tag{3.7}$$

where $\beta = \eta_{\rm eff} - 1$.

Following the same procedures as those performed by G16, we first compute the responsivity and EW for the portion of the Hβ light curve that correlates with the UV continuum, and then examine how these values differ for portions of the Hβ light curve that deviate from the UV continuum. There is very little contribution from the host galaxy in the continuum flux because the continuum at 1158 Å is dominated by the variable AGN. To remove the non-variable component of the emission-line flux, we took Hβ fluxes measured using simple linear continuum removal (without spectral decomposition) and subtracted a constant narrow Hβ flux measured from the MDM mean spectrum fit. We also shifted the Hβ light curve by 7.01 days, which is the lag of the portion of the line light curve closely correlated with the UV continuum light curve, to remove the emission-line delay in our calculation of $\eta_{\rm eff}$ and β.

Figure 3.15(c) shows the 1158 Å continuum light curve (black) with the time-shifted Hβ light curve, which has also been scaled and shifted in flux for better visual comparison. The beginning of each Hβ light curve is truncated to match the first epoch of continuum observations. To show the line light curve's general behavior toward the end of the campaign, we have shown here the full 147 epochs of Hβ flux measurements instead of the 134-epoch light curve we used in the Hβ lag analysis. However, since the last 13 epochs of spectra suffer from inconsistent spectral flux calibrations (see Section 3.2), we do not use these points in calculating η_{eff} or β.

We divided each Hβ light curve into five segments. The first segment corresponds to the period when the line light curve closely follows the continuum light curve (blue points); the second and third segments correspond to when the line light curve decouples from the continuum (cyan points) and remains in a state of depressed flux (red points); the last two segments correspond to the line light curve recovering from the depressed stated (magenta points) and correlating once again with the continuum light curve (green points). The epochs that divide these segments are THJD = 6745, 6774, 6810, and 6828. We will refer to using this set of dividing epochs as Method 1.

Figure 3.15(a) and 3.15(b) show the Hβ broad-line flux and EW as a function of the 1158 Å continuum flux determined from the *HST* epoch closest to each MDM epoch. The red lines represent least-squares fits to the equations

$$\mathrm{d}(\log\ F_{\text{line}}) = A + \eta_{\text{eff}}[\mathrm{d}(\log\ F_{\text{cont}})] \tag{3.8}$$

and

$$\mathrm{d}(\log\ \mathrm{EW}_{\text{line}}) = B + \beta[\mathrm{d}(\log\ F_{\text{cont}})] \tag{3.9}$$

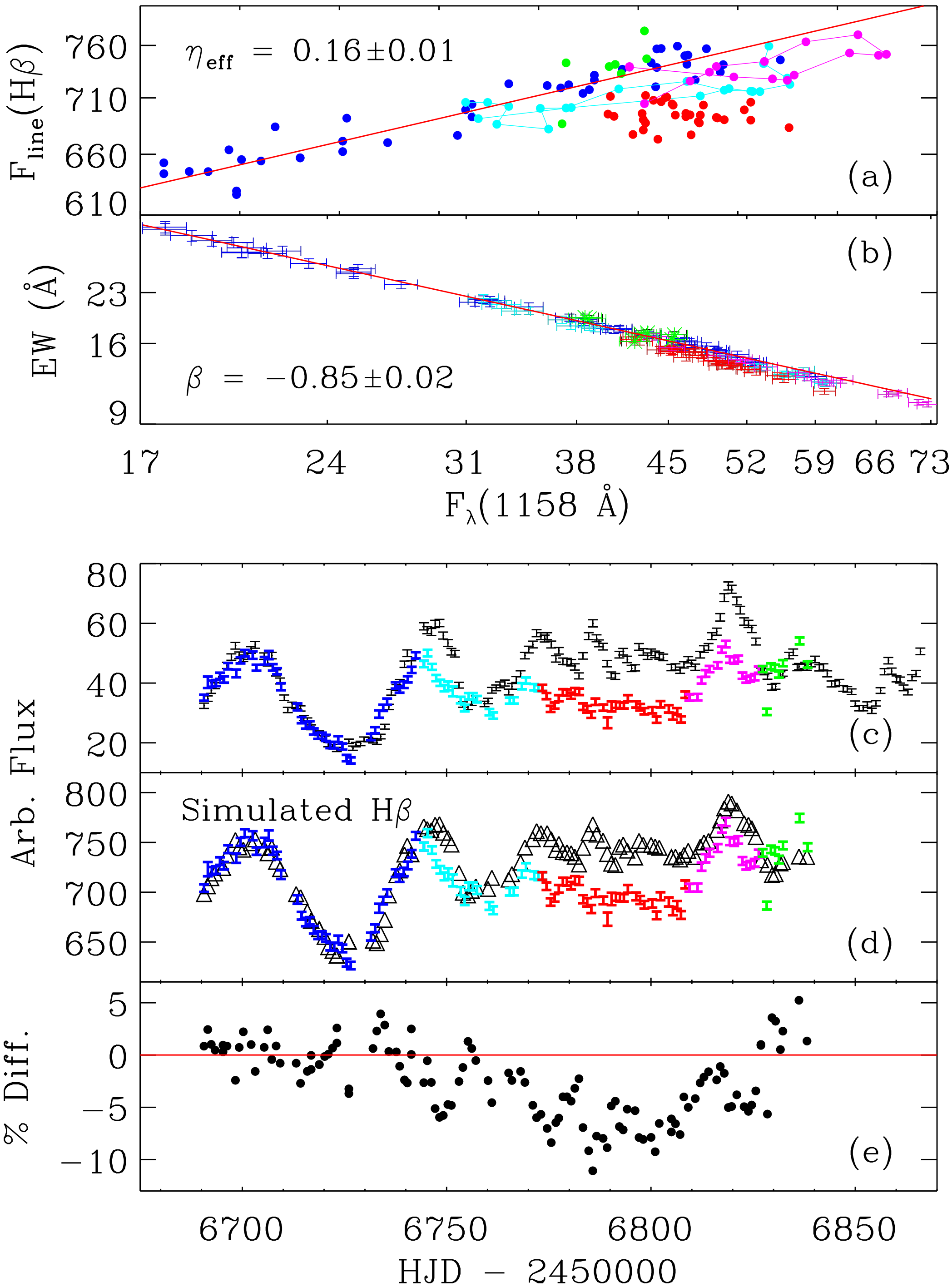

Figure 3.15: Panels (a) and (b) show the Hβ broad-line flux and EW as a function of the 1158 Å continuum flux. Panel (c) shows 1158 Å continuum light curve with the time-shifted Hβ light curve. Panels (d) and (e) show the reconstructed Hβ light curve and the percent of flux lost during the anomaly (see text).

Table 3.6. Broad-Line Responsivity

Line ID	$\eta_{\rm eff}$	β	$f_{\rm lost}$
Lyα	0.30 ± 0.01	-0.73 ± 0.02	9%
Si IV(+O IV])	0.45 ± 0.01	-0.58 ± 0.03	23%
C IV	0.25 ± 0.01	-0.75 ± 0.01	18%
He II(+O III])	0.58 ± 0.04	-0.48 ± 0.04	21%
Hβ	0.16 ± 0.01	-0.85 ± 0.01	7%

Note. — Responsivity values for all broad emission lines in NGC 5548 during this campaign. The first four rows show values from Goad et al. (2016).

using only the blue points corresponding to when the continuum and line light curves are closely correlated during the first half of the campaign. We found that the cyan, red, and magenta points—corresponding to when the light curves are not well-correlated—lie well below the best fits of Equations 3.8 and 3.9 to the blue points. This is the same as what was found for C IV, Lyα, He II(+O III]) and Si IV(+O IV]) in G16. Table 3.6 summarizes the responsivity values for all broad emission lines measured during this campaign. Note that the $\eta_{\rm eff}$ and β values from G16 were computed using data points both before and after the light-curve anomaly (blue and green points), whereas our calculations for Hβ are done using only data points before the anomaly (blue) since the points after the anomaly (green) are affected by inconsistent flux calibrations (see Section 3.2).

To measure the amplitude of the Hβ anomaly, we followed methods described in G16 and used the fitted β value given in Table 3.6 to reconstruct a simulated Hβ light curve that represents what the emission-line light curve would have been if the anomaly had not occurred. The reconstructed light curve is shown as black triangles in Figure 3.15(d), and the observed light curve is shown in color. We define the fraction of the line flux lost as $f_{\rm lost} = [f_{\rm rec} - f_{\rm obs}]$ (Figure 3.15, panel e) and found a time-averaged flux loss of $\sim 7\%$ during the anomaly (red section), which is a smaller deficit than seen for the UV emission lines.

The responsivity of the BLR in NGC 5548 has been studied in detail previously by Goad et al. (2004, GKK04). Table 3.7 summarizes the Hβ responsivity and AGN optical continuum flux values measured by GKK04 for every year of the 13-year monitoring campaign carried out by the AGN Watch consortium (Peterson et al., 2002). We computed the Hβ $\eta_{\rm eff}$ value from our campaign using the AGN 5100 Å continuum after subtracting host-galaxy flux and found $\eta_{\rm eff} = 1.05 \pm 0.01$. Both the responsivity and optical continuum flux during our campaign (7.34×10^{-15} erg s^{-1} cm^{-2} Å^{-1}) are close to those measured in Year 8, despite the fact that the values measured by GKK04 use older measurements of the narrow Hβ and host galaxy fluxes.

The Hβ EW, on the other hand, is relatively lower compared to previous campaigns. The mean AGN optical continuum flux without host galaxy contributions is $\langle f_{\rm AGN} \rangle = 7.37 \times 10^{-15}$ erg s^{-1} cm^{-2} Å^{-1}, and the mean Hβ flux without narrow-line contributions is $\langle f_{{\rm H}\beta} \rangle = 710.45 \times 10^{-15}$ erg s^{-1} cm^{-2}, giving a mean EW of 96.40. Comparing to the Hβ EW computed by Goad & Korista (2014), the value from this campaign is similar only to those measured during the AGN's brightest states.

The Hβ light curve decorrelates from the UV continuum light curve at an earlier time (around THJD 6742) compared to C IV (around THJD 6765 as found by G16). In Method 2 of dividing the light curves, we assume that the Hβ light curve decorrelates and re-correlates with the continuum light curve at the same times as C IV and use the same dividing THJDs as those used in G16 (top panel of Figure 3.16). We find $\eta_{\rm eff} = 0.16 \pm 0.01$ and $\beta = -0.85 \pm 0.02$ for the blue points, which are consistent with the values found using Method 1.

The middle panel of Figure 3.16 shows the He II λ4686 light curve as compared to the far-UV and optical spectroscopic continuum light curves. He II also shows anomalous behavior during the second half of the campaign. However, since the broad He II component is very

Table 3.7. NGC 5548 Hβ Responsivity and AGN Continuum Flux

Year	η_{eff}	$\langle f_{\mathrm{cont}} \rangle$	$\sigma_{\langle f_{\mathrm{cont}} \rangle}$
1	0.56	6.54	1.27
2	0.84	3.79	0.91
3	0.95	6.06	0.92
4	0.94	3.34	1.17
5	0.43	5.69	0.87
6	0.74	6.40	1.11
7	0.68	8.71	1.01
8	0.54	7.07	1.52
9	0.80	4.73	0.89
10	0.51	10.05	1.44
11	0.41	8.48	1.82
12	0.65	3.59	1.20
13	1.00	3.65	0.86
2014	0.51	7.37	0.22

Note. — Fluxes are in units of 10^{-15} erg s^{-1} cm^{-2} Å^{-1}. The first 13 rows show values from Goad et al. (2004), and the last row shows values from this campaign. All η_{eff} values listed were measured with respect to the 5100 Å continuum.

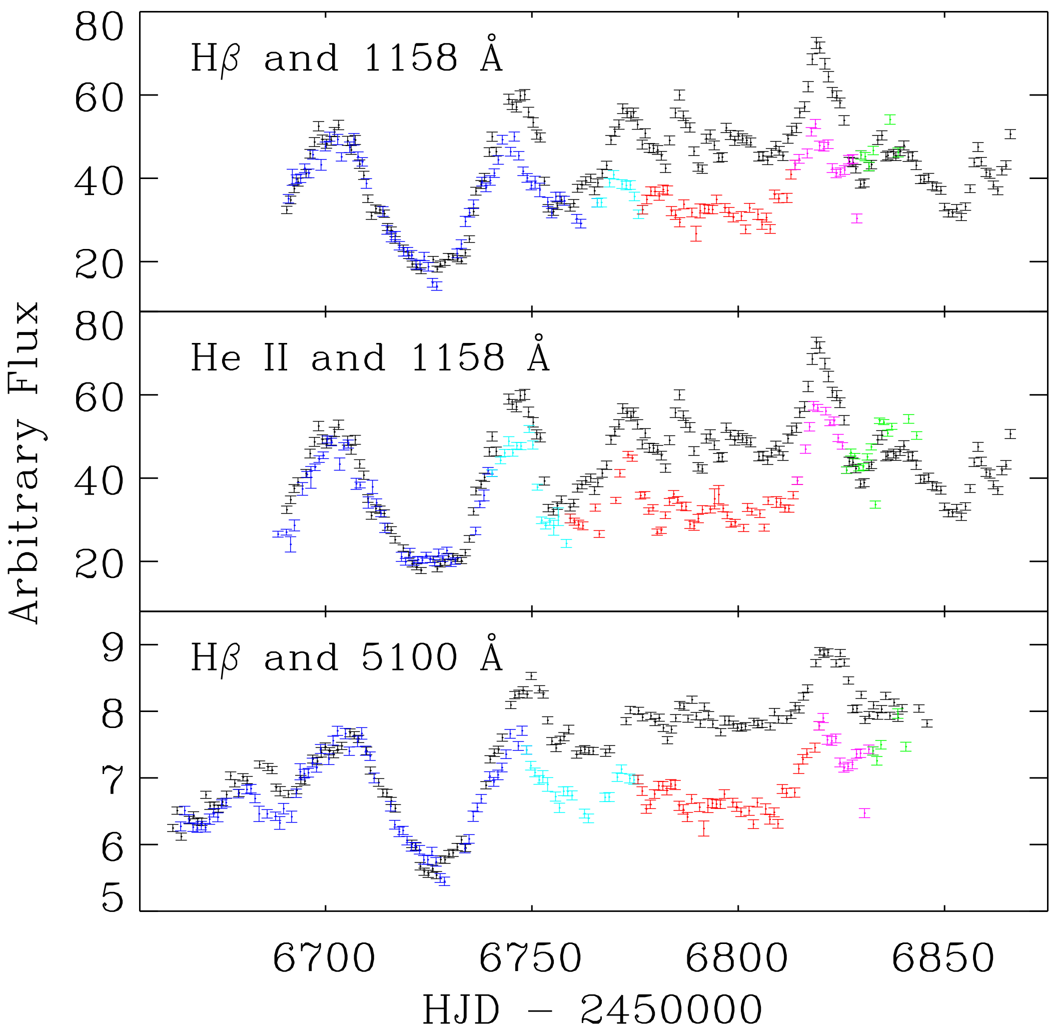

Figure 3.16: *Top:* Hβ and the 1158 Å continuum light curves with the Hβ light curve color-coded as in Goad et al. (2016). *Middle:* He II and the 1158 Å continuum light curves, where the He II light curve is colored by when the line decorrelates from and re-correlate with the continuum. *Bottom:* Hβ light curve (colored using Method 1, see text) and the 5100 Å continuum light curves.

weak and its fitted profile is poorly constrained in the spectral decomposition process, the He II light curve is much noisier than that of Hβ and the $F_{\rm line}$ and EW values are poorly correlated with $F_{\rm cont}$. We therefore do not perform detailed analysis of the responsivity for this emission line.

3.4.3 Line Width and $M_{\rm BH}$ Estimate

The black hole mass in NGC 5548 has been estimated from several previous RM campaigns, including the AGN Watch consortium (Peterson et al., 2002), Bentz et al. (2007), Denney et al. (2009), and Bentz et al. (2009b). The AGN Watch group determined the BH mass using data from each of the program's monitoring years, and subsequent campaigns each produced an independent BH mass value. We computed the BH mass using data from this campaign and compare it with previous results.

We measured the line widths from the Hβ-only mean and rms spectra as shown in Figure 3.5. The narrow Hβ line essentially disappears in the rms spectrum but is still present in the mean spectrum. We removed this emission component by subtracting a Gaussian fit to the Hβ narrow line in the mean MDM spectrum. The resulting spectrum still has some residual narrow Hβ flux since our spectral decomposition routine cannot accurately fit the broad Hβ line core. We linearly interpolate over the residual narrow-line flux as well as the [O III] λ4959 and λ5007 residuals, and the resulting spectrum is plotted in solid black in Figure 3.17.

Two emission-line width values are typically measured in RM: the FWHM and the line dispersion, defined by

$$\sigma_{\rm line}^2 = \left(\frac{c}{\lambda_0}\right)^2 \left(\frac{\sum \lambda_i^2 S_i}{\sum S_i} - \lambda_0^2\right), \tag{3.10}$$

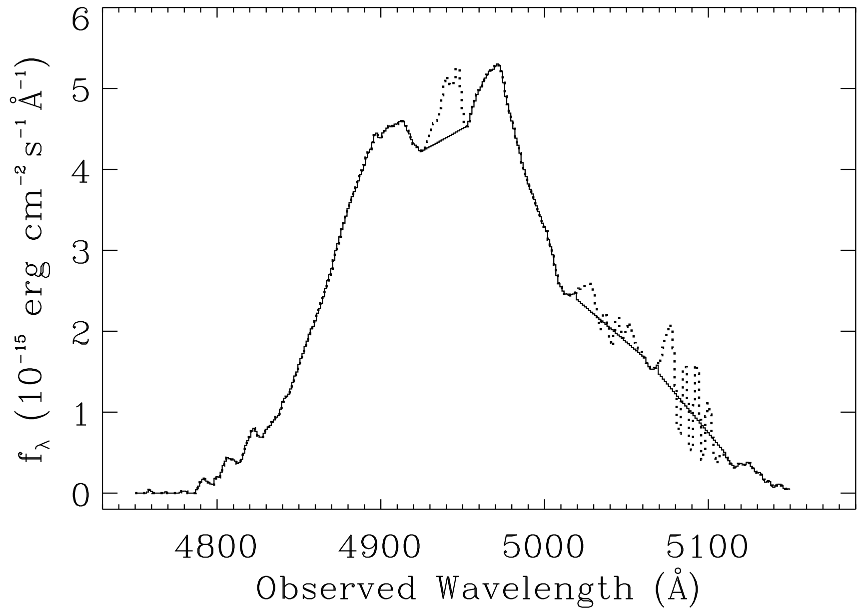

Figure 3.17: Mean Hβ profile after removing the narrow-line component and linearly interpolating over the narrow Hβ and [O III] residuals (solid black). The dotted line shows the spectrum after subtracting the narrow Hβ model but before linear interpolation.

where S_i is the flux density at wavelength bin λ_i and λ_0 is the flux-weighted centroid wavelength of the line profile.

We obtained $\sigma_{\rm line}$ and FWHM for the mean and rms spectra of the full campaign, T1 and T2 periods using the line profile within the wavelength range 4750−5150 Å. We follow procedures described by Peterson et al. (2004) to measure the FWHM of the mean spectrum, which we treat as a double-peaked profile. From each of the two peaks at 4910 Å and 4970 Å, we traced the line profile outward until the flux reached $0.5 f_{\rm max}$, then traced the line profile inward from the continuum until the flux again reached $0.5 f_{\rm max}$. The average of the two wavelengths at $0.5 f_{\rm max}$ is then taken to be the wavelength at half maximum on each side of the profile. The rms profile is more complicated because it has more than two peaks and the troughs between them can reach well below half the maximum flux at each peak. We therefore identified a single maximum flux $f_{\rm max}$ and traced the profile from the continuum toward the center on both sides until the flux reached $0.5 f_{\rm max}$. The separation between the two wavelengths at $0.5 f_{\rm max}$ is taken to be the rms FWHM.

The Hβ line widths and their uncertainties were determined using Monte Carlo bootstrap analysis. With n total spectra, each bootstrap iteration randomly selects n spectra from the dataset with replacement, constructs mean and rms line profiles from this randomly selected sample, and measures the line dispersion and FWHM of these profiles. We constructed a distribution of line dispersion and FWHM values from 10^4 bootstrap iterations, and the median and standard deviation of each distribution are taken to be the values and uncertainties for $\sigma_{\rm line}$ and FWHM.

There are additional systematic uncertainties in the Hβ line widths from using different Fe II templates in spectral decomposition. We repeated the above bootstrap analysis to find Hβ line widths after performing spectral decomposition using the Boroson & Green (1992), Véron-Cetty et al. (2004) and Kovačević et al. (2010) Fe II templates, then took the standard deviation of the Hβ widths measured from using all three Fe II templates as the systematic uncertainty in the true Hβ width. For both $\sigma_{\rm line}$ and FWHM, we added this value in quadrature to the Kovačević et al. (2010) line width uncertainty from bootstrap analysis to obtain the final Hβ line width uncertainty.

The emission-line widths are affected by instrumental broadening due to the wide slits. The observed line width is the quadratic sum of the intrinsic and instrumental line widths ($\sigma^2_{\rm observed} = \sigma^2_{\rm intrinsic} + \sigma^2_{\rm instrumental}$ or similarly for FWHM). To calculate the instrumental broadening through a $5''$ slit, we follow methods described by Bentz et al. (2009b) and compare the [O III] λ5007 line width measured from our observations to the width measured from a higher-resolution observation taken using a narrow ($\sim 2''$) slit, which would represent the intrinsic line width. We measured the FWHM of the [O III] λ5007 model from the MDM mean spectrum to be 9.56 Å, or $\text{FWHM}_{\rm observed} = 563$ km s^{-1}. Whittle (1992) gives the NGC 5548 [O III] line width measured from spectrum taken through a $2''$ slit as $\text{FWHM}_{\rm intrinsic} = 410$ km s^{-1}. Combining these two values, we find the instrumental broadening to be $\text{FWHM}_{\rm inst} = 386$ km s^{-1}, corresponding to $\sigma_{\rm inst} = 164$ km s^{-1} assuming the [O

Table 3.8. Hβ Line Widths

Segment	Spectrum	$\sigma_{\rm line}$ (km s^{-1})	FWHM (km s^{-1})
Full	RMS	4311 ± 586	10155 ± 1425
T1	RMS	4170 ± 491	10316 ± 811
T2	RMS	4859 ± 720	9112 ± 1980
Full	Mean	3961 ± 160	9496 ± 417
T1	Mean	3981 ± 149	9574 ± 447
T2	Mean	3941 ± 173	9380 ± 383

III] line profile is close to Gaussian. We subtract the instrumental widths in quadrature from the Hβ line width measurements to obtain the intrinsic Hβ line widths, which are listed in Table 3.8. The large uncertainties on the FWHM measurements from the rms spectrum are caused by the very jagged shape of the rms profile.

As is common practice in RM, we use the line dispersion as the Hβ width (Peterson et al., 2004) and calculate the virial product defined as VP $= c\tau\Delta V^2/G$. The f factor in Equation 1.2, which incorporates the geometry and kinematics of the BLR, is generally unknown for any individual AGN, so a single value $\langle f \rangle$ is often used to represent the average normalization for all AGN. This value is typically taken to be the scale factor that puts the sample of RM virial products onto the same $M_{\rm BH} - \sigma_\star$ relation as nearby inactive galaxies (Onken et al., 2004; Woo et al., 2010; Graham et al., 2011; Park et al., 2012a; Grier et al., 2013; Ho & Kim, 2015). The value of $\langle f \rangle$ varies depending on what objects are included in the AGN sample and also on the fitting method. We adopt a value of $\langle f \rangle = 4.47$ as calculated by Woo et al. (2015). Since $\langle f \rangle$ is calibrated using Hβ lags measured against the optical continuum, we used the Hβ–optical lag in calculating the VP and BH mass.

Table 3.9 lists the virial products (VP) and the inferred BH masses calculated for the full, T1, and T2 segments. The T1 and T2 $M_{\rm BH}$ estimates are consistent even though the two lags

Table 3.9. Hβ Line Measurements, $M_{\rm BH}$ Estimates, and Continuum Fluxes

Segment	$\sigma_{\rm line}$ (km s^{-1})	$\tau_{\rm optical}$ (days)	Virial Product ($10^7\ M_\odot$)	$M_{\rm BH}$ ($10^7\ M_\odot$)	$f_{5100,\rm total}$ (10^{-15} erg s^{-1} cm^{-2})	$f_{5100,\rm AGN}$
Full	4311 ± 586	$4.21^{+0.40}_{-0.35}$	$1.50^{+0.43}_{-0.43}$	$6.72^{+1.93}_{-1.91}$	11.89 ± 0.22	7.37 ± 0.50
T1	4170 ± 491	$5.12^{+0.38}_{-0.46}$	$1.71^{+0.42}_{-0.43}$	$7.64^{+1.89}_{-1.93}$	11.30 ± 0.45	6.78 ± 0.64
T2	4859 ± 720	$3.13^{+0.73}_{-0.64}$	$1.42^{+0.54}_{-0.51}$	$6.34^{+2.39}_{-2.28}$	12.50 ± 0.49	7.98 ± 0.67

Note. — $\tau_{\rm optical}$ is the ICCF $\tau_{\rm cen}$ value measured against the 5100 Å continuum.

are different by more than 1σ. The full-campaign virial product is entirely consistent with the value obtained by Bentz et al. (2009b) ($1.5^{+0.37}_{-0.51} \times 10^7\ M_\odot$), but the BH mass is a factor of 2 higher than the value determined by Pancoast et al. (2014, P14) from BLR dynamical modeling ($\sim 3.2 \times 10^7\ M_\odot$). This is likely because P14 use the optical continuum as the ionizing source, which we know leads to a shorter Hβ lag than using the UV continuum and can cause the BLR size and subsequent BH mass to be underestimated.

3.5 Discussion

3.5.1 Implications of UV and Optical Hβ Lags

Ground-based RM campaigns have traditionally used the optical continuum light curve—by necessity—to determine emission-line lags, even though the far-UV continuum is a much better proxy for the ionizing source. Emission-line lags relative to the UV continuum ($\tau_{\rm UV}$) thus should yield more accurate estimates of $R_{\rm BLR}$ than their optical lags ($\tau_{\rm optical}$). Our Hβ–UV lag ($\tau_{\rm UV} = 6.26^{+0.47}_{-0.39}$ days) is two days longer than the Hβ–optical lag ($\tau_{\rm optical} = 4.21^{+0.40}_{-0.35}$ days). Given that past measurements of the NGC 5548 Hβ-optical lag range from $\sim$4 to

$\sim$25 days (Bentz et al., 2013, and references therein), the BLR size has been underestimated by $10-50\%$ from optical data alone. There is likely a very short lag (~ 0.1 days) between the 1158 Å continuum and the ionizing continuum at 912 Å, and perhaps a slightly longer lag measured against the continuum from even shorter wavelengths (F16), so the true BLR size may be slightly larger than the value measured using the 1158 Å continuum.

Since virial estimates of $M_{\rm BH}$ scale with $R_{\rm BLR}$, it may seem that this change in the inferred BLR size will change the BH mass estimate for NGC 5548 and other reverberation-mapped AGN. However, the virial product—not the BH mass—is the quantity that is directly affected, and the normalization factor f is still needed to scale the virial product to a calibrated BH mass. If the ratio of the Hβ–UV and Hβ–optical lags ($R_{\rm UV/opt} = \tau_{\rm UV}/\tau_{\rm optical}$) is the same for all AGN, then all RM virial products would be scaled up by a constant value, and a recalibration of f to bring the scaled virial products to the quiescent-galaxy $M_{\rm BH} - \sigma_\star$ relation would nullify the effects of this $R_{\rm BLR}$ bias and leave the RM black hole masses unchanged. There are two AGN in the literature—NGC 4151 and NGC 3227—with BH mass measurements from both RM (Bentz et al., 2006; Denney et al., 2009) and stellar dynamical modeling (Onken et al., 2014; Davies et al., 2006). Comparison of the dynamical modeling black hole masses and the RM virial products for these objects suggests a constant $R_{\rm UV/opt}$. However, many additional measurements of this ratio for other AGN are needed in order to determine whether the RM black hole mass scale is impacted by this effect.

While the discrepancy between $\tau_{\rm UV}$ and $\tau_{\rm optical}$ does not change the RM $M_{\rm BH}$ measurements that use the scale factor f, dynamical models that infer $M_{\rm BH}$ and BLR characteristics (e.g. Pancoast et al., 2011; Li et al., 2013) using only ground-based data *are* directly affected since they do not depend on this virial normalization. The BLR size for each AGN inferred using optical data alone would thus be biased by some factor that depends on the value of $R_{\rm UV/opt}$ for that particular object.

Changes in the inferred BLR size could also have an effect on single-epoch (SE) $M_{\rm BH}$

estimates, which rely on the empirical relation between BLR radius and AGN continuum luminosity ($R_{\rm BLR} \propto L_{\rm AGN}^{\alpha}$, e.g. Laor, 1998; Wandel et al., 1999; Kaspi et al., 2000; McLure & Jarvis, 2002; Kaspi et al., 2005; Vestergaard & Peterson, 2006; Bentz et al., 2006, 2009a, 2013). For example, if $R_{\rm UV/opt}$ is found to correlate with AGN luminosity, then the shape of the $R_{\rm BLR} - L_{\rm AGN}$ relation will change; and if $R_{\rm UV/opt}$ is different for all AGN but is uncorrelated with any other AGN properties, then this would introduce additional scatter to the scaling relation. As the $R_{\rm BLR} - L_{\rm AGN}$ relation is the basis for all SE BH mass estimates at higher redshifts, it is important to explore the potential consequences of this effect by obtaining more simultaneously measured emission-line UV and optical lags from RM over a wide range of AGN luminosities.

We also find that the difference between Hβ lags measured against the far-UV and optical continua ($\tau_{\rm UV} - \tau_{\rm optical} = 2.05^{+0.62}_{-0.52}$ days) is consistent with the optical-to-UV continuum lag ($2.24^{+0.24}_{-0.24}$ days). This would be a reasonable assumption if the BLR gas has a scale height above the plane of the accretion disk that is much smaller than the BLR radius. This campaign provides the first direct test of this assumption. Edelson et al. (2015) and F16 examine the inter-band continuum lags in more detail, and found them to be consistent with a model of standard steady-state accretion disk where the continuum band lags are dominated by light-travel time across the accretion disk. Gardner & Done (2016) argue for an alternative model in which the optical-UV continuum lag is not dominated by the accretion disk reprocessing hard X-ray emission, but is a result of the reprocessing of FUV/EUV continuum from an extended "soft excess" region within dense, optically thick clouds just inside the inner edge of the BLR. We suggest, however, that this reprocessed optical-to-UV continuum must be in addition to that arising from the clouds producing the broad emission lines (Korista & Goad, 2001).

3.5.2 Anomalous Emission-Line Light Curve Behavior

The Hβ light curve anomaly during the T2 period is similar to what is observed for C IV and Lyα (G16). The percent of line flux lost during this event compared to what the flux would have been without the anomaly is higher for Hβ than for the UV lines. The light-curve decorrelation also starts earlier for Hβ than for C IV. Despite these differences, we can conclude that the phenomenon that is causing the C IV light curve anomaly is also affecting Hβ.

G16 suggests two plausible scenarios for this suppression of line flux and variability: (1) a temporary obscuration of the ionizing source by a moving veil of gas between the accretion disk and BLR, and (2) a temporary change in spectral energy distribution of the ionizing source. The first scenario can only account for the emission-line flux suppression, while the second scenario can explain the reduction of both line flux and variability.

The bottom panel of Figure 3.16 shows that the Hβ light curve decorrelation was also clearly detected using only the optical data. If our campaign had lasted for only the duration of T2, we still would have been able to measure the Hβ lags ($\tau_{\rm UV} = 5.95^{+0.79}_{-0.80}$ days and $\tau_{\rm optical} = 3.13^{+0.73}_{-0.64}$ days) with a small formal precision, but the lag signal would be contaminated by other unknown factors and would lead to a very biased estimate of the BLR size. Depending on how common this decorrelation behavior is for Hβ, this effect could contribute to additional scatter in the single-object $R_{\rm BLR} - L_{\rm AGN}$ relations for NGC 5548 and other AGN, which can account for about half of the observed scatter in the global $R_{\rm BLR} - L_{\rm AGN}$ relation for the entire sample of reverberation-mapped AGN (Kilerci Eser et al., 2015).

The long duration and long baseline wavelength coverage of this campaign have both been crucial in detecting and characterizing this decorrelation phenomenon. Horne et al. (2004) found that a campaign duration of at least three times the BLR light-crossing time is needed to recover high-fidelity velocity-delay maps from reverberation mapping data. Given the

Hβ–UV lag of $\sim$ 6 days for NGC 5548 during our monitoring period, the light-crossing time is $\sim$ 12 days and the minimum campaign length would correspond to $\sim$ 40 days, which would not have allowed us to detect the light-curve decorrelation. In order to detect and study these anomalous behaviors in the emission-line light curves, RM campaigns need to be much longer than the minimum requirement for obtaining velocity-delay maps.

Finally, while there aren't any published results documenting such extreme emission-line light curve behavior, it is possible that this decorrelation phenomenon was indeed observed in other AGN in previous RM campaigns but went unrecognized, especially if the campaign had relatively low cadence. Future RM programs designed to obtain data for larger numbers of sources but with lower cadence would also not be able to detect such light-curve decorrelations. This further highlights the importance of high-cadence, long-duration and high-SNR multi-wavelength reverberation datasets in order to determine the prevalence of this phenomenon in AGN.

3.5.3 Comparison to Previous Campaigns: The $R_{\rm BLR} - L_{\rm AGN}$ Relation

We compare our measurements of the NGC 5548 Hβ optical lag and 5100 Å continuum luminosity (L_{5100}) to those obtained in previous RM campaigns spanning 1988 to 2007, a compilation of which was presented by Bentz et al. (2013). The total 5100 Å flux for the full, T1, and T2 segments ($f_{5100,\rm total}$) were measured from their mean spectra and are listed in column 6 of Table 3.9, and column 7 lists the AGN continuum flux after subtracting host-galaxy contributions ($f_{5100,\rm AGN}$). In converting flux measurements to luminosities, we apply a Galactic extinction correction of $E(B-V) = 0.017$ mag (Schlegel et al., 1998; Schlafly & Finkbeiner, 2011) and use a luminosity distance of 75 Mpc following Bentz et al. (2013).

Figure 3.18 plots the BLR size against L_{5100} for measurements from previous campaigns as listed by Bentz et al. (2013) (filled circles) and the full period, T1, and T2 segments from this campaign (open black diamond, open gray triangle, open orange square). The L_{5100} values have been corrected for the variability of [O III] as described by Peterson et al. (2013b), and the uncertainties are from absolute photometric calibration using [O III] $\lambda5007$ and do not include the luminosity distance uncertainty. Denney et al. (2010) monitored NGC 5548 as part of a multi-object RM campaign and found an Hβ ICCF lag of $12.40^{+2.74}_{-3.85}$ days measuring using the 5100 Å continuum. However, the light curves were dominated by a large long-term trend, and after detrending the light curves with a 3rd order polynomial, the Hβ lag becomes $5.07^{+2.46}_{-2.37}$. This updated value is shown as an open circle in Figure 3.18.

Compared to previous results, our $R_{\rm BLR}$ values have significantly smaller uncertainties, which can be attributed to the high cadence and long duration of our ground-based monitoring. Our campaign also yielded much shorter lags compared to previous campaigns during which NGC 5548 was in a similar brightness state. The black line shows a linear least-squares fit to the black data points. Based on this fitted relation, the AGN's luminosity during this campaign would suggest an Hβ lag of ~ 20 days. However, the measured lags for the full campaign, T1, and T2 are all nearly a factor of five shorter than this value. NGC 5548 was also monitored in 2012 (De Rosa et al, in prep), during which its Hβ lag and 5100 Å continuum luminosity were similar to those from our campaign.

It is clear from these results that the $R_{\rm BLR} - L_{\rm AGN}$ relation is much more complex than previously realized. Bentz et al. (2013) found a scatter of only 0.13 dex in the $R_{\rm BLR} - L_{\rm AGN}$ relation for the full sample of reverberation-mapped AGN. However, Du et al. (2015) and Du et al. (2016b) claim that AGN with high accretion rates tend to have shorter lags than predicted by the Bentz et al. (2013) $R_{\rm BLR} - L_{\rm AGN}$ relation given their luminosities. Now, our $R_{\rm BLR}$ and AGN luminosity measurements have shown that even for a single AGN, the $R_{\rm BLR} - L_{\rm AGN}$ relation does not always follow a simple power-law scaling relation, and

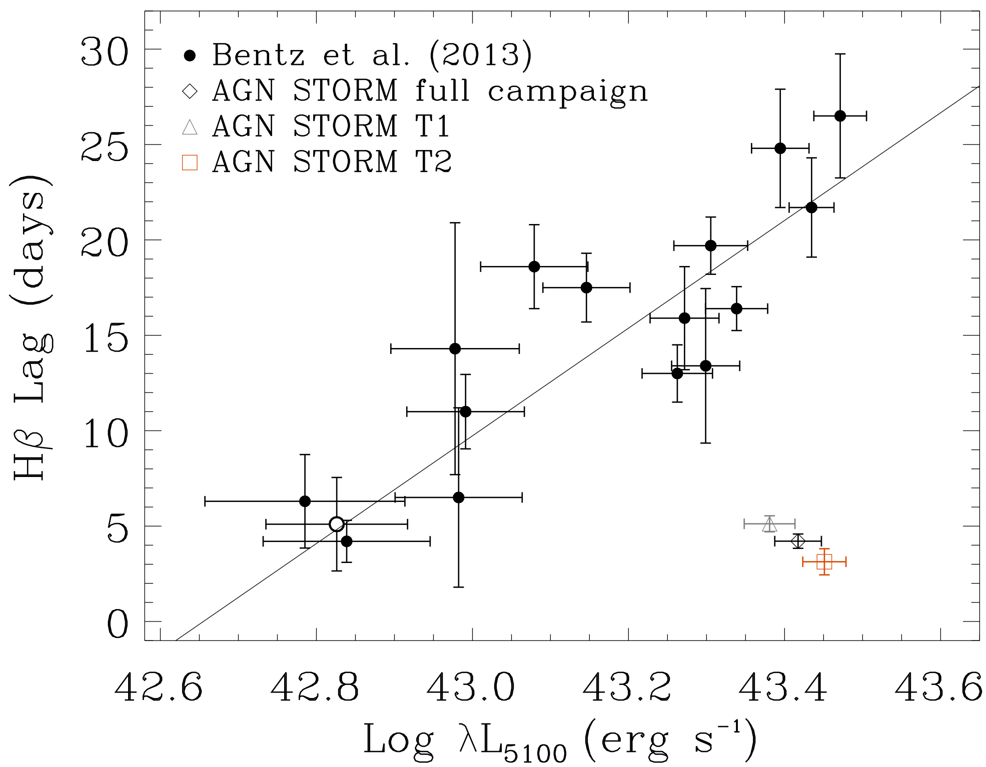

Figure 3.18: NGC 5548 luminosity and Hβ lags measured against the 5100 Å continuum from past campaigns compiled by Bentz et al. (2013) (black dots) and measurements from this campaign (open symbols). The open circle shows the updated lag for Denney et al. (2010, see text). The black line shows a linear least-squares fit to the black data points.

that there may be other, more complex physical processes that contribute to the scatter. Further investigation of the single-object $R_{\rm BLR} - L_{\rm AGN}$ relation is needed in the form of many repeated observation campaigns for individual AGN so that we can track the behavior of each object over a range of timescales and luminosity states. This will, in turn, improve our understanding of the global $R_{\rm BLR} - L_{\rm AGN}$ relation and its implications for both local and high-redshift galaxies.

Chapter 4

Conclusions

This thesis work is divided into two major scientific projects, each presented in a previous chapter. The first project is a reverberation mapping campaign targeting the *Kepler*-field AGN KA1858+4850, and the second project is a detailed study of the broad line region in the galaxy NGC 5548. The major results of each project and relevant future work are summarized in this chapter.

4.1 Reverberation Mapping of KA1858+4850

We photometrically and spectroscopically monitored the *Kepler*-field AGN KA1858+4850 over a period of nine months. We found an Hβ rest-frame lag of $13.53^{+2.03}_{-2.32}$ days with respect to continuum variations using cross-correlation methods, and a lag of $13.15^{+1.08}_{-1.00}$ days using the `JAVELIN` method. We also measured emission-line lags with respect to the *Kepler* light curve and found slightly shorter lags compared to those measured against the V-band light curve, which is expected given the contributions of broad emission lines and red continuum flux to the *Kepler* band. We measured an Hβ velocity dispersion of $\sigma_{\rm line} = 770 \pm 49$ km s^{-1}, and calculated a black hole virial mass of $M_{\rm BH} = 8.06^{+1.59}_{-1.72} \times 10^6\ M_\odot$ using $\tau_{\rm CCF}$ and scale factor empirically derived from local active galaxies by Park et al. (2012a), and a black hole mass of $M_{\rm BH,\texttt{JAVELIN}} = 6.58^{+1.00}_{-0.98} \times 10^6\ M_\odot$ using $\tau_{\texttt{JAVELIN}}$ and scale factor taken from Grier et al. (2013). For this mass, the Eddington ratio is $L/L_{\rm Edd} \approx 0.2$.

KA1858+4850 was the second AGN for which data was obtained in this interrupt observing mode from Lick Observatory, and the second AGN in the *Kepler* field to be monitored by ground-based telescopes (the first being Zw 229-015, Barth et al. 2011b). Comparing our lag results with those obtained by the LAMP 2008 collaboration (Bentz et al., 2009a), our lag uncertainties are slightly larger. However, considering the much longer lag of KA1858+4850, our Hβ fractional lag precision, at less than 20%, is still very good. Our analysis using *Kepler* light curves also offers one of the first direct comparison of reverberation mapping results between ground- and space-based observations for a *Kepler* AGN. The success of our campaign demonstrates the robust capabilities of interrupt-mode observations for monitoring AGN variability. Factors that negatively impact our measurements, such as inconsistency in data quality and gaps in the spectroscopic light curves (in this case due to the AGN being observed only during dark runs), are mitigated by a well-sampled V-band light curve obtained by combining observations from several ground-based telescopes as well as the long duration of the program.

Thanks to the *Kepler* mission, the light curve of KA1858+4850 has among the highest cadences and signal-to-noise ratios ever measured for an active galactic nucleus. Thus, our black hole mass measurement will serve as a reference point for relations between black hole mass and continuum variability characteristics in active galactic nuclei. Further observations of KA1858+4850 can also provide additional insight into various properties of the host galaxy. Specifically, observations of the bulge properties can put KA1858+4850 on the $M_{\rm BH} - L_{\rm bulge}$, $M_{\rm BH} - M_{\rm bulge}$, and $M_{\rm BH} - \sigma_*$ relations. Since the host galaxy is very compact, high-resolution HST or adaptive optics imaging will be needed to examine the host-galaxy morphology.

4.2 The Broad Line Region in NGC 5548

We presented the results of an optical spectroscopic monitoring program in 2014 targeting the galaxy NGC 5548 as part of the AGN STORM collaboration. Our campaign spanned six months and achieved almost daily cadence. We determined Hβ and He II λ4686 emission-line lags relative to the far-UV and optical continua and found that the lag measured against the UV continuum is approximately two days longer than that measured against the optical continuum. Given that past measurements of the NGC 5548 Hβ lag against the optical continuum range from ~ 4 to ~ 25 days, the BLR size inferred from previous data is likely biased low by $10 - 50\%$. The difference between the Hβ-to-UV and Hβ-to-optical lags is consistent with the lag between the UV and optical continua.

If the ratio of UV and optical Hβ lags is not the same for all AGN, but scales with luminosity or BH mass, then both the virial normalization factor f and the shape of the Hβ $R_{\rm BLR}-L_{\rm AGN}$ relation will change, which would have direct impact on single-epoch $M_{\rm BH}$ estimates for high-redshift AGN. It is therefore imperative that we obtain more Hβ lags measured against simultaneously observed UV and optical continua in order to examine the ratio between $\tau_{\rm UV}$ and $\tau_{\rm optical}$ for other objects and understand this systematic effect.

We also obtained velocity-resolved lags for the broad Hβ line and found a double-peaked lag profile as a function of wavelength, with shorter lags in the high-velocity wings. The overall shape of the lag profile has qualitatively similar structure to those of Keplerian models (e.g. Horne et al., 2004), and is very similar to what is found for Lyα (De Rosa et al., 2015). Both the Hβ and He II emission lines exhibit changes in their response to UV continuum variations about halfway through our monitoring campaign. The line light curves decorrelate from the continuum light curve by decreasing in flux when the continuum light curve flux increased, then staying at a suppressed state until near the end of the campaign. The same phenomenon is observed for all the UV emission lines. Further investigation into the simultaneous UV and optical line responses during this campaign may elucidate the cause of this change in BLR responsivity. Depending on how frequently this decorrelation between line and continuum light curves occurs in the AGN population as a whole, this effect could contribute to scatter in single-object and global $R_{\rm BLR} - L_{\rm AGN}$ relations.

The anomaly in the emission-line responses was detectable because of the high cadence, long duration, and excellent data quality of this campaign. Shorter monitoring programs, where the campaign duration is only a few times the expected line lag, and future RM campaigns aiming to obtain data for more objects with lower cadence would both have difficulty detecting this effect. Thus, more high-cadence, long-duration, and high-quality monitoring campaigns targeting other AGN are needed in order to understand the frequency of this decorrelation phenomenon.

Finally, we determined that, given the optical luminosity of NGC 5548 during our campaign, the measured Hβ lag is a factor of five shorter than the expected value based on the $R_{\rm BLR} - L_{\rm AGN}$ relation measured for NGC 5548 from past monitoring campaigns. This demonstrates that the AGN does not follow a simple power-law $R_{\rm BLR} - L_{\rm AGN}$ relation at all times. Further investigation of the single-object $R_{\rm BLR} - L_{\rm AGN}$ relation in the form of many repeated observation campaigns for individual AGN will help to track the behavior of each object over a range of timescales and luminosity states.

Bibliography

Antonucci, R. R. J., & Cohen, R. D. 1983, ApJ, 271, 564

Barth, A. J., et al. 2015, ApJS, 217, 26

Barth, A. J., & Bentz, M. C. 2016, MNRAS, 458, L109

Barth, A. J., et al. 2011a, ApJ, 732, 121

—. 2011b, ApJ, 732, 121

—. 2013, ApJ, 769, 128

Bauer, A., Baltay, C., Coppi, P., Ellman, N., Jerke, J., Rabinowitz, D., & Scalzo, R. 2009, ApJ, 696, 1241

Bentz, M. C., et al. 2007, ApJ, 662, 205

—. 2013, ApJ, 767, 149

—. 2010a, ApJL, 720, L46

Bentz, M. C., & Katz, S. 2015, PASP, 127, 67

Bentz, M. C., Peterson, B. M., Netzer, H., Pogge, R. W., & Vestergaard, M. 2009a, ApJ, 697, 160

Bentz, M. C., Peterson, B. M., Pogge, R. W., Vestergaard, M., & Onken, C. A. 2006, ApJ, 644, 133

Bentz, M. C., et al. 2009b, ApJ, 705, 199

—. 2010b, ApJ, 716, 993

Blandford, R. D., & McKee, C. F. 1982, ApJ, 255, 419

Boroson, T. A., & Green, R. F. 1992, ApJS, 80, 109

Borucki, W. J., et al. 2010, Science, 327, 977

Brown, T. M., et al. 2013, PASP, 125, 1031

Bruzual, G., & Charlot, S. 2003, MNRAS, 344, 1000

Cid Fernandes, Jr., R., Aretxaga, I., & Terlevich, R. 1996, MNRAS, 282, 1191

Clavel, J., et al. 1991, ApJ, 366, 64

Collier, S., & Peterson, B. M. 2001, ApJ, 555, 775

Collier, S. J., et al. 1998, ApJ, 500, 162

Crenshaw, D. M., & Blackwell, Jr., J. H. 1990, ApJL, 358, L37

Cristiani, S., Vio, R., & Andreani, P. 1990, AJ, 100, 56

Czerny, B., Doroshenko, V. T., Nikołajuk, M., Schwarzenberg-Czerny, A., Loska, Z., & Madejski, G. 2003, MNRAS, 342, 1222

Czerny, B., Schwarzenberg-Czerny, A., & Loska, Z. 1999, MNRAS, 303, 148

Davies, R. I., et al. 2006, ApJ, 646, 754

De Rosa, G., et al. 2015, ApJ, 806, 128

—. 2014, ApJ, 790, 145

Denney, K. D., et al. 2006, ApJ, 653, 152

—. 2010, ApJ, 721, 715

—. 2009, ApJL, 704, L80

Dietrich, M., et al. 1993, ApJ, 408, 416

—. 1998, ApJS, 115, 185

Done, C., & Krolik, J. H. 1996, ApJ, 463, 144

Du, P., et al. 2015, ApJ, 806, 22

—. 2014, ApJ, 782, 45

—. 2016a, ArXiv e-prints

—. 2016b, ArXiv e-prints

Edelson, R., et al. 2015, ApJ, 806, 129

Edelson, R., & Malkan, M. 2012, ApJ, 751, 52

Fausnaugh, M. M., et al. 2016, ApJ, 821, 56

Ferrarese, L., & Merritt, D. 2000, ApJL, 539, L9

Filippenko, A. V. 1982, PASP, 94, 715

Filippenko, A. V., Li, W. D., Treffers, R. R., & Modjaz, M. 2001, in Astronomical Society of the Pacific Conference Series, Vol. 246, IAU Colloq. 183: Small Telescope Astronomy on Global Scales, ed. B. Paczynski, W.-P. Chen, & C. Lemme, 121

Gardner, E., & Done, C. 2016, ArXiv e-prints

Gaskell, C. M. 1988, ApJ, 325, 114

Gaskell, C. M., & Goosmann, R. W. 2013, ApJ, 769, 30

—. 2016, Ap&SS, 361, 67

Gaskell, C. M., & Peterson, B. M. 1987, ApJS, 65, 1

Gaskell, C. M., & Sparke, L. S. 1986, ApJ, 305, 175

Gebhardt, K., et al. 2000, ApJL, 539, L13

Giallongo, E., Trevese, D., & Vagnetti, F. 1991, ApJ, 377, 345

Gilbert, K. M., & Peterson, B. M. 2003, ApJ, 587, 123

Giveon, U., Maoz, D., Kaspi, S., Netzer, H., & Smith, P. S. 1999, MNRAS, 306, 637

Goad, M. R., & Korista, K. T. 2014, MNRAS, 444, 43

Goad, M. R., et al. 2016, ArXiv e-prints

Goad, M. R., Korista, K. T., & Knigge, C. 2004, MNRAS, 352, 277

Goad, M. R., Korista, K. T., & Ruff, A. J. 2012, MNRAS, 426, 3086

Graham, A. W., Onken, C. A., Athanassoula, E., & Combes, F. 2011, MNRAS, 412, 2211

Greene, J. E., et al. 2010, ApJ, 721, 26

Grier, C. J., et al. 2013, ApJ, 773, 90

Gültekin, K., et al. 2009, ApJ, 698, 198

Ho, L. C., & Kim, M. 2014, ApJ, 789, 17

—. 2015, ApJ, 809, 123

Hook, I. M., McMahon, R. G., Boyle, B. J., & Irwin, M. J. 1994, MNRAS, 268, 305

Horne, K. 1986, PASP, 98, 609

Horne, K., Peterson, B. M., Collier, S. J., & Netzer, H. 2004, PASP, 116, 465

Horne, K., Welsh, W. F., & Peterson, B. M. 1991, ApJL, 367, L5

Kaspi, S., Maoz, D., Netzer, H., Peterson, B. M., Vestergaard, M., & Jannuzi, B. T. 2005, ApJ, 629, 61

Kaspi, S., Smith, P. S., Netzer, H., Maoz, D., Jannuzi, B. T., & Giveon, U. 2000, ApJ, 533, 631

Kelly, B. C., Bechtold, J., & Siemiginowska, A. 2009, ApJ, 698, 895

Kilerci Eser, E., Vestergaard, M., Peterson, B. M., Denney, K. D., & Bentz, M. C. 2015, ApJ, 801, 8

Kollatschny, W. 2003, A&A, 407, 461

Korista, K. T., et al. 1995, ApJS, 97, 285

Korista, K. T., & Goad, M. R. 2001, ApJ, 553, 695

—. 2004, ApJ, 606, 749

Kormendy, J., & Ho, L. C. 2013, ARA&A, 51, 511

Kovačević, J., Popović, L. Č., & Dimitrijević, M. S. 2010, ApJS, 189, 15

Kozłowski, S., et al. 2010, ApJ, 708, 927

Krolik, J. H., Horne, K., Kallman, T. R., Malkan, M. A., Edelson, R. A., & Kriss, G. A. 1991, ApJ, 371, 541

Landolt, A. U. 1992, AJ, 104, 340

Lang, D., Hogg, D. W., Mierle, K., Blanton, M., & Roweis, S. 2010, AJ, 139, 1782

Laor, A. 1998, ApJL, 505, L83

Leighly, K. M., & Moore, J. R. 2004, ApJ, 611, 107

Li, Y.-R., Wang, J.-M., Ho, L. C., Du, P., & Bai, J.-M. 2013, ApJ, 779, 110

MacLeod, C. L., et al. 2010, ApJ, 721, 1014

McHardy, I. M., et al. 2014, MNRAS, 444, 1469

McLure, R. J., & Jarvis, M. J. 2002, MNRAS, 337, 109

Murray, N., & Chiang, J. 1997, ApJ, 474, 91

Mushotzky, R. F., Edelson, R., Baumgartner, W., & Gandhi, P. 2011, ApJL, 743, L12

Nenkova, M., Sirocky, M. M., Nikutta, R., Ivezić, Ž., & Elitzur, M. 2008, ApJ, 685, 160

Netzer, H. 2015, ARA&A, 53, 365

Netzer, H., & Laor, A. 1993, ApJL, 404, L51

Onken, C. A., Ferrarese, L., Merritt, D., Peterson, B. M., Pogge, R. W., Vestergaard, M., & Wandel, A. 2004, ApJ, 615, 645

Onken, C. A., et al. 2014, ApJ, 791, 37

Pancoast, A., Brewer, B. J., & Treu, T. 2011, ApJ, 730, 139

Pancoast, A., Brewer, B. J., Treu, T., Park, D., Barth, A. J., Bentz, M. C., & Woo, J.-H. 2013, ArXiv e-prints

—. 2014, MNRAS, 445, 3073

Park, D., Kelly, B. C., Woo, J.-H., & Treu, T. 2012a, ApJS, 203, 6

Park, D., et al. 2012b, ApJ, 747, 30

Peterson, B. M. 1993, PASP, 105, 247

Peterson, B. M. 2006, in Astronomical Society of the Pacific Conference Series, Vol. 360, Astronomical Society of the Pacific Conference Series, ed. C. M. Gaskell, I. M. McHardy, B. M. Peterson, & S. G. Sergeev, 191

Peterson, B. M., et al. 1991, ApJ, 368, 119

—. 1999, ApJ, 510, 659

—. 2002, ApJ, 581, 197

—. 2013a, ApJ, 779, 109

—. 2013b, ApJ, 779, 109

Peterson, B. M., & Ferland, G. J. 1986, Nature, 324, 345

Peterson, B. M., et al. 2004, ApJ, 613, 682

Peterson, B. M., & Horne, K. 2004, Astronomische Nachrichten, 325, 248

Peterson, B. M., Pogge, R. W., Wanders, I., Smith, S. M., & Romanishin, W. 1995, PASP, 107, 579

Peterson, B. M., Wanders, I., Bertram, R., Hunley, J. F., Pogge, R. W., & Wagner, R. M. 1998, ApJ, 501, 82

Pogge, R. W. 2011, in Narrow-Line Seyfert 1 Galaxies and their Place in the Universe

Pogge, R. W., & Peterson, B. M. 1992, AJ, 103, 1084

Rees, M. J., Netzer, H., & Ferland, G. J. 1989, ApJ, 347, 640

Reichert, G. A., et al. 1994, ApJ, 425, 582

Revalski, M., Nowak, D., Wiita, P. J., Wehrle, A. E., & Unwin, S. C. 2014, ApJ, 785, 60

Rodriguez-Pascual, P. M., et al. 1997, ApJS, 110, 9

Rosenblatt, E. I., & Malkan, M. A. 1990, ApJ, 350, 132

Santos-Lleó, M., et al. 1997, ApJS, 112, 271

Schlafly, E. F., & Finkbeiner, D. P. 2011, ApJ, 737, 103

Schlegel, D. J., Finkbeiner, D. P., & Davis, M. 1998, ApJ, 500, 525

Sergeev, S. G., Doroshenko, V. T., Golubinskiy, Y. V., Merkulova, N. I., & Sergeeva, E. A. 2005, ApJ, 622, 129

Shakura, N. I., & Sunyaev, R. A. 1973, A&A, 24, 337

Shappee, B. J., et al. 2014, ApJ, 788, 48

Still, M., & Barclay, T. 2012, PyKE: Reduction and analysis of Kepler Simple Aperture Photometry data, astrophysics Source Code Library

Stirpe, G. M., et al. 1994, ApJ, 425, 609

Timmer, J., & Koenig, M. 1995, A&A, 300, 707

Ulrich, M. H., et al. 1984, MNRAS, 206, 221

Ulrich, M.-H., & Horne, K. 1996, MNRAS, 283, 748

Urry, C. M., & Padovani, P. 1995, PASP, 107, 803

van Dokkum, P. G. 2001a, PASP, 113, 1420

—. 2001b, PASP, 113, 1420

van Groningen, E., & Wanders, I. 1992a, PASP, 104, 700

—. 1992b, PASP, 104, 700

Vanden Berk, D. E., et al. 2004, ApJ, 601, 692

Véron-Cetty, M.-P., Joly, M., & Véron, P. 2004, A&A, 417, 515

Vestergaard, M., & Peterson, B. M. 2006, ApJ, 641, 689

Voges, W., et al. 1999, VizieR Online Data Catalog, 9010, 0

Wandel, A., Peterson, B. M., & Malkan, M. A. 1999, ApJ, 526, 579

Wanders, I., et al. 1995, ApJL, 453, L87

—. 1997, ApJS, 113, 69

Webb, W., & Malkan, M. 2000, ApJ, 540, 652

Welsh, W. F. 1999, PASP, 111, 1347

Welsh, W. F., & Horne, K. 1991, ApJ, 379, 586

Welsh, W. F., Martino, D. L., Kawaguchi, G., & Kollatschny, W. 2007, in Astronomical Society of the Pacific Conference Series, Vol. 373, The Central Engine of Active Galactic Nuclei, ed. L. C. Ho & J.-W. Wang, 29

White, R. J., & Peterson, B. M. 1994, PASP, 106, 879

Whittle, M. 1992, ApJS, 79, 49

Wilhite, B. C., Brunner, R. J., Grier, C. J., Schneider, D. P., & vanden Berk, D. E. 2008, MNRAS, 383, 1232

Wold, M., Brotherton, M. S., & Shang, Z. 2007, MNRAS, 375, 989

Woo, J.-H., Schulze, A., Park, D., Kang, W.-R., Kim, S. C., & Riechers, D. A. 2013, ApJ, 772, 49

Woo, J.-H., et al. 2010, ApJ, 716, 269

Woo, J.-H., Yoon, Y., Park, S., Park, D., & Kim, S. C. 2015, ApJ, 801, 38

Zu, Y., Kochanek, C. S., & Peterson, B. M. 2011, ApJ, 735, 80

Appendix A

Aperture Photometry Pipeline

A.1 Background

One of the two crucial components in any RM campaign is a light curve of the AGN continuum, typically obtained in one of two ways. The first is by measuring the spectral flux at the rest-frame wavelength 5100 Å for each epoch in the spectroscopic time series. This method uses the same set of spectra for both the emission line flux and the AGN continuum flux, and can thus introduce significant correlated errors when computing the cross-correlation between the two light curves. To avoid these correlated errors, the second method of obtaining continuum light curve from photometric monitoring is often preferred in RM.

Photometric light curves can be measured using either difference imaging or aperture photometry. Difference imaging, in its simplest form, takes the difference of two images of the same field with the same point spread functions (PSFs), taken at different times. In the residual image, all constant-brightness objects should disappear and only the variable objects would remain. To construct a light curve, a constant template image is subtracted from all images in a time series, and the residual flux is measured for each image to produce a light curve showing relative variability. This method can yield high-precision variability measurements if implemented successfully. However, matching the PSFs of all the images in an RM campaign can be very challenging, and requires high SNR data, high-precision flat fielding, and many constant-flux reference stars in the field of view.

Aperture photometry, on the other hand, has less stringent requirements for the quality of a photometric data set. It involves simply summing up all the light from a source within a defined aperture and subtracting the background light measured using an annulus surrounding the aperture. Given the centroid pixel value of a source in an image, the aperture size, and the inner and outer radii of the sky annulus, the IDL routine `aper` easily performs this task and outputs a brightness magnitude for the source assuming some zero-point magnitude offset. To make a light curve, aperture photometry magnitudes are computed for the variable source and several constant-flux reference stars, and statistical analysis is then performed on the reference star magnitudes in order to calibrate the night-to-night variations due to changes in observing conditions.

Large RM campaigns often involve hundreds of images taken by several different telescopes, so it can be very time-consuming and inefficient to perform aperture photometry on the AGN and reference stars by hand. Additionally, it is often useful to photometrically monitor potential RM targets for a short period of time before the start of the campaign in order to determine whether they are in a highly variable state and thus suitable for RM. In order to monitor the AGN's variability in real time, the light curve would need to be updated frequently as new observations are taken. This would be very difficult to do with difference imaging or if flux measurements and light curve calibrations were done manually. The photometry pipeline I developed—`Autophot`—aims to address these challenges in efficiently processing large amounts of photometric data for variable sources.

A.2 `Autophot`

Prior to being processed by `Autophot`, all images must go through the standard set of photometric data reduction procedures, including overscan correction, trimming, bias subtraction, flat fielding, and cosmic ray cleaning (L.A.Cosmic routine, van Dokkum, 2001a). The images must also be mapped onto celestial coordinates, which allows the automatic detection of the AGN and reference-star locations. Some telescopes, such as those in the Las Cumbres Observatory Global Telescope network, will produce data with celestial coordinates already mapped onto them as part of the standard data reduction pipeline. For images from most other telescopes, this can be done using the *Astrometry.net* software (Lang et al., 2010). Images must also have HJD values recorded in their headers.

For each AGN, reference stars must be selected in the object's field of view and their celestial coordinates must be recorded in a text file that is taken as input by `Autophot`. Reference stars are typically selected to have V-band magnitudes simiar to or brighter than the AGN magnitude. It is always better to have more reference stars to make the light curve calibrations more robust, however a minimum of six objects is highly recommended. The pipeline uses a library of gain, read noise, and pixel scale values for 18 different telescopes and instruments, and the library can be extended to include any new telescopes producing data to be processed by `Autophot`.

The steps taken by `Autophot` to create an AGN light curve using data from multiple telescopes are as follows. (Steps 1–6 are done for data from each individual telescope. N is the number of points in the data set and M is the number of reference stars.)

1. Aperture photometry magnitudes are calculated for the AGN and all reference stars for each image in the time series using the IDL `aper` routine. Magnitudes for images taken within a certain period of each other—with the time period specified by the user—are

averaged, and magnitude uncertainties are propagated through all subsequent steps.

2. The mean magnitude for each reference star $\bar{v}_m$ is computed for the entire time series. Any reference stars showing brightness variations above a set threshold is considered to be possibly variable and removed from the analysis.

3. For each epoch n, a magnitude shift s_n is computed as

$$s_n = \frac{1}{M}\sum_{i=1}^{M} s_{n,m} \qquad \text{and} \qquad s_{n,m} = \bar{v}_m - v_{m,n}, \tag{A.1}$$

where $v_{m,n}$ is the magnitude for the reference star m in epoch n.

4. Any reference star with an $s_{n,m}$ value significantly different from those of other reference stars will be discarded from the analysis for epoch n only. (This means that if a reference star has a bad pixel or cosmic ray in the aperature for just one image, the magnitude measurement for that image is not used for calibrations, but the reference star is not discarded completely.) s_n is then recomputed and the shift is applied to the AGN and reference star magnitudes for each epoch.

5. Steps 2–4 are repeated two more times.

6. Additional error in the final AGN magnitudes, such as those due to inconsistencies in flat-field corrections and poor reference-star magnitude measurements owing to blemishes on the detector, are determined by first computing the excess variance in each of the scaled reference star light curves, defined as

$$\sigma_m^2 = \frac{1}{N}\sum_{i=1}^{N} [(\bar{v} - v_{m,n})^2 - \sigma_{m,n}^2], \tag{A.2}$$

where $\sigma_{m,n}^2$ is the measurement uncertainty, then taking the mean of the excess varaince values for all the reference stars and adding it in quadrature to the AGN magnitude uncertainties.

7. Light curves from different telescopes are inter-calibrated by finding pairs of nearly contemporaneous points between each dataset and the pre-selected "anchor" light curve (typicall chosen to be the dataset with the longest temporal baseline and highest sampling cadence), then using a linear least-squares fit to compute the optimal scale factor and shift values to put each light curve onto the same scale as the anchor light curve.

A.3 Applications and Sample Light Curves

The automated nature of this pipeline enables it to process a large number of images at once and to rapidly produce and update AGN light curves as new data are acquired. It is thus extremely useful for monitoring AGN variability in real time to quickly determine if potential RM targets are highly variable. Figure A.1 shows the V-band light curve for RBS 1573, a potential RM target for the LCOGT FLOYDS spectrograph in 2013. This AGN was monitored for nearly six months using six identical robotic, 1-m telescopes in the LCOGT network, and this photometric light curve, produced within hours of collecting the full dataset, was used in a proposal to show that the AGN was indeed varying strongly and thus ideal as an RM target.

In addition to working with typical RM datasets, `Autophot` is also able to produce light curves for data taken over much shorter and much longer timescales. Figure A.2 shows the light curve for a rapidly varying blazar, Mrk 501. This object was observed at West Mountain Observatory over a period of less than five hours, and coherent variability showing flare events are clearly visible in the blazar light curve. Figure A.3 shows a light curve of Zw 229-015, the brightest *Kepler*-field AGN, from nearly five years of ground-based observations. While *Kepler* has observed this object with an exquisitely fine sampling cadence of 30 minutes,

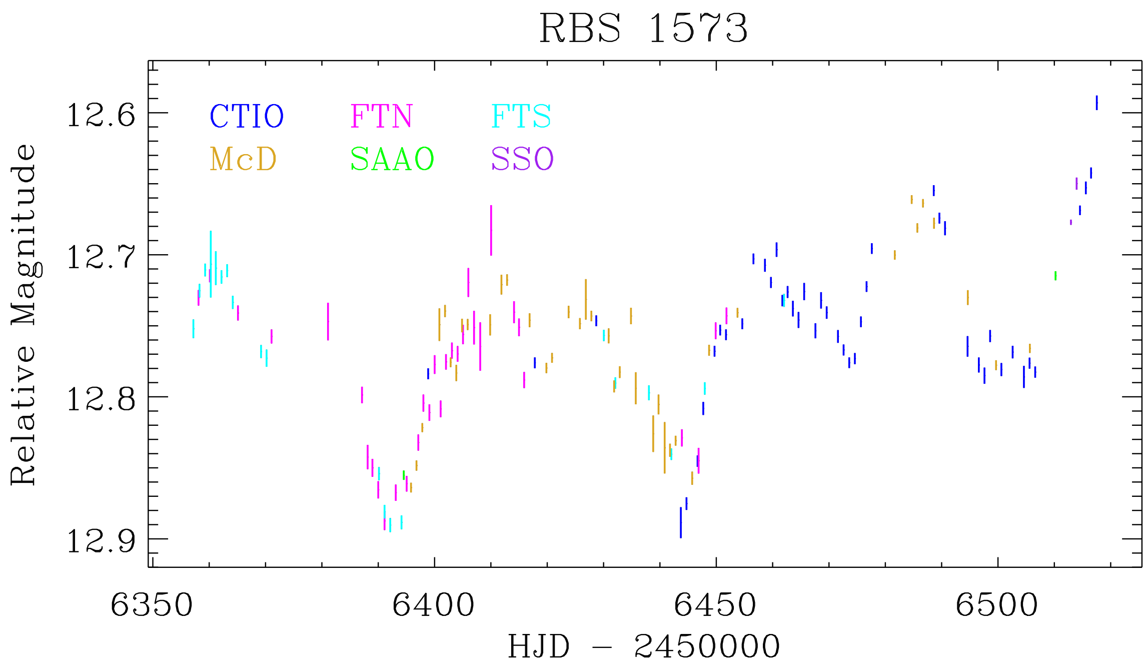

Figure A.1: V-band light curve of RBS 1573 from six robotic 1-m telescopes in the LCOGT network: Cerro Tololo Inter-American Observatory (CTIO), Faulkes Telescope North (FTN), Faulkes Telescope South (FTS), McDonald Observatory (McD), South African Astronomy Observatory (SAAO), and Siding Spring Observatory (SSO).

light curves from individual quarters are disjointed from each other (see Section 2.3.2). This light curve will be highly effective in calibrating the quarterly *Kepler* light curves onto a common flux scale. The same light curve is plotted in Figure A.4, but stretched out over three panels to show short-term variability.

The IDL scripts used to perform `Autophot` has been distributed to and used by various collaborators, including professors, research scientists, and undergraduate students. I used this pipeline to produce light curves for several targets in the 2011 Lick AGN Monitoring Project (LAMP) (Pancoast et al., *in prep*), and a junior researcher in the Barth group is using this pipeline to create light curves for the LAMP 2016 project, which targets AGNs with higher luminosities and Hβ lags than the current sample of RM objects. `Autophot` has also been used by an undergraduate student to search through the Intermediate Palomar Transient Factory survey data and archival Lick Observatory KAIT data for variable AGNs, and its utility can be extended to photometric time-domain studies of all variable objects.

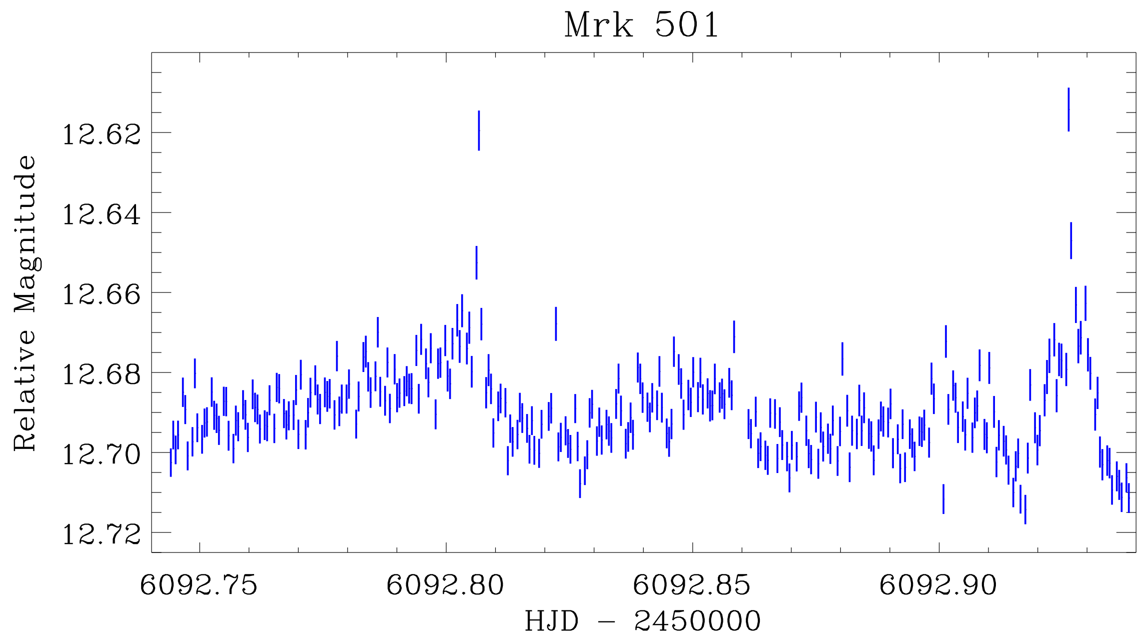

Figure A.2: V-band light curve of the blazar Mrk 501, observed at the West Mountain Observatory over a period of less than five hours.

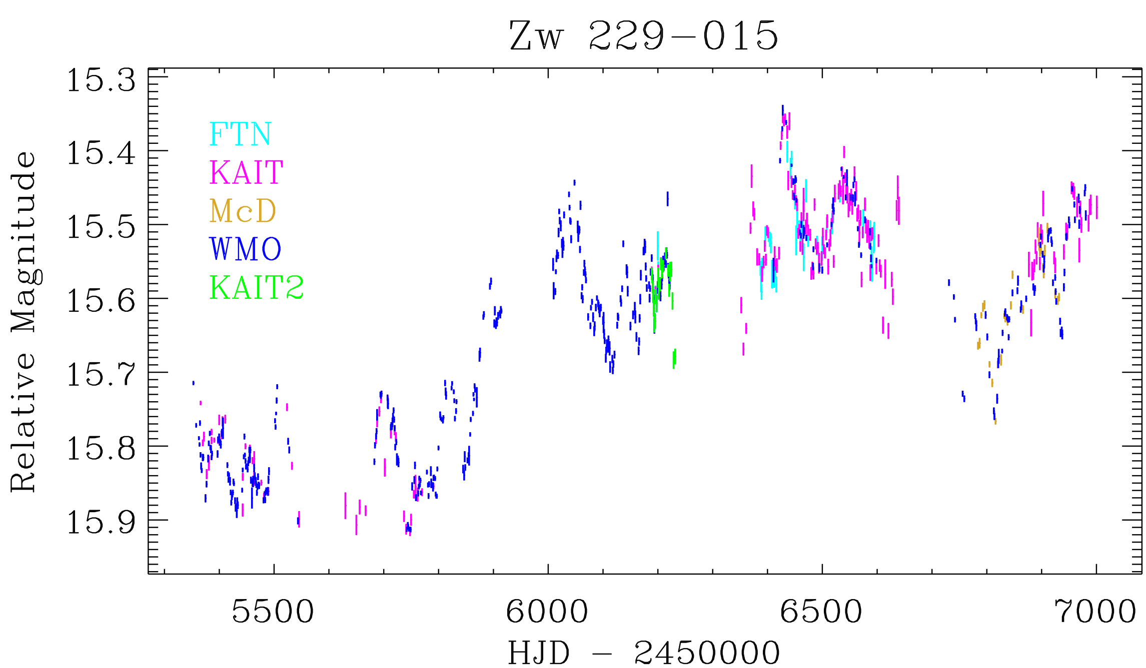

Figure A.3: V-band light curve of Zw 229-015 constructed using nearly five years of ground-based observations. The WMO dataset was used as an anchor to bring light curves from FTN, McDonald, and the two KAIT detectors to the same magnitude scale.

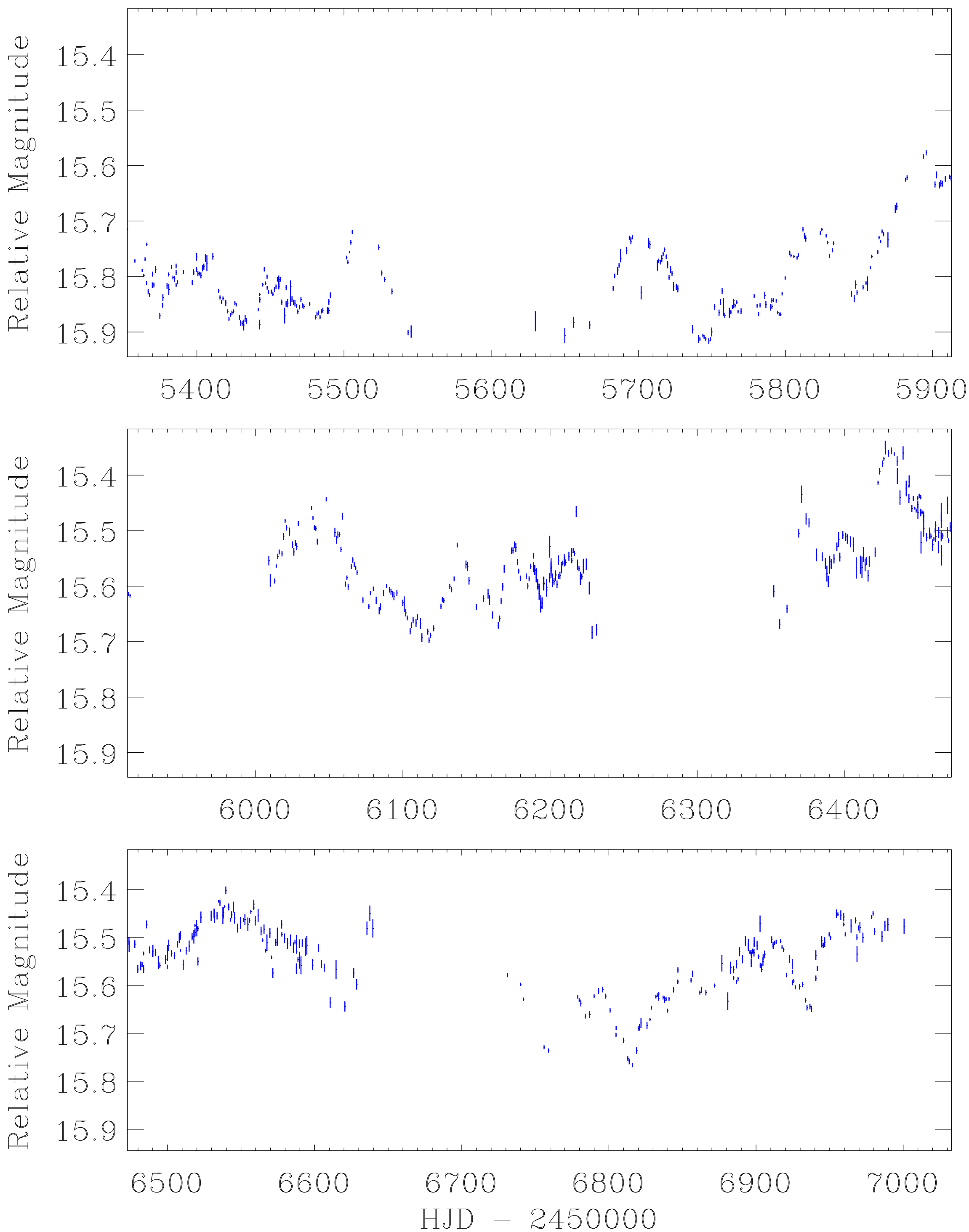

Figure A.4: Five-year Zw 229-015 light curve expanded to show short-term variability.

Appendix B

Light Curve Tables from Reverberation Mapping Data

Table B.1: Photometry measurements for KA1858+4850. The telescopes are listed as follows: N = Nickel, M = MLO, F = FTN, K = KAIT, W = WMO. (Full version of Table 2.2.)

UT Date	Telescope	HJD − 2450000	V (mag)
2012-01-31	N	5957.754	17.129 ± 0.008
2012-02-11	M	5969.014	17.012 ± 0.015
2012-02-17	N	5974.663	17.055 ± 0.015
2012-02-20	F	5978.153	17.011 ± 0.014
2012-02-22	F	5980.166	17.037 ± 0.020
2012-02-23	K	5981.038	17.030 ± 0.025
2012-02-24	K	5982.023	17.055 ± 0.018
2012-02-24	F	5982.115	17.001 ± 0.013
2012-02-25	K	5983.081	17.055 ± 0.048
2012-02-26	N	5983.640	17.016 ± 0.016

Continued on next page

Table B.1 – continued from previous page

UT Date	Telescope	HJD − 2450000	V (mag)
2012-02-26	K	5984.075	17.059 ± 0.034
2012-02-26	F	5984.143	17.030 ± 0.014
2012-02-28	F	5986.092	17.031 ± 0.016
2012-03-03	K	5990.029	17.014 ± 0.016
2012-03-05	M	5992.005	17.051 ± 0.025
2012-03-05	K	5992.020	17.073 ± 0.020
2012-03-08	K	5995.002	17.018 ± 0.038
2012-03-09	K	5996.014	16.970 ± 0.029
2012-03-10	K	5997.060	17.027 ± 0.027
2012-03-13	M	6000.016	16.946 ± 0.015
2012-03-15	F	6002.127	16.963 ± 0.015
2012-03-17	F	6004.144	16.977 ± 0.015
2012-03-19	F	6006.096	16.983 ± 0.013
2012-03-21	K	6008.056	16.986 ± 0.036
2012-03-22	W	6008.931	17.010 ± 0.009
2012-03-26	W	6012.891	17.046 ± 0.005
2012-03-27	W	6013.913	17.013 ± 0.005
2012-03-28	W	6014.948	16.996 ± 0.007
2012-03-29	W	6015.892	17.005 ± 0.006
2012-03-29	F	6016.140	17.005 ± 0.016
2012-03-31	W	6017.846	17.016 ± 0.008
2012-03-31	M	6017.989	17.000 ± 0.015
2012-04-01	W	6018.833	17.010 ± 0.009
2012-04-02	W	6019.957	17.014 ± 0.006

Continued on next page

Table B.1 – continued from previous page

UT Date	Telescope	HJD − 2450000	V (mag)
2012-04-03	N	6020.649	16.982 ± 0.027
2012-04-03	W	6020.952	17.015 ± 0.006
2012-04-05	W	6022.870	17.008 ± 0.013
2012-04-07	W	6024.960	17.010 ± 0.009
2012-04-07	K	6025.020	17.010 ± 0.028
2012-04-08	W	6025.882	16.984 ± 0.011
2012-04-08	K	6026.014	17.000 ± 0.029
2012-04-09	W	6026.966	17.003 ± 0.007
2012-04-10	W	6027.874	17.012 ± 0.015
2012-04-11	W	6028.926	17.000 ± 0.007
2012-04-19	N	6036.633	17.074 ± 0.005
2012-04-20	W	6037.904	17.064 ± 0.006
2012-04-20	K	6038.011	17.053 ± 0.022
2012-04-21	W	6038.883	17.057 ± 0.007
2012-04-21	K	6038.994	17.053 ± 0.017
2012-04-21	F	6039.070	17.058 ± 0.012
2012-04-22	W	6039.832	17.057 ± 0.007
2012-04-22	F	6040.099	17.035 ± 0.016
2012-04-23	N	6040.730	17.043 ± 0.017
2012-04-23	W	6040.804	17.038 ± 0.007
2012-04-23	M	6040.975	17.041 ± 0.015
2012-04-24	W	6041.812	17.040 ± 0.008
2012-04-24	F	6042.118	17.032 ± 0.012
2012-04-27	K	6045.010	17.046 ± 0.028

Continued on next page

Table B.1 – continued from previous page

UT Date	Telescope	HJD − 2450000	V (mag)
2012-04-27	F	6045.127	17.013 ± 0.017
2012-04-28	K	6045.986	17.098 ± 0.017
2012-04-29	K	6047.001	17.024 ± 0.026
2012-04-29	M	6047.008	17.046 ± 0.029
2012-04-30	W	6047.895	17.081 ± 0.006
2012-04-30	K	6048.009	17.071 ± 0.040
2012-05-01	N	6048.678	17.078 ± 0.007
2012-05-01	K	6048.996	17.076 ± 0.018
2012-05-02	K	6049.984	17.061 ± 0.024
2012-05-03	K	6050.998	17.082 ± 0.018
2012-05-05	K	6052.951	17.130 ± 0.036
2012-05-06	W	6053.796	17.125 ± 0.017
2012-05-06	K	6053.971	17.206 ± 0.037
2012-05-07	W	6054.815	17.179 ± 0.014
2012-05-07	K	6054.946	17.177 ± 0.028
2012-05-08	N	6055.597	17.232 ± 0.010
2012-05-08	W	6055.819	17.161 ± 0.012
2012-05-09	W	6056.914	17.201 ± 0.009
2012-05-09	K	6056.967	17.165 ± 0.023
2012-05-10	W	6057.910	17.212 ± 0.009
2012-05-10	K	6057.960	17.210 ± 0.022
2012-05-11	K	6058.936	17.137 ± 0.021
2012-05-12	N	6059.666	17.173 ± 0.006
2012-05-12	M	6059.901	17.150 ± 0.016

Continued on next page

Table B.1 – continued from previous page

UT Date	Telescope	HJD − 2450000	V (mag)
2012-05-12	K	6059.993	17.220 ± 0.029
2012-05-13	W	6060.891	17.163 ± 0.008
2012-05-13	K	6060.994	17.262 ± 0.029
2012-05-14	W	6061.931	17.159 ± 0.007
2012-05-15	W	6062.808	17.141 ± 0.010
2012-05-15	K	6062.977	17.218 ± 0.024
2012-05-16	K	6063.979	17.153 ± 0.018
2012-05-17	W	6064.913	17.160 ± 0.007
2012-05-17	F	6065.112	17.147 ± 0.014
2012-05-18	W	6065.931	17.169 ± 0.008
2012-05-18	F	6066.105	17.150 ± 0.012
2012-05-19	N	6066.669	17.198 ± 0.007
2012-05-19	W	6066.932	17.164 ± 0.007
2012-05-19	K	6066.961	17.136 ± 0.018
2012-05-19	F	6067.099	17.176 ± 0.012
2012-05-20	W	6067.917	17.161 ± 0.006
2012-05-20	K	6067.940	17.166 ± 0.017
2012-05-20	F	6067.965	17.176 ± 0.012
2012-05-21	W	6068.828	17.173 ± 0.007
2012-05-21	K	6068.959	17.117 ± 0.021
2012-05-21	F	6068.962	17.168 ± 0.012
2012-05-22	K	6069.977	17.155 ± 0.020
2012-05-23	N	6070.605	17.157 ± 0.008
2012-05-23	K	6070.905	17.168 ± 0.021

Continued on next page

Table B.1 – continued from previous page

UT Date	Telescope	HJD − 2450000	V (mag)
2012-05-23	F	6071.005	17.158 ± 0.012
2012-05-24	K	6071.951	17.176 ± 0.018
2012-05-25	W	6072.847	17.183 ± 0.008
2012-05-27	K	6074.948	17.210 ± 0.016
2012-05-28	K	6075.933	17.215 ± 0.018
2012-05-29	W	6076.873	17.185 ± 0.007
2012-05-29	K	6076.922	17.209 ± 0.018
2012-05-31	W	6077.934	17.173 ± 0.007
2012-05-30	K	6077.963	17.167 ± 0.017
2012-05-30	F	6078.011	17.151 ± 0.020
2012-05-31	N	6078.626	17.160 ± 0.006
2012-05-31	K	6078.970	17.147 ± 0.017
2012-06-01	W	6079.918	17.132 ± 0.006
2012-06-01	K	6079.970	17.158 ± 0.017
2012-06-03	W	6081.852	17.101 ± 0.011
2012-06-03	K	6081.963	17.139 ± 0.030
2012-06-05	W	6083.880	17.085 ± 0.011
2012-06-06	W	6084.752	17.066 ± 0.012
2012-06-06	K	6084.953	17.068 ± 0.022
2012-06-07	N	6085.555	17.095 ± 0.007
2012-06-07	K	6085.963	17.071 ± 0.020
2012-06-08	W	6086.818	17.066 ± 0.010
2012-06-08	K	6086.976	17.093 ± 0.027
2012-06-08	F	6087.074	17.030 ± 0.015

Continued on next page

Table B.1 – continued from previous page

UT Date	Telescope	HJD − 2450000	V (mag)
2012-06-09	M	6087.916	17.066 ± 0.015
2012-06-09	K	6087.936	17.071 ± 0.021
2012-06-10	W	6088.844	17.046 ± 0.006
2012-06-10	F	6089.100	17.035 ± 0.013
2012-06-11	W	6089.857	17.021 ± 0.006
2012-06-11	K	6089.906	17.002 ± 0.015
2012-06-12	N	6090.636	17.017 ± 0.006
2012-06-12	K	6090.916	17.011 ± 0.015
2012-06-12	W	6090.945	17.006 ± 0.009
2012-06-13	F	6091.883	17.008 ± 0.012
2012-06-13	K	6091.913	17.000 ± 0.015
2012-06-13	W	6091.939	17.007 ± 0.007
2012-06-14	N	6092.628	16.998 ± 0.007
2012-06-14	K	6092.890	16.988 ± 0.014
2012-06-14	W	6092.939	16.983 ± 0.008
2012-06-15	K	6093.884	16.959 ± 0.016
2012-06-15	W	6093.946	17.003 ± 0.013
2012-06-16	K	6094.878	16.972 ± 0.016
2012-06-16	F	6095.073	16.967 ± 0.011
2012-06-17	W	6095.934	17.000 ± 0.007
2012-06-18	K	6096.889	16.964 ± 0.014
2012-06-18	M	6096.899	16.994 ± 0.014
2012-06-19	N	6097.667	16.989 ± 0.007
2012-06-19	M	6097.906	16.966 ± 0.014

Continued on next page

Table B.1 – continued from previous page

UT Date	Telescope	HJD − 2450000	V (mag)
2012-06-20	K	6098.863	16.966 ± 0.014
2012-06-21	K	6099.909	16.941 ± 0.014
2012-06-21	W	6099.941	16.959 ± 0.007
2012-06-22	N	6100.643	16.954 ± 0.007
2012-06-22	W	6100.938	16.951 ± 0.018
2012-06-23	W	6101.943	16.958 ± 0.008
2012-06-24	K	6102.874	16.937 ± 0.016
2012-06-24	M	6102.917	16.924 ± 0.014
2012-06-24	W	6102.920	16.944 ± 0.006
2012-06-25	K	6103.854	16.931 ± 0.016
2012-06-25	M	6103.898	16.928 ± 0.014
2012-06-26	M	6104.872	16.931 ± 0.014
2012-06-26	W	6104.941	16.938 ± 0.007
2012-06-27	W	6105.728	16.932 ± 0.008
2012-06-27	M	6105.893	16.921 ± 0.014
2012-06-27	K	6105.898	16.957 ± 0.015
2012-06-28	K	6106.874	16.932 ± 0.014
2012-06-28	W	6106.940	16.930 ± 0.007
2012-06-29	N	6107.554	16.954 ± 0.007
2012-06-29	M	6107.910	16.940 ± 0.014
2012-06-29	K	6107.912	16.926 ± 0.013
2012-06-30	W	6108.946	16.945 ± 0.008
2012-07-01	W	6109.841	16.940 ± 0.008
2012-07-02	K	6110.824	16.930 ± 0.021

Continued on next page

Table B.1 – continued from previous page

UT Date	Telescope	HJD − 2450000	V (mag)
2012-07-03	N	6111.526	16.959 ± 0.013
2012-07-03	W	6111.891	16.948 ± 0.012
2012-07-05	K	6113.877	16.983 ± 0.021
2012-07-06	K	6114.843	16.920 ± 0.020
2012-07-07	N	6115.610	16.935 ± 0.008
2012-07-07	M	6115.831	16.931 ± 0.014
2012-07-07	K	6115.853	16.921 ± 0.017
2012-07-08	K	6116.850	16.953 ± 0.017
2012-07-08	W	6116.889	16.948 ± 0.007
2012-07-09	W	6117.768	16.932 ± 0.007
2012-07-09	K	6117.850	16.959 ± 0.015
2012-07-10	W	6118.813	16.921 ± 0.006
2012-07-10	K	6118.828	16.918 ± 0.014
2012-07-11	K	6119.832	16.926 ± 0.014
2012-07-12	K	6120.826	16.991 ± 0.020
2012-07-12	W	6120.898	16.965 ± 0.007
2012-07-13	K	6121.828	16.984 ± 0.014
2012-07-14	K	6122.838	16.953 ± 0.013
2012-07-15	K	6123.842	16.977 ± 0.014
2012-07-16	K	6124.819	16.949 ± 0.014
2012-07-17	K	6125.834	16.988 ± 0.014
2012-07-17	W	6125.859	16.973 ± 0.007
2012-07-18	W	6126.793	16.971 ± 0.007
2012-07-19	W	6127.790	16.961 ± 0.006

Continued on next page

Table B.1 – continued from previous page

UT Date	Telescope	HJD − 2450000	V (mag)
2012-07-20	K	6128.869	16.975 ± 0.014
2012-07-20	F	6128.889	16.977 ± 0.011
2012-07-21	K	6129.807	16.980 ± 0.015
2012-07-21	M	6129.819	16.951 ± 0.014
2012-07-22	K	6130.809	16.964 ± 0.014
2012-07-22	F	6130.827	16.962 ± 0.011
2012-07-23	K	6131.817	16.929 ± 0.022
2012-07-23	W	6131.881	16.938 ± 0.007
2012-07-23	F	6131.882	16.940 ± 0.011
2012-07-23	N	6131.924	16.931 ± 0.007
2012-07-24	F	6132.880	16.943 ± 0.011
2012-07-24	W	6132.937	16.934 ± 0.007
2012-07-25	F	6133.764	16.929 ± 0.012
2012-07-25	K	6133.797	16.935 ± 0.014
2012-07-26	K	6134.818	16.931 ± 0.014
2012-07-26	W	6134.821	16.928 ± 0.006
2012-07-26	F	6134.845	16.929 ± 0.012
2012-07-27	N	6135.750	16.942 ± 0.007
2012-07-27	K	6135.783	16.911 ± 0.014
2012-07-27	F	6135.797	16.931 ± 0.013
2012-07-28	K	6136.785	16.923 ± 0.015
2012-07-28	F	6136.841	16.929 ± 0.014
2012-07-28	W	6136.923	16.917 ± 0.007
2012-07-29	F	6137.891	16.900 ± 0.014

Continued on next page

Table B.1 – continued from previous page

UT Date	Telescope	HJD − 2450000	V (mag)
2012-07-30	F	6138.959	16.927 ± 0.017
2012-07-31	N	6139.786	16.902 ± 0.007
2012-08-01	K	6140.795	16.954 ± 0.021
2012-08-01	F	6140.918	16.880 ± 0.023
2012-08-02	F	6141.866	16.842 ± 0.022
2012-08-03	F	6142.747	16.885 ± 0.019
2012-08-03	K	6142.846	16.913 ± 0.022
2012-08-03	W	6142.877	16.858 ± 0.010
2012-08-04	F	6143.915	16.881 ± 0.017
2012-08-04	W	6143.928	16.881 ± 0.012
2012-08-05	K	6144.782	16.899 ± 0.017
2012-08-05	W	6144.925	16.915 ± 0.010
2012-08-05	F	6144.927	16.934 ± 0.017
2012-08-06	F	6145.753	16.936 ± 0.012
2012-08-06	K	6145.790	16.956 ± 0.021
2012-08-07	N	6146.776	16.924 ± 0.006
2012-08-07	F	6146.854	16.925 ± 0.012
2012-08-08	K	6147.836	16.952 ± 0.016
2012-08-08	F	6147.976	16.909 ± 0.014
2012-08-09	F	6148.744	16.897 ± 0.014
2012-08-09	M	6148.758	16.882 ± 0.014
2012-08-09	K	6148.781	16.880 ± 0.015
2012-08-10	F	6149.751	16.910 ± 0.011
2012-08-10	N	6149.849	16.888 ± 0.006

Continued on next page

Table B.1 – continued from previous page

UT Date	Telescope	HJD − 2450000	V (mag)
2012-08-10	W	6149.914	16.900 ± 0.008
2012-08-11	F	6150.743	16.903 ± 0.015
2012-08-11	M	6150.854	16.852 ± 0.022
2012-08-12	K	6151.750	16.901 ± 0.015
2012-08-12	F	6151.795	16.882 ± 0.011
2012-08-14	F	6153.751	16.950 ± 0.012
2012-08-14	K	6153.753	16.931 ± 0.015
2012-08-15	F	6154.740	16.916 ± 0.019
2012-08-15	N	6154.750	16.917 ± 0.007
2012-08-15	W	6154.752	16.918 ± 0.008
2012-08-15	K	6154.754	16.904 ± 0.015
2012-08-16	K	6155.722	16.911 ± 0.014
2012-08-17	M	6156.667	16.928 ± 0.016
2012-08-17	K	6156.736	16.919 ± 0.021
2012-08-17	N	6156.790	16.915 ± 0.006
2012-08-18	W	6157.889	16.956 ± 0.012
2012-08-19	N	6158.779	16.951 ± 0.007
2012-08-19	W	6158.870	16.964 ± 0.012
2012-08-20	K	6159.723	16.918 ± 0.014
2012-08-21	K	6160.730	16.951 ± 0.014
2012-08-21	W	6160.860	16.942 ± 0.008
2012-08-23	K	6162.730	16.917 ± 0.015
2012-08-24	K	6163.712	16.909 ± 0.015
2012-08-25	K	6164.720	16.859 ± 0.020

Continued on next page

Table B.1 – continued from previous page

UT Date	Telescope	HJD − 2450000	V (mag)
2012-08-25	W	6164.812	16.908 ± 0.007
2012-08-26	W	6165.755	16.898 ± 0.008
2012-08-27	M	6166.661	16.904 ± 0.015
2012-08-27	K	6166.710	16.872 ± 0.016
2012-08-27	W	6166.770	16.902 ± 0.008
2012-08-28	K	6167.712	16.882 ± 0.018
2012-08-28	N	6167.734	16.895 ± 0.008
2012-08-28	W	6167.860	16.919 ± 0.010
2012-08-29	W	6168.856	16.921 ± 0.011
2012-08-30	K	6169.714	16.922 ± 0.022
2012-08-31	K	6170.738	16.919 ± 0.021
2012-08-31	N	6170.767	16.914 ± 0.009
2012-09-02	K	6172.762	16.916 ± 0.021
2012-09-03	K	6173.702	16.937 ± 0.019
2012-09-03	W	6173.826	16.922 ± 0.009
2012-09-04	K	6174.726	16.913 ± 0.017
2012-09-04	W	6174.816	16.907 ± 0.008
2012-09-05	N	6175.792	16.901 ± 0.008
2012-09-05	W	6175.852	16.882 ± 0.009
2012-09-06	W	6176.762	16.891 ± 0.022
2012-09-07	W	6177.829	16.881 ± 0.008
2012-09-08	W	6178.682	16.893 ± 0.008
2012-09-08	K	6178.684	16.861 ± 0.014
2012-09-08	W	6178.685	16.895 ± 0.008

Continued on next page

Table B.1 – continued from previous page

UT Date	Telescope	HJD − 2450000	V (mag)
2012-09-08	N	6178.814	16.894 ± 0.008
2012-09-09	K	6179.690	16.895 ± 0.015
2012-09-09	W	6179.798	16.882 ± 0.007
2012-09-10	K	6180.675	16.921 ± 0.015
2012-09-10	N	6180.829	16.896 ± 0.006
2012-09-10	F	6181.727	16.896 ± 0.020
2012-09-13	W	6183.849	16.907 ± 0.007
2012-09-14	W	6184.873	16.903 ± 0.008
2012-09-15	M	6185.701	16.889 ± 0.014
2012-09-15	W	6185.773	16.876 ± 0.007
2012-09-16	W	6186.803	16.885 ± 0.007
2012-09-16	F	6187.723	16.911 ± 0.013
2012-09-18	M	6188.693	16.928 ± 0.014
2012-09-18	N	6188.831	16.921 ± 0.009
2012-09-18	W	6188.856	16.916 ± 0.008
2012-09-19	W	6189.785	16.916 ± 0.006
2012-09-20	W	6190.770	16.931 ± 0.007
2012-09-21	N	6191.670	16.935 ± 0.006
2012-09-20	F	6191.721	16.924 ± 0.015
2012-09-21	W	6191.789	16.966 ± 0.008
2012-09-22	W	6192.788	16.941 ± 0.008
2012-09-23	W	6193.726	16.909 ± 0.016
2012-09-22	F	6193.816	16.893 ± 0.015
2012-09-24	F	6195.767	16.874 ± 0.016

Continued on next page

Table B.1 – continued from previous page

UT Date	Telescope	HJD − 2450000	V (mag)
2012-09-26	N	6196.676	16.898 ± 0.013
2012-09-26	F	6197.718	16.916 ± 0.020
2012-09-29	W	6199.706	16.871 ± 0.012
2012-09-28	F	6199.775	16.812 ± 0.024
2012-09-29	F	6200.723	16.927 ± 0.023
2012-10-01	W	6201.672	16.845 ± 0.009
2012-10-02	W	6202.718	16.857 ± 0.009
2012-10-03	N	6203.671	16.824 ± 0.008
2012-10-03	W	6203.758	16.809 ± 0.009
2012-10-04	W	6204.758	16.826 ± 0.011
2012-10-05	W	6205.629	16.778 ± 0.007
2012-10-06	W	6206.704	16.840 ± 0.007
2012-10-07	N	6207.669	16.801 ± 0.007
2012-10-07	W	6207.702	16.820 ± 0.006
2012-10-08	W	6208.604	16.821 ± 0.008
2012-10-09	W	6209.634	16.817 ± 0.006
2012-10-10	W	6210.635	16.790 ± 0.012
2012-10-11	M	6211.630	16.850 ± 0.015
2012-10-11	N	6211.637	16.841 ± 0.008
2012-10-10	F	6211.722	16.834 ± 0.010
2012-10-12	W	6212.799	16.848 ± 0.009
2012-10-14	M	6214.627	16.896 ± 0.014
2012-10-14	W	6214.755	16.865 ± 0.007
2012-10-14	F	6215.717	16.893 ± 0.011

Continued on next page

Table B.1 – continued from previous page

UT Date	Telescope	HJD − 2450000	V (mag)
2012-10-15	W	6215.728	16.902 ± 0.007
2012-10-16	W	6216.663	16.928 ± 0.007
2012-10-16	F	6217.716	16.960 ± 0.011
2012-10-17	W	6217.802	16.953 ± 0.014
2012-10-18	W	6218.667	16.968 ± 0.007
2012-10-19	N	6219.607	17.012 ± 0.008
2012-10-19	W	6219.687	16.982 ± 0.007
2012-10-18	F	6219.716	16.995 ± 0.011
2012-10-20	W	6220.644	16.978 ± 0.011
2012-10-21	W	6221.613	16.976 ± 0.008
2012-10-20	F	6221.739	17.004 ± 0.012
2012-10-22	N	6222.614	16.977 ± 0.024
2012-10-24	N	6224.599	16.973 ± 0.008
2012-10-25	M	6225.737	16.980 ± 0.018
2012-10-28	F	6229.716	16.958 ± 0.018
2012-10-30	N	6230.631	16.948 ± 0.011
2012-11-03	N	6234.642	16.909 ± 0.008
2012-11-04	W	6235.579	16.920 ± 0.008
2012-11-04	M	6235.579	16.917 ± 0.015
2012-11-04	W	6235.584	16.901 ± 0.006
2012-11-03	F	6235.722	16.898 ± 0.011
2012-11-05	N	6236.588	16.921 ± 0.008
2012-11-05	W	6236.638	16.909 ± 0.006
2012-11-05	F	6237.721	16.931 ± 0.011

Continued on next page

Table B.1 – continued from previous page

UT Date	Telescope	HJD − 2450000	V (mag)
2012-11-08	N	6239.620	16.931 ± 0.007
2012-11-08	W	6239.635	16.934 ± 0.005
2012-11-09	F	6241.719	16.940 ± 0.011
2012-11-11	F	6243.716	16.928 ± 0.011
2012-11-14	N	6245.651	16.902 ± 0.009
2012-11-15	F	6247.777	16.898 ± 0.015

Table B.2: Spectroscopic Measurements for KA1858+4850. Listed SNR is the signal-to-noise ratio per pixel for the observed wavelength range 4500–4600 Å in the AGN spectra. Measured fluxes include the blended broad and narrow emission lines. (Full version of Table 2.4.)

UT Date	HJD−2450000	SNR	f(Hβ)	f(Hγ)	f(Hδ)	f(He II)
				(10^{-15} erg s^{-1} cm^{-2})		
2012-02-16	5974.087	11	42.87 ± 0.38	19.12 ± 0.51	8.27 ± 0.54	11.60 ± 0.47
2012-03-04	5991.073	35	40.90 ± 0.14	18.37 ± 0.14	9.84 ± 0.14	7.30 ± 0.14
2012-04-02	6020.024	19	42.42 ± 0.30	19.30 ± 0.27	12.24 ± 0.27	9.68 ± 0.28
2012-04-16	6033.929	21	45.20 ± 0.28	22.75 ± 0.26	13.73 ± 0.26	10.20 ± 0.27
2012-04-16	6034.975	34	46.41 ± 0.19	22.53 ± 0.16	13.15 ± 0.16	8.04 ± 0.16
2012-04-20	6036.930	24	42.77 ± 0.22	21.05 ± 0.23	11.19 ± 0.25	7.72 ± 0.22
2012-04-24	6041.013	22	44.66 ± 0.29	20.27 ± 0.24	10.99 ± 0.24	9.29 ± 0.25
2012-04-28	6046.026	11	45.42 ± 0.36	20.86 ± 0.43	11.14 ± 0.45	10.26 ± 0.39
2012-05-00	6048.942	21	44.91 ± 0.24	22.80 ± 0.27	12.31 ± 0.29	9.62 ± 0.25
2012-05-18	6065.967	30	41.41 ± 0.17	18.68 ± 0.15	10.41 ± 0.15	5.35 ± 0.16
2012-05-20	6066.952	29	41.92 ± 0.20	18.94 ± 0.16	10.63 ± 0.16	5.80 ± 0.16
2012-05-20	6068.009	19	42.87 ± 0.22	18.80 ± 0.23	12.37 ± 0.25	6.24 ± 0.22
2012-05-20	6068.989	28	41.91 ± 0.20	18.57 ± 0.16	10.20 ± 0.16	5.32 ± 0.16
2012-05-28	6075.973	24	40.17 ± 0.22	18.03 ± 0.18	9.75 ± 0.18	5.24 ± 0.19

Continued on next page

Table B.2 – continued from previous page

UT Date	HJD−2450000	SNR	$f(\mathrm{H}\beta)$	$f(\mathrm{H}\gamma)$	$f(\mathrm{H}\delta)$	$f(\text{He II})$
				(10^{-15} erg s^{-1} cm^{-2})		
2012-05-28	6076.996	25	38.62 ± 0.18	17.03 ± 0.17	9.21 ± 0.17	4.50 ± 0.16
2012-06-12	6091.860	29	42.96 ± 0.24	20.98 ± 0.20	12.56 ± 0.20	9.46 ± 0.22
2012-06-14	6092.962	37	40.43 ± 0.18	19.64 ± 0.15	12.38 ± 0.15	10.28 ± 0.15
2012-06-18	6096.997	20	41.71 ± 0.26	21.68 ± 0.27	12.02 ± 0.28	7.07 ± 0.26
2012-06-20	6097.874	27	42.47 ± 0.26	20.27 ± 0.21	12.02 ± 0.21	8.69 ± 0.23
2012-06-20	6098.803	25	41.77 ± 0.28	20.12 ± 0.24	12.45 ± 0.24	8.62 ± 0.25
2012-06-20	6099.834	40	44.78 ± 0.19	21.28 ± 0.15	13.12 ± 0.14	10.46 ± 0.15
2012-06-22	6100.819	31	45.85 ± 0.24	20.97 ± 0.19	12.46 ± 0.18	10.81 ± 0.21
2012-06-24	6101.787	21	43.50 ± 0.32	19.08 ± 0.25	10.88 ± 0.25	10.33 ± 0.27
2012-06-24	6102.795	14	41.70 ± 0.42	19.48 ± 0.39	10.93 ± 0.41	9.95 ± 0.43
2012-06-24	6103.799	30	43.43 ± 0.23	20.65 ± 0.19	12.44 ± 0.19	11.67 ± 0.20
2012-06-28	6105.997	23	45.63 ± 0.26	21.80 ± 0.26	12.92 ± 0.27	12.85 ± 0.26
2012-07-12	6119.922	37	47.95 ± 0.19	23.41 ± 0.16	13.80 ± 0.16	11.64 ± 0.16
2012-07-12	6120.926	35	48.08 ± 0.20	21.88 ± 0.16	13.04 ± 0.16	10.52 ± 0.17
2012-07-12	6121.926	35	50.14 ± 0.18	23.78 ± 0.17	13.95 ± 0.16	10.32 ± 0.18

Continued on next page

Table B.2 – continued from previous page

UT Date	HJD−2450000	SNR	$f(\mathrm{H}\beta)$	$f(\mathrm{H}\gamma)$	$f(\mathrm{H}\delta)$	$f(\mathrm{He\ II})$
				(10^{-15} erg s^{-1} cm^{-2})		
2012-07-14	6122.901	36	48.22 ± 0.18	22.74 ± 0.16	12.70 ± 0.16	9.46 ± 0.17
2012-07-16	6123.884	41	47.62 ± 0.16	22.82 ± 0.14	13.09 ± 0.14	9.83 ± 0.15
2012-07-16	6124.861	31	48.33 ± 0.21	23.70 ± 0.20	12.51 ± 0.19	9.97 ± 0.21
2012-07-22	6130.966	32	48.09 ± 0.22	22.15 ± 0.18	12.98 ± 0.18	8.01 ± 0.19
2012-07-24	6132.011	16	49.45 ± 0.34	22.79 ± 0.38	12.97 ± 0.41	8.45 ± 0.36
2012-08-08	6148.812	40	50.96 ± 0.20	23.61 ± 0.16	14.06 ± 0.15	9.41 ± 0.16
2012-08-10	6149.692	31	52.55 ± 0.25	23.23 ± 0.20	14.29 ± 0.20	9.63 ± 0.21
2012-08-12	6150.702	25	53.58 ± 0.33	22.46 ± 0.24	13.81 ± 0.23	10.26 ± 0.25
2012-08-12	6151.694	15	53.09 ± 0.54	23.86 ± 0.48	15.52 ± 0.49	10.97 ± 0.52
2012-08-12	6152.743	25	48.26 ± 0.30	22.33 ± 0.25	12.41 ± 0.25	11.82 ± 0.27
2012-08-14	6153.900	32	48.71 ± 0.23	23.21 ± 0.20	13.26 ± 0.20	10.93 ± 0.20
2012-08-16	6154.752	25	46.41 ± 0.29	21.36 ± 0.24	12.85 ± 0.24	8.30 ± 0.26
2012-08-16	6155.761	29	49.82 ± 0.26	23.68 ± 0.21	14.34 ± 0.21	11.27 ± 0.23
2012-08-16	6156.780	29	50.14 ± 0.27	22.44 ± 0.22	13.48 ± 0.21	8.92 ± 0.23
2012-08-20	6158.748	24	52.18 ± 0.31	23.34 ± 0.26	13.90 ± 0.26	10.45 ± 0.27

Continued on next page

Table B.2 – continued from previous page

UT Date	HJD−2450000	SNR	f(Hβ)	f(Hγ)	f(Hδ)	f(He II)
				(10^{-15} erg s^{-1} cm^{-2})		
2012-08-20	6159.741	42	49.87 ± 0.18	22.64 ± 0.14	13.46 ± 0.13	9.24 ± 0.14
2012-08-20	6160.709	26	48.46 ± 0.29	23.16 ± 0.24	13.13 ± 0.24	9.88 ± 0.26
2012-08-22	6161.768	45	50.07 ± 0.17	22.59 ± 0.14	13.46 ± 0.13	10.48 ± 0.14
2012-08-24	6162.665	34	48.28 ± 0.19	21.14 ± 0.16	13.43 ± 0.16	9.16 ± 0.16
2012-08-24	6163.764	25	49.66 ± 0.33	23.50 ± 0.27	13.75 ± 0.27	10.79 ± 0.29
2012-09-08	6178.650	41	49.05 ± 0.17	23.04 ± 0.15	13.60 ± 0.14	11.64 ± 0.15
2012-09-08	6179.656	25	48.20 ± 0.30	22.63 ± 0.25	13.44 ± 0.25	12.23 ± 0.28
2012-09-10	6180.645	37	49.68 ± 0.19	22.50 ± 0.16	13.64 ± 0.16	11.88 ± 0.16
2012-09-20	6191.652	17	49.19 ± 0.47	25.92 ± 0.43	18.09 ± 0.44	8.05 ± 0.47
2012-09-22	6192.645	28	50.64 ± 0.25	23.53 ± 0.20	12.28 ± 0.20	8.43 ± 0.22
2012-09-24	6193.635	40	49.15 ± 0.18	22.57 ± 0.14	12.84 ± 0.14	8.42 ± 0.15
2012-09-24	6194.681	24	50.56 ± 0.30	22.99 ± 0.25	12.66 ± 0.25	9.67 ± 0.27
2012-09-24	6195.644	26	51.10 ± 0.27	24.06 ± 0.24	14.53 ± 0.25	11.39 ± 0.25
2012-09-26	6196.669	22	52.71 ± 0.31	24.03 ± 0.28	13.76 ± 0.29	11.76 ± 0.30
2012-10-04	6205.624	20	54.53 ± 0.40	25.20 ± 0.37	15.08 ± 0.38	15.93 ± 0.41

Continued on next page

Table B.2 – continued from previous page

UT Date	HJD−2450000	SNR	$f(\mathrm{H}\beta)$	$f(\mathrm{H}\gamma)$	$f(\mathrm{H}\delta)$	$f(\mathrm{He\ II})$
				(10^{-15} erg s^{-1} cm^{-2})		
2012-10-08	6207.614	33	49.24 ± 0.21	23.38 ± 0.19	13.54 ± 0.19	11.70 ± 0.20
2012-10-08	6209.677	35	50.45 ± 0.22	23.90 ± 0.19	14.09 ± 0.19	12.60 ± 0.20
2012-10-14	6214.632	40	53.15 ± 0.20	24.22 ± 0.16	14.84 ± 0.16	11.97 ± 0.17
2012-10-20	6219.612	23	50.78 ± 0.29	23.19 ± 0.24	13.26 ± 0.24	5.01 ± 0.26
2012-10-20	6220.608	26	50.61 ± 0.26	23.50 ± 0.22	13.81 ± 0.22	4.77 ± 0.22
2012-10-20	6221.604	18	49.48 ± 0.32	23.25 ± 0.30	13.38 ± 0.31	6.56 ± 0.31
2012-11-04	6235.654	25	47.80 ± 0.29	22.24 ± 0.25	12.41 ± 0.26	14.04 ± 0.28
2012-11-04	6236.619	31	48.85 ± 0.23	22.88 ± 0.20	13.31 ± 0.20	13.49 ± 0.21
2012-11-06	6237.597	25	49.82 ± 0.29	22.92 ± 0.25	13.10 ± 0.25	13.81 ± 0.27
2012-11-08	6238.626	45	50.66 ± 0.16	21.61 ± 0.13	12.76 ± 0.13	11.68 ± 0.14
2012-11-08	6239.624	44	50.01 ± 0.17	22.94 ± 0.14	13.96 ± 0.14	10.66 ± 0.15
2012-11-12	6243.660	18	51.57 ± 0.42	25.19 ± 0.39	15.64 ± 0.40	13.24 ± 0.43
2012-11-14	6245.588	29	47.02 ± 0.22	22.45 ± 0.20	12.71 ± 0.20	12.87 ± 0.21
2012-11-16	6246.618	28	50.31 ± 0.25	23.39 ± 0.21	13.52 ± 0.21	14.94 ± 0.24
2012-11-20	6251.581	16	51.11 ± 0.36	23.55 ± 0.36	12.91 ± 0.38	15.09 ± 0.39

Table B.3: NGC 5548 continuum and emission-line flux measurements. All emission-line fluxes include contribution from both broad and narrow line components. (Full version of Table 3.2.)

HJD−2450000	Telescope	f_{5100}[a]	$f_{\mathrm{H}\beta}$[b]	$f_{\mathrm{H}\beta,\ \mathrm{SD}}$[c]	$f_{\mathrm{He\ II},\ \mathrm{SD}}$[d]
6663.00	MDM	10.768 ± 0.054	726.164 ± 3.759	732.158 ± 3.734	22.116 ± 2.666
6663.65	Asiago	10.800 ± 0.057	737.867 ± 4.391	—	—
6664.03	MDM	11.029 ± 0.055	724.274 ± 3.970	729.721 ± 3.946	29.052 ± 3.269
6665.02	MDM	10.639 ± 0.054	714.493 ± 3.697	721.235 ± 3.671	25.510 ± 2.469
6667.02	MDM	10.887 ± 0.056	735.759 ± 4.288	734.996 ± 4.266	37.657 ± 4.080
6668.00	MDM	10.959 ± 0.054	726.749 ± 3.707	729.858 ± 3.681	35.963 ± 2.502
6669.01	MDM	10.867 ± 0.054	727.293 ± 3.695	730.747 ± 3.668	41.501 ± 2.462
6669.65	Asiago	11.057 ± 0.053	722.654 ± 3.535	—	—
6670.02	MDM	10.859 ± 0.055	724.813 ± 3.996	725.673 ± 3.972	44.214 ± 3.348
6670.65	Asiago	10.736 ± 0.054	727.809 ± 3.660	—	—
6671.00	MDM	11.266 ± 0.054	738.781 ± 3.771	730.422 ± 3.746	54.330 ± 2.720
6672.00	MDM	11.100 ± 0.054	731.389 ± 3.747	746.003 ± 3.721	55.723 ± 2.672
6672.61	Asiago	10.722 ± 0.055	740.233 ± 3.798	—	—
6673.00	MDM	11.107 ± 0.054	724.160 ± 3.776	730.383 ± 3.750	52.890 ± 2.787
6674.01	MDM	11.060 ± 0.054	723.311 ± 3.757	719.928 ± 3.732	44.005 ± 2.731

Continued on next page

Table B.3 – continued from previous page

HJD−2450000	Telescope	f_{5100}[a]	$f_{\mathrm{H}\beta}$[b]	$f_{\mathrm{H}\beta,\ \mathrm{SD}}$[c]	$f_{\mathrm{He\ II},\ \mathrm{SD}}$[d]
6675.01	MDM	11.159 ± 0.054	725.535 ± 3.778	731.036 ± 3.753	56.684 ± 2.794
6676.01	MDM	11.269 ± 0.054	723.672 ± 3.778	727.508 ± 3.752	48.232 ± 2.777
6677.00	MDM	11.552 ± 0.058	731.209 ± 4.576	738.676 ± 4.555	67.484 ± 4.885
6678.00	MDM	11.439 ± 0.054	736.854 ± 3.771	743.102 ± 3.745	64.393 ± 2.748
6679.02	MDM	11.294 ± 0.055	732.806 ± 3.936	749.218 ± 3.911	67.309 ± 3.240
6679.63	Asiago	11.254 ± 0.054	729.276 ± 3.774	—	—
6679.98	MDM	11.529 ± 0.054	744.429 ± 3.808	757.013 ± 3.783	74.281 ± 2.881
6681.00	MDM	11.488 ± 0.054	745.811 ± 3.748	761.766 ± 3.722	89.320 ± 2.677
6682.59	Asiago	11.822 ± 0.055	742.361 ± 3.805	—	—
6683.57	Asiago	12.555 ± 0.060	742.114 ± 4.964	—	—
6684.01	MDM	11.721 ± 0.054	753.744 ± 3.744	767.640 ± 3.718	98.627 ± 2.653
6686.04	MDM	11.684 ± 0.054	757.366 ± 3.768	761.169 ± 3.743	88.887 ± 2.752
6686.64	Asiago	11.917 ± 0.054	758.639 ± 3.767	—	—
6687.03	MDM	11.638 ± 0.054	758.135 ± 3.748	757.852 ± 3.723	69.285 ± 2.667
6688.02	MDM	11.374 ± 0.054	749.410 ± 3.735	755.072 ± 3.709	61.377 ± 2.609
6689.01	MDM	11.321 ± 0.069	735.880 ± 6.788	729.055 ± 6.774	47.395 ± 9.032

Continued on next page

Table B.3 – continued from previous page

HJD−2450000	Telescope	f_{5100}[a]	$f_{\mathrm{H}\beta}$[b]	$f_{\mathrm{H}\beta,\ \mathrm{SD}}$[c]	$f_{\mathrm{He\ II},\ \mathrm{SD}}$[d]
6690.98	MDM	11.277 ± 0.054	735.875 ± 3.736	739.916 ± 3.710	50.149 ± 2.604
6693.01	MDM	11.335 ± 0.054	733.770 ± 3.723	736.958 ± 3.697	51.925 ± 2.564
6694.02	MDM	11.496 ± 0.063	727.813 ± 5.580	740.922 ± 5.563	41.078 ± 6.795
6694.96	MDM	11.472 ± 0.058	740.481 ± 4.658	741.915 ± 4.637	57.954 ± 4.915
6695.56	Asiago	11.336 ± 0.054	745.920 ± 3.667	—	—
6696.90	MDM	11.803 ± 0.060	733.319 ± 4.986	748.523 ± 4.967	90.387 ± 5.660
6698.01	MDM	11.772 ± 0.054	754.050 ± 3.743	759.288 ± 3.718	103.301 ± 2.654
6698.96	MDM	11.905 ± 0.071	773.080 ± 7.113	785.717 ± 7.099	100.651 ± 9.703
6699.04	APO	11.766 ± 0.035	779.014 ± 2.383	—	—
6699.94	MDM	11.992 ± 0.054	771.395 ± 3.829	778.968 ± 3.804	109.650 ± 2.941
6700.95	MDM	11.920 ± 0.054	772.175 ± 3.819	788.781 ± 3.793	116.929 ± 2.924
6701.55	Asiago	11.863 ± 0.055	769.665 ± 3.804	—	—
6701.94	MDM	11.876 ± 0.054	781.178 ± 3.837	785.347 ± 3.812	120.337 ± 3.000
6702.93	MDM	11.948 ± 0.054	776.533 ± 3.849	781.401 ± 3.824	134.364 ± 3.073
6703.92	MDM	12.000 ± 0.055	793.161 ± 3.940	805.131 ± 3.916	132.125 ± 3.342
6703.94	APO	12.227 ± 0.035	793.753 ± 2.409	—	—

Continued on next page

Table B.3 – continued from previous page

HJD−2450000	Telescope	f_{5100}[a]	$f_{\mathrm{H}\beta}$[b]	$f_{\mathrm{H}\beta,\ \mathrm{SD}}$[c]	$f_{\mathrm{He\ II},\ \mathrm{SD}}$[d]
6705.91	MDM	12.196 ± 0.059	784.175 ± 4.810	796.123 ± 4.790	112.452 ± 5.496
6706.62	Asiago	12.107 ± 0.056	811.642 ± 4.018	—	—
6706.94	APO	12.080 ± 0.035	795.650 ± 2.370	—	—
6706.95	MDM	12.160 ± 0.055	800.479 ± 3.919	799.087 ± 3.894	128.266 ± 3.234
6708.00	MDM	12.105 ± 0.055	809.205 ± 4.038	802.359 ± 4.014	130.285 ± 3.572
6709.94	MDM	11.925 ± 0.058	806.710 ± 4.605	812.472 ± 4.584	94.907 ± 4.923
6710.86	MDM	11.630 ± 0.054	791.216 ± 3.715	787.592 ± 3.689	93.851 ± 2.578
6711.51	Asiago	11.491 ± 0.054	799.184 ± 3.698	—	—
6712.54	Asiago	11.285 ± 0.054	786.455 ± 3.671	—	—
6712.86	MDM	11.452 ± 0.058	799.811 ± 4.714	795.030 ± 4.693	78.290 ± 5.063
6713.54	Asiago	11.099 ± 0.054	783.893 ± 3.658	—	—
6713.88	MDM	11.294 ± 0.060	806.890 ± 5.118	800.628 ± 5.100	92.188 ± 5.918
6714.85	MDM	11.294 ± 0.055	791.627 ± 4.038	789.029 ± 4.014	78.074 ± 3.501
6715.90	MDM	11.175 ± 0.054	786.808 ± 3.771	792.054 ± 3.746	68.417 ± 2.726
6716.89	MDM	11.064 ± 0.056	767.574 ± 4.321	767.240 ± 4.298	55.777 ± 4.193
6720.90	MDM	10.530 ± 0.056	742.649 ± 4.273	747.261 ± 4.250	29.992 ± 4.075

Continued on next page

Table B.3 – continued from previous page

HJD−2450000	Telescope	f_{5100}[a]	$f_{\mathrm{H}\beta}$[b]	$f_{\mathrm{H}\beta,\ \mathrm{SD}}$[c]	$f_{\mathrm{He\ II},\ \mathrm{SD}}$[d]
6721.89	MDM	10.490 ± 0.054	726.267 ± 3.871	734.706 ± 3.846	25.566 ± 3.016
6722.60	Asiago	10.248 ± 0.054	724.347 ± 3.660	—	—
6722.95	MDM	10.195 ± 0.056	719.976 ± 4.245	725.579 ± 4.223	33.555 ± 4.029
6723.54	Asiago	10.048 ± 0.054	721.325 ± 3.649	—	—
6723.88	MDM	10.112 ± 0.054	721.234 ± 3.658	729.277 ± 3.631	24.768 ± 2.354
6724.51	Asiago	10.022 ± 0.055	689.675 ± 3.826	—	—
6724.88	MDM	10.080 ± 0.054	712.217 ± 3.784	718.485 ± 3.759	27.609 ± 2.761
6725.52	Asiago	10.079 ± 0.054	699.510 ± 3.741	—	—
6725.93	MDM	10.157 ± 0.054	706.766 ± 3.781	714.794 ± 3.756	27.061 ± 2.755
6726.51	Asiago	10.201 ± 0.054	703.925 ± 3.781	—	—
6726.87	MDM	10.061 ± 0.054	706.917 ± 3.754	710.941 ± 3.728	31.407 ± 2.682
6727.87	MDM	10.296 ± 0.054	704.180 ± 3.806	705.862 ± 3.781	27.759 ± 2.864
6728.53	Asiago	10.668 ± 0.055	705.310 ± 3.865	—	—
6728.92	MDM	10.291 ± 0.054	695.253 ± 3.771	697.471 ± 3.745	24.804 ± 2.745
6729.47	Asiago	10.185 ± 0.054	712.140 ± 3.755	—	—
6729.89	MDM	10.377 ± 0.055	695.342 ± 4.034	707.850 ± 4.010	33.318 ± 3.551

Continued on next page

Table B.3 – continued from previous page

HJD−2450000	Telescope	f_{5100}[a]	$f_{\mathrm{H}\beta}$[b]	$f_{\mathrm{H}\beta,\ \mathrm{SD}}$[c]	$f_{\mathrm{He\ II},\ \mathrm{SD}}$[d]
6730.49	Asiago	10.786 ± 0.056	709.034 ± 4.017	—	—
6730.88	MDM	10.395 ± 0.054	702.628 ± 3.718	705.233 ± 3.692	28.427 ± 2.625
6731.90	MDM	10.483 ± 0.054	693.491 ± 3.810	695.865 ± 3.785	35.587 ± 2.949
6732.91	MDM	10.590 ± 0.055	679.247 ± 3.918	676.466 ± 3.894	24.686 ± 3.325
6733.91	APO	10.387 ± 0.035	662.122 ± 2.364	—	—
6733.93	MDM	10.468 ± 0.054	676.311 ± 3.784	681.671 ± 3.758	26.236 ± 2.885
6734.82	APO	10.377 ± 0.035	707.105 ± 2.467	—	—
6735.82	APO	11.032 ± 0.036	680.069 ± 2.595	—	—
6736.86	WIRO	10.790 ± 0.040	759.805 ± 3.376	—	—
6737.84	WIRO	11.487 ± 0.053	685.009 ± 4.799	—	—
6738.81	APO	11.452 ± 0.038	711.845 ± 2.889	—	—
6738.87	MDM	11.410 ± 0.055	705.373 ± 3.957	705.704 ± 3.933	53.016 ± 3.335
6739.89	MDM	11.800 ± 0.054	713.724 ± 3.820	716.223 ± 3.795	76.636 ± 2.922
6739.90	APO	11.772 ± 0.034	704.311 ± 2.200	—	—
6740.89	MDM	11.899 ± 0.057	733.785 ± 4.558	733.605 ± 4.536	84.629 ± 4.814
6741.88	MDM	11.943 ± 0.054	741.545 ± 3.841	752.540 ± 3.816	106.530 ± 2.969

Continued on next page

Table B.3 – continued from previous page

HJD−2450000	Telescope	f_{5100}[a]	$f_{\mathrm{H}\beta}$[b]	$f_{\mathrm{H}\beta,\ \mathrm{SD}}$[c]	$f_{\mathrm{He\ II},\ \mathrm{SD}}$[d]
6742.84	MDM	12.125 ± 0.054	749.115 ± 3.846	757.241 ± 3.821	104.374 ± 2.986
6744.89	MDM	12.614 ± 0.054	769.203 ± 3.854	765.313 ± 3.829	115.759 ± 3.009
6745.88	MDM	12.763 ± 0.054	764.094 ± 3.888	759.106 ± 3.863	122.396 ± 3.115
6746.89	MDM	12.783 ± 0.056	770.264 ± 4.247	770.126 ± 4.224	132.782 ± 4.062
6747.87	MDM	12.834 ± 0.054	776.773 ± 3.842	786.828 ± 3.817	122.453 ± 2.982
6748.85	MDM	12.773 ± 0.054	788.520 ± 3.846	800.678 ± 3.821	128.790 ± 2.983
6749.84	MDM	13.050 ± 0.055	806.509 ± 3.916	809.576 ± 3.891	128.472 ± 3.185
6751.83	MDM	12.850 ± 0.054	795.829 ± 3.883	803.267 ± 3.858	143.715 ± 3.086
6752.73	MDM	12.773 ± 0.055	809.290 ± 4.087	823.641 ± 4.064	129.457 ± 3.656
6753.82	MDM	12.385 ± 0.054	792.249 ± 3.742	800.863 ± 3.716	91.938 ± 2.653
6754.85	MDM	12.072 ± 0.054	778.395 ± 3.849	784.577 ± 3.824	62.470 ± 2.971
6755.85	MDM	11.969 ± 0.054	772.501 ± 3.865	777.295 ± 3.840	57.796 ± 3.021
6756.86	MDM	12.092 ± 0.054	765.830 ± 3.894	773.199 ± 3.869	61.101 ± 3.117
6757.78	MDM	12.139 ± 0.062	768.639 ± 5.391	766.493 ± 5.373	55.864 ± 6.647
6758.91	MDM	12.246 ± 0.065	761.818 ± 6.027	798.180 ± 6.011	65.653 ± 7.873
6760.84	MDM	11.871 ± 0.055	751.131 ± 4.039	754.031 ± 4.015	41.845 ± 3.577

Continued on next page

Table B.3 – continued from previous page

HJD−2450000	Telescope	f_{5100}[a]	$f_{\mathrm{H}\beta}$[b]	$f_{\mathrm{H}\beta,\ \mathrm{SD}}$[c]	$f_{\mathrm{He\ II},\ \mathrm{SD}}$[d]
6761.80	MDM	11.931 ± 0.056	741.137 ± 4.143	764.827 ± 4.120	64.141 ± 3.900
6762.79	MDM	11.950 ± 0.055	755.846 ± 3.908	752.944 ± 3.884	61.273 ± 3.134
6763.80	MDM	11.926 ± 0.055	755.812 ± 4.045	759.116 ± 4.021	58.975 ± 3.608
6764.84	MDM	11.924 ± 0.055	752.179 ± 4.013	750.934 ± 3.989	57.577 ± 3.506
6767.86	MDM	11.898 ± 0.055	736.131 ± 3.905	756.492 ± 3.881	73.761 ± 3.145
6768.81	WIRO	11.963 ± 0.029	733.332 ± 1.895	—	—
6768.82	MDM	11.952 ± 0.054	731.866 ± 3.879	741.545 ± 3.854	50.283 ± 3.053
6768.83	APO	11.969 ± 0.035	735.215 ± 2.348	—	—
6769.80	WIRO	11.886 ± 0.030	734.662 ± 1.981	—	—
6769.82	APO	12.286 ± 0.035	713.867 ± 2.370	—	—
6770.79	WIRO	11.910 ± 0.030	734.917 ± 1.968	—	—
6770.95	APO	12.422 ± 0.035	734.144 ± 2.445	—	—
6771.74	WIRO	12.509 ± 0.030	749.785 ± 2.010	—	—
6771.83	APO	12.204 ± 0.034	746.026 ± 2.210	—	—
6772.82	APO	12.407 ± 0.034	740.299 ± 2.247	—	—
6772.83	MDM	12.372 ± 0.054	750.419 ± 3.763	767.981 ± 3.738	80.175 ± 2.723

Continued on next page

Table B.3 – continued from previous page

HJD−2450000	Telescope	f_{5100}[a]	$f_{\mathrm{H}\beta}$[b]	$f_{\mathrm{H}\beta,\ \mathrm{SD}}$[c]	$f_{\mathrm{He\ II},\ \mathrm{SD}}$[d]
6773.83	MDM	12.539 ± 0.055	750.703 ± 3.968	749.250 ± 3.943	104.299 ± 3.324
6775.81	MDM	12.527 ± 0.054	768.255 ± 3.801	779.278 ± 3.776	120.947 ± 2.852
6776.81	MDM	12.430 ± 0.054	775.324 ± 3.774	792.014 ± 3.749	117.764 ± 2.759
6777.97	Lick	12.510 ± 0.074	761.144 ± 4.641	—	—
6778.83	Lick	12.299 ± 0.074	748.265 ± 4.652	—	—
6778.83	MDM	12.451 ± 0.054	767.051 ± 3.869	773.067 ± 3.844	84.433 ± 3.043
6779.84	MDM	12.358 ± 0.054	765.802 ± 3.790	768.960 ± 3.764	85.184 ± 2.801
6779.87	Lick	12.240 ± 0.074	757.943 ± 4.613	—	—
6780.82	Lick	12.275 ± 0.074	751.879 ± 4.661	—	—
6780.83	MDM	12.424 ± 0.054	766.223 ± 3.818	774.811 ± 3.793	70.694 ± 2.891
6781.84	MDM	12.270 ± 0.054	756.007 ± 3.794	767.170 ± 3.768	73.555 ± 2.815
6782.84	MDM	12.086 ± 0.054	740.141 ± 3.781	753.636 ± 3.755	51.992 ± 2.798
6783.81	MDM	12.247 ± 0.054	744.277 ± 3.796	762.153 ± 3.770	53.545 ± 2.830
6784.84	MDM	12.418 ± 0.054	753.381 ± 3.844	770.360 ± 3.819	66.976 ± 2.977
6785.83	MDM	12.613 ± 0.054	760.696 ± 3.879	772.371 ± 3.855	78.806 ± 3.088
6786.83	MDM	12.591 ± 0.054	760.489 ± 3.877	770.458 ± 3.852	85.837 ± 3.092

Continued on next page

Table B.3 – continued from previous page

HJD−2450000	Telescope	f_{5100} [a]	$f_{\mathrm{H}\beta}$ [b]	$f_{\mathrm{H}\beta,\ \mathrm{SD}}$ [c]	$f_{\mathrm{He\ II,\ SD}}$ [d]
6787.83	MDM	12.410 ± 0.054	756.461 ± 3.859	769.097 ± 3.834	80.549 ± 3.048
6788.79	MDM	12.694 ± 0.055	762.172 ± 3.990	774.699 ± 3.966	75.114 ± 3.460
6789.83	MDM	12.448 ± 0.055	761.335 ± 4.091	771.047 ± 4.067	74.748 ± 3.773
6790.80	MDM	12.334 ± 0.055	742.957 ± 4.071	761.602 ± 4.048	58.920 ± 3.730
6791.79	MDM	12.590 ± 0.056	739.781 ± 4.170	764.684 ± 4.147	57.566 ± 4.031
6792.80	MDM	12.460 ± 0.055	733.074 ± 4.067	741.020 ± 4.044	64.050 ± 3.741
6793.81	MDM	12.329 ± 0.055	749.035 ± 3.977	758.160 ± 3.952	72.027 ± 3.449
6795.75	MDM	12.206 ± 0.054	741.762 ± 3.884	756.891 ± 3.859	72.068 ± 3.120
6796.76	MDM	12.380 ± 0.069	722.917 ± 6.674	777.866 ± 6.659	81.553 ± 8.955
6797.76	MDM	12.382 ± 0.066	743.191 ± 6.217	744.732 ± 6.202	85.364 ± 8.119
6798.83	MDM	12.319 ± 0.054	745.222 ± 3.838	758.832 ± 3.813	73.077 ± 2.968
6799.81	MDM	12.281 ± 0.054	744.505 ± 3.829	762.856 ± 3.804	66.850 ± 2.938
6800.77	MDM	12.276 ± 0.054	744.329 ± 3.701	763.486 ± 3.675	58.858 ± 2.536
6801.74	MDM	12.295 ± 0.054	753.348 ± 3.845	769.019 ± 3.819	60.320 ± 2.978
6803.79	MDM	12.361 ± 0.055	745.746 ± 3.929	755.765 ± 3.905	55.650 ± 3.216
6804.74	MDM	12.327 ± 0.055	742.180 ± 4.065	757.936 ± 4.041	73.897 ± 3.581

Continued on next page

Table B.3 – continued from previous page

HJD−2450000	Telescope	f_{5100}[a]	$f_{\mathrm{H}\beta}$[b]	$f_{\mathrm{H}\beta,\ \mathrm{SD}}$[c]	$f_{\mathrm{He\ II},\ \mathrm{SD}}$[d]
6805.78	MDM	12.333 ± 0.054	737.276 ± 3.873	758.854 ± 3.848	70.130 ± 3.069
6805.83	Lick	12.579 ± 0.074	730.862 ± 4.627	—	—
6806.74	Lick	12.277 ± 0.074	732.728 ± 4.622	—	—
6807.73	Lick	12.277 ± 0.074	728.933 ± 4.624	—	—
6807.74	MDM	12.293 ± 0.055	738.545 ± 3.992	751.501 ± 3.968	68.361 ± 3.404
6808.76	Lick	12.268 ± 0.074	733.845 ± 4.614	—	—
6808.78	MDM	12.508 ± 0.054	726.772 ± 3.880	735.738 ± 3.856	55.914 ± 3.100
6809.74	MDM	12.397 ± 0.055	745.877 ± 3.994	766.955 ± 3.970	79.829 ± 3.392
6811.70	Lick	12.222 ± 0.074	724.805 ± 4.581	—	—
6811.76	MDM	12.395 ± 0.057	740.199 ± 4.573	748.705 ± 4.552	78.725 ± 4.799
6812.70	Lick	12.320 ± 0.074	728.114 ± 4.586	—	—
6812.76	MDM	12.468 ± 0.056	730.998 ± 4.198	744.933 ± 4.175	77.994 ± 3.940
6813.80	Lick	12.506 ± 0.074	738.549 ± 4.623	—	—
6813.81	MDM	12.598 ± 0.055	737.235 ± 3.950	757.143 ± 3.925	72.978 ± 3.284
6814.74	MDM	12.549 ± 0.054	727.070 ± 3.886	748.483 ± 3.861	72.781 ± 3.131
6814.78	Lick	12.413 ± 0.074	760.329 ± 4.628	—	—

Continued on next page

Table B.3 – continued from previous page

HJD−2450000	Telescope	f_{5100}[a]	$f_{\mathrm{H}\beta}$[b]	$f_{\mathrm{H}\beta,\ \mathrm{SD}}$[c]	$f_{\mathrm{He\ II},\ \mathrm{SD}}$[d]
6815.80	MDM	12.742 ± 0.055	757.778 ± 3.939	774.789 ± 3.915	84.784 ± 3.227
6816.81	MDM	12.862 ± 0.055	754.384 ± 3.982	773.328 ± 3.958	97.686 ± 3.368
6818.80	MDM	13.243 ± 0.055	754.687 ± 4.102	783.493 ± 4.078	125.773 ± 3.743
6819.77	MDM	13.421 ± 0.056	775.633 ± 4.132	792.688 ± 4.109	145.665 ± 3.774
6820.76	MDM	13.384 ± 0.056	784.057 ± 4.160	804.263 ± 4.137	164.325 ± 3.856
6821.74	MDM	13.403 ± 0.055	789.477 ± 3.913	797.224 ± 3.888	162.381 ± 3.212
6823.71	MDM	13.241 ± 0.055	794.300 ± 3.996	809.422 ± 3.972	159.583 ± 3.385
6824.71	MDM	13.395 ± 0.054	813.536 ± 3.740	815.438 ± 3.714	149.172 ± 2.580
6825.69	MDM	13.252 ± 0.055	820.489 ± 4.068	824.884 ± 4.044	150.917 ± 3.470
6826.70	MDM	12.982 ± 0.055	801.258 ± 3.966	812.665 ± 3.942	135.708 ± 3.210
6827.75	MDM	12.552 ± 0.054	800.253 ± 3.858	817.047 ± 3.833	128.621 ± 2.908
6828.73	Lick	12.439 ± 0.074	795.849 ± 4.628	—	—
6828.75	MDM	12.562 ± 0.054	802.470 ± 3.870	826.931 ± 3.845	107.064 ± 2.940
6829.78	MDM	12.766 ± 0.055	781.265 ± 3.931	772.948 ± 3.907	122.800 ± 3.086
6830.73	MDM	12.390 ± 0.054	776.356 ± 3.701	768.063 ± 3.675	119.552 ± 2.411
6831.72	MDM	12.463 ± 0.054	777.707 ± 3.693	768.703 ± 3.667	108.783 ± 2.383

Continued on next page

Table B.3 – continued from previous page

HJD−2450000	Telescope	f_{5100}[a]	$f_{\mathrm{H}\beta}$[b]	$f_{\mathrm{H}\beta,\ \mathrm{SD}}$[c]	$f_{\mathrm{He\ II},\ \mathrm{SD}}$[d]
6831.75	Lick	12.285 ± 0.074	739.703 ± 4.605	—	—
6832.77	MDM	12.611 ± 0.055	779.525 ± 3.860	770.558 ± 3.835	109.982 ± 2.885
6833.77	MDM	12.454 ± 0.054	788.789 ± 3.819	782.802 ± 3.794	118.874 ± 2.786
6834.72	MDM	12.552 ± 0.054	789.407 ± 3.800	782.383 ± 3.775	127.776 ± 2.729
6835.71	Lick	12.636 ± 0.074	755.615 ± 4.619	—	—
6835.72	MDM	12.751 ± 0.055	736.484 ± 3.984	735.419 ± 3.960	76.442 ± 3.248
6836.74	MDM	12.452 ± 0.054	792.942 ± 3.717	772.155 ± 3.691	150.986 ± 2.479
6837.75	MDM	12.652 ± 0.054	791.435 ± 3.650	773.351 ± 3.623	149.791 ± 2.273
6837.77	Lick	12.727 ± 0.074	768.829 ± 4.618	—	—
6838.70	MDM	12.423 ± 0.054	782.698 ± 3.788	773.510 ± 3.762	139.918 ± 2.702
6838.75	Lick	12.614 ± 0.074	765.432 ± 4.611	—	—
6839.70	MDM	12.567 ± 0.054	796.891 ± 3.777	782.786 ± 3.751	146.061 ± 2.669
6843.78	MDM	12.562 ± 0.056	824.406 ± 4.204	808.882 ± 4.181	152.621 ± 3.861
6845.73	MDM	12.338 ± 0.055	795.168 ± 3.989	781.308 ± 3.965	137.881 ± 3.403
6867.70	Lick	12.382 ± 0.074	729.692 ± 4.629	—	—
6868.69	Lick	12.498 ± 0.074	715.600 ± 4.629	—	—

Continued on next page

Table B.3 – continued from previous page

HJD−2450000	Telescope	f_{5100}[a]	$f_{\mathrm{H}\beta}$[b]	$f_{\mathrm{H}\beta,\ \mathrm{SD}}$[c]	$f_{\mathrm{He\ II},\ \mathrm{SD}}$[d]
6869.69	Lick	12.607 ± 0.074	734.319 ± 4.633	—	—
6870.69	Lick	12.937 ± 0.074	732.891 ± 4.638	—	—
6871.68	Lick	12.839 ± 0.074	709.330 ± 4.713	—	—
6874.69	Lick	13.025 ± 0.075	745.080 ± 4.942	—	—

[a] Continuum flux (10^{-15} erg s^{-1} cm^{-2} Å^{-1}) at 5100 Å rest wavelength; includes both AGN and host galaxy contributions.

[b] Hβ flux (10^{-15} erg s^{-1} cm^{-2}) measured after subtracting a straigt-line fit to the continuum.

[c] Flux in 10^{-15} erg s^{-1} cm^{-2} measured from integrating the Hβ residual obtained after subtracting from the data all spectral decomposition (SD) model components except the Hβ components

[d] He II flux (10^{-15} erg s^{-1} cm^{-2}) measured from spectral decomposition models.